MATHEMATICAL MODELING OF CHARGED LIQUID DROPLETS: NUMERICAL SIMULATION AND STABILITY ANALYSIS

Orestis Vantzos

Thesis Prepared for the Degree of

MASTER OF ARTS

UNIVERSITY OF NORTH TEXAS

March 2006

APPROVED:

Santiago Betelu, Major Professor
John Neuberger, Committee Member
John Quintanilla, Committee Member
Neal Brand, Chair of the Department of Mathematics
Sandra L. Terrell, Dean of the Robert B. Toulouse School of Graduate Studies

CONTENTS

ACKNOWLEDGMENTS

- *Dr Nikolaos Alikakos and Dr Santiago Betelu*, for guidance and patience and, moreover, for knowing when to apply what.
- *Vasileios Mpouris, Tasia and Kostas Nasiopoulos, Dia and Dimitris Dimas, and Vasileios Parasxis*, for moral and material support in critical times.

CHAPTER 1

INTRODUCTION

1.1. Motivation

The goal of this thesis is the study of the evolution of three dimensional electrically charged droplets of fluid moving under the influence of surface tension and electrostatic forces. We are particularly interested in the stability of these droplets and the formation of finite time singularities at the free surface. These singularities take the form of conical tips at the surface of the droplet, where the curvature of the surface and the velocity field of the fluid diverge in finite time. The evolution of charged fluid droplets and the formation of the aforementioned singularities are relevant in many different contexts:

- Electrically charged droplets of water are generated in thunderclouds [Duft]. The electric charge affects the way that droplets coalesce and fission, two fundamental phenomena governing the onset of rain.
- In *electrospraying*, an "electrostatic spray gun" is loaded with electrically charged paint, which is in turn attracted by a polarized surface [Bea]. This results in the surface getting coated with a uniform film of paint.
- Stabilization and control of viscous liquid jets by means of electric fields has applications in the production of fibers that are solidified from a liquid phase, as well as in *microencapsulation* [Bar].
- The *Field Emission Electric Propulsion (FEEP) thrusters* [Van], that are used to control satellites, are based on the emission of droplets of liquid propellant off a tungsten needle under the influence of a strong electric field.
- A very promising application of the small scale flow of liquid droplets is the *microfluidic chip* (see [Dvo], [Cho], [For] and [Sto]), where electric fields are used to manipulate small

quantities of chemicals inside an “integrated circuit” of extremely thin channels inside the microfluidic device.

- *Electronic paper* [Hay]. In recent years a number of technologies have been proposed to produce flexible computer displays at industrial scale. One of the technologies, developed by Phillips, consists of electrically charged droplets of ink encapsulated between charged conductors. The transparency of each “pixel” is controlled by the application of an appropriate electric potential that “shapes” the encapsulated ink droplet.

We base our work on a mathematical model where droplets of a conducting viscous fluid are immersed in a dielectric viscous fluid of infinite extent and evolve under the influence of capillarity and electrostatic repulsion. By using the equations of fluid dynamics and electromagnetism and a number of physically realistic assumptions, we reduce the problem to a system of PDEs. The solution of this system of equations is particularly challenging. The difficulties arise from

- the non-linearity of the equations of the model,
- the coupling between the equations of evolution of the free boundary with a system of elliptic PDEs
- the numerically intensive nature of the problem, that precludes the use of simplistic numerical methods.

The problem has a number of mathematically interesting features, including singularity formation in finite time and the potential existence of non spherical equilibria.

1.2. Previous Work

The study of charged liquid droplets dates back to Lord Rayleigh, who in 1882 showed that if the electrical charge Q is larger than a critical value Q_{cr} then spherical drops become unstable [Ray]. The critical charge was found to be $Q_{cr} = \sqrt{64\gamma\pi^2\epsilon_0 R^3}$, where γ is the surface tension, R is the radius of the droplet and ϵ_0 is dielectric constant of the medium in which the droplet is suspended. After the droplet becomes unstable, it undergoes *fission* disintegrating into a number of smaller droplets. Moreover, in recent experiments (see [Duft]) it has been observed that prior to fission, the drop evolves into a prolate spheroid and develops conical tips from which thin jets emerge in finite time. The existence of static solutions on the surface of a conducting fluid, under the influence of an electric field was first studied by Taylor [Tay]. Some solutions have the form of cones, known today as *Taylor cones*, that have a typical half angle of 49.3°. More details can be found in [Yar], in the context of the electrospinning of nanofibers, and in [Sav], who also covers the case of poorly conducting liquids. Both papers include comparisons of the theory with experimental data.

A stability analysis of charged liquid droplets can be found in [Fon], where the existence of static oblate shapes is proven. It should be noted that although their stability is in general unknown, we have found numerical evidence that they are in fact unstable (chapter 5). A number of solutions for the case of a charged droplet lying on a flat dielectric surface are derived in [Bet2], where the rate of the spreading of the droplets is computed.

There are many papers that use numerical methods to study the motion of *axisymmetric* droplets, in which case the dimension of the problem is reduced to 2. The most popular numerical method is the Boundary Elements Method (BEM). The BEM is used in [Bue], [Rez] to study the evolution of a liquid droplet attached to a surface, under the influence of an externally applied electric field. Buehrle *et al* compare the numerical results with an asymptotic analytical model, whereas Reznik *et al* focus on comparison with experimental data.[1] A numerical study of the evolution of a liquid metal surface in the presence of a high electric field can be found in [Suv].[2] The case of a liquid droplet that is electrostatically levitated under the influence of an electric field is studied numerically using BEM in [Feng]. Similarly, [Yang] uses BEM to study numerically the evolution of a liquid droplet under the influence of an electric field, when the droplet is immersed in an external dielectric fluid. Regarding the study of charged liquid droplets, [Bet] combines analytical and numerical results to study the existence and stability of stationary non spherical shapes for charged, isolated droplets. A similar study in [Pel] uses a hybrid FEM[3]/BEM method. In [Bet3], the BEM method is used to study the evolution of charged liquid droplets whose charge

---

[1] [Rez] is also interesting in that it includes photographs of a droplet in various stages of its evolution.

[2] The authors of [Suv] do not use BEM, but a combination of a transformation of the domain with a specialized numerical method.

[3] Finite Elements Method

is equal to Rayleigh's critical charge Q_{cr}. The numerical results indicate that a perturbed sphere with critical charge evolves into a fusiform shape with conical tips, whose semiangle is smaller than that of the Taylor cones.

The literature on the numerical simulation of non axisymmetric liquid droplets is rather limited in comparison. The phenomenon of drop coalescence is studied numerically using BEM in [Baz], [Zin]. Drop coalescence as well as drop breakup are studied in [Cri]. A numerical study of the evolution of multiple drops arranged in a periodic lattice can be found in [Cun]. In all of these papers, the droplets are uncharged and there is no external electric field. The numerical study of the 3D dynamics of electrically charged droplets, which constitutes a large part of this thesis, has apparently not received much attention in the literature.

1.3. Overview

In chapter 2, we introduce an appropriate mathematical model for the problem. Then, in chapter 3, we present the linear stability analysis of a family of solutions that arise from perturbing a sphere of radius R (which is an equilibrium solution). We find explicit expressions for the rate of growth of each solution and for the critical amount of charge that needs to be exceeded for the solution to become unstable.

The *boundary elements method* is introduced in chapter 4. We describe the algorithms necessary to calculate the mean curvature H and surface charge distribution σ on the free boundary, and to integrate the equations of the model numerically. Furthermore, we describe an array of techniques that facilitate our need for an *adaptive* mesh, both in space and time, with which to approximate the evolving free boundary.

In chapter 5 we validate the numerical scheme. We compute the curvature and surface charge density of an ellipsoid and compare with the exact values. We also compute numerically the evolution of the perturbed spheres from chapter 3 and compare with the linearized solutions.

Finally, in chapter 6, we present some numerical results. These are the formation of necks in droplets with supercritical charge, the evolution of a surface with holes, singularity formation on droplets with various symmetries and numerical evidence that oblate spheroids are unstable.

CHAPTER 2

THE MATHEMATICAL MODEL

We consider a droplet D of a fluid A, with viscosity μ_{in}, suspended in an infinite fluid B, with viscosity μ_{out} (see fig. 2.1). Both the interior and exterior fluids evolve according to the Stokes approximation of the Navier-Stokes equations:

$$\mu_{in}\nabla^2\mathbf{u}(\mathbf{x},t) = \nabla p(\mathbf{x},t), \quad \mathbf{x} \in D \tag{2.1a}$$

$$\mu_{out}\nabla^2\mathbf{u}(\mathbf{x},t) = \nabla p(\mathbf{x},t), \quad \mathbf{x} \in \mathbb{R}^3 \setminus D \tag{2.1b}$$

$$\nabla \cdot \mathbf{u}(\mathbf{x},t) = 0, \quad \mathbf{x} \notin \partial D \tag{2.1c}$$

where $\mathbf{u}$ is the *velocity field* and p is the *pressure* in the fluid. From equations (2.1a)-(2.1c) follows immediately that the pressure p is a harmonic function away from the boundary:

$$\nabla^2 p(\mathbf{x},t) = 0, \quad x \notin \partial D \tag{2.2}$$

The dependence on t comes from the motion of the interface, as is explained below. Equations (2.1a)-(2.1c) are a valid approximation, provided the Reynolds number is small:

$$Re = \frac{uR\rho}{\mu} \ll 1 \tag{2.3}$$

where u is the *typical velocity* of the fluid, R is the *characteristic length* of the droplet, ρ is the *density* of the fluid and μ is the *viscosity*. The size of the droplets that we study is of the order of *microns*, and under this condition this hypothesis is usually satisfied.[1] On the other hand, the droplets are large enough to satisfy the *continuum hypothesis*, which dictates that the aggregate of the motion of the molecules of the fluid can be treated as a continuum.[2] It is worth noting

---

[1] For an entertaining discussion on the dynamics of the low Reynolds number regime, see [Pur].

[2] Another limit on the minimum size of the droplets is imposed by the phenomenon of *ion desorption* [Bea], where ions escape from the free boundary directly into the exterior fluid when the electrical field is powerful enough.

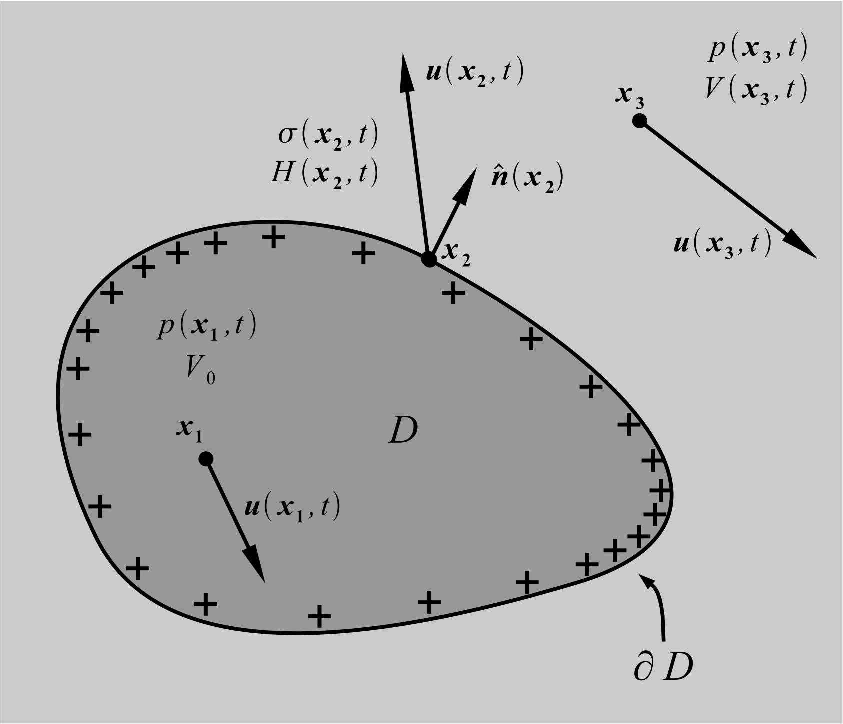

FIGURE 2.1. A charged liquid droplet.

that we also ignore the effects of *evaporation* on the evolution of the droplet. The time scale of the motion of the free boundary is of the order of *milliseconds*, which is clearly insufficient for significant mass loss due to evaporation.

The interior fluid is a perfect electric conductor, whereas the exterior fluid is a perfect electric insulator. Furthermore, the droplet contains an amount of *electric charge* Q. Inside the conducting interior fluid, the charges repel each other and therefore move toward the free boundary. Since they cannot escape into the insulating exterior fluid, they end up distributed along the free boundary ∂D with surface charge density σ and they create an electrical field with *electric potential* V.[3] The potential is constant inside the droplet (see fig. 2.1)

$$V(\mathbf{x},t) = V_0, \quad \text{for } \mathbf{x} \in D \tag{2.4}$$

---

[3] Given that the motion of the charges on the free boundary takes place at a time scale much smaller than the motion of the free boundary itself, it is commonly assumed that at any given moment the charge distribution is in *electrostatic equilibrium*.

and satisfies the Laplace equation outside D

$$\nabla^2 V(\mathbf{x}, t) = 0, \quad \text{for } \mathbf{x} \notin D \tag{2.5}$$

At the free boundary, the potential V is continuous, but the *normal derivative* $\dfrac{\partial V}{\partial n}$ is discontinuous. The jump of the normal derivative and the surface charge density σ on the free boundary are related by

$$\left[\frac{\partial V}{\partial n}\right]_{\partial D} = -\frac{\sigma}{\epsilon_0} \tag{2.6}$$

where $[\cdot]_{\partial D}$ denotes the jump of a quantity across ∂D and ϵ_0 is the *dielectric constant of the surrounding medium*.[4] The surface charge density also satisfies the condition

$$\int_{\partial D} \sigma ds = Q \tag{2.7}$$

By virtue of the *law of charge conservation*, Q is constant in time.

The corresponding boundary condition for the velocity field $\mathbf{u}$ on the free boundary is

$$\begin{aligned} [\mathbb{S}\hat{\mathbf{n}}]_{\partial D} &= \left(2\gamma H - \frac{\epsilon_0}{2}\left(\frac{\partial V}{\partial n}\right)^2\right)\hat{\mathbf{n}} \\ &= \left(2\gamma H - \frac{\sigma^2}{2\epsilon_0}\right)\hat{\mathbf{n}} \end{aligned} \tag{2.8}$$

where γ is the *capillarity constant*, H is the *mean curvature* and $\hat{\mathbf{n}}$ is the (outward pointing) *normal vector* of the free boundary, and $\mathbb{S}$ is the *stress tensor*[5]

$$\mathbb{S}_{ij} = -p\delta_{ij} + \mu\left(\frac{\partial \mathbf{u}_i}{\partial \mathbf{x}_j} + \frac{\partial \mathbf{u}_j}{\partial \mathbf{x}_i}\right), \quad i, j \in \{1, 2, 3\} \tag{2.9}$$

The quantity on the right hand side of (2.8) is called the *traction* ΔT. Note that this boundary condition couples the fluid velocity field with the electrostatic field (via the surface charge density σ).

Finally, the motion of the free boundary itself is governed by the *kinematic condition*

$$\frac{d\mathbf{x}}{dt} = \mathbf{u}(\mathbf{x}, t), \quad \mathbf{x} \in \partial D \tag{2.10}$$

---

[4] This equation can be derived using the first Maxwell equation.

[5] The subscripts in equation (2.9) denote the cartesian coordinates $(\mathbf{x}_1, \mathbf{x}_2, \mathbf{x}_3)$ of a vector $\mathbf{x}$.

The interesting dynamics of the problem stems exactly from the existence of two *opposing forces* acting on the interface between the two fluids, the capillarity (the $2\gamma H$ term in (2.8)) and the electrostatic force (the $\frac{\sigma^2}{2\epsilon_0}$ term in (2.8)). Whereas the capillarity tries to make the droplet as smooth and spherical as possible, the electric forces tend to amplify any "bumps" of the shape of the droplet, as the charges accumulate in parts of the free boundary with high curvature and pull at the surface at these points.

CHAPTER 3

STABILITY ANALYSIS

3.1. Introduction

In this chapter we derive explicit linearized solutions of the mathematical model. Our goal is to understand how the stability of the drop depends on the values of charge, volume, surface tension and viscosity, as well as on the shape of the droplet. We also use the linearized solutions to validate the numerics in chapter 5.

The linearized solutions describe the evolution of a sphere perturbed by a spherical harmonic $\mathcal{Y}_l^m(\theta,\phi)$ with amplitude $\epsilon \ll 1$. For every mode, we calculate a critical value of the charge Q_{cr} that separates stable solutions from unstable ones. If $Q < Q_{cr}$ the solution tends to a sphere, whereas if $Q > Q_{cr}$ the amplitude of the perturbation increases with respect to t. We also calculate the rate of growth of the perturbation. The critical charge Q_{cr} was first computed by Lord Rayleigh [Ray]. A more detailed stability analysis of the problem appears in [Fon]. However, the expression for the growth rate g of the amplitude, that we calculate explicitly in this chapter, has not been published before.

3.2. The Unperturbed Sphere Equilibrium

It is relatively straightforward to verify that a sphere with radius R is an equilibrium solution for the model. Given that we want to study perturbations of a sphere, it is convenient to work in spherical coordinates (r,θ,ϕ), where $r \geq 0$ is the distance of the point from the origin, $\theta \in [0,\pi]$ is the *polar angle* and $\phi \in (0,2\pi]$ is the *azimuthal angle* (see fig. 3.1).

A point $\mathbf{x} \in \mathbb{R}^3$ with spherical coordinates (r,θ,ϕ) has cartesian coordinates

$$\mathbf{x}(r,\theta,\phi) = (r\cos\phi\sin\theta, r\sin\phi\sin\theta, r\cos\theta) \tag{3.1}$$

The base vectors $\hat{\mathbf{e}}_r, \hat{\mathbf{e}}_\theta, \hat{\mathbf{e}}_\phi$ at a point $\mathbf{x}$ form an orthonormal basis and therefore any vector can be expressed uniquely as a linear combination of the base vectors. The base vectors can be

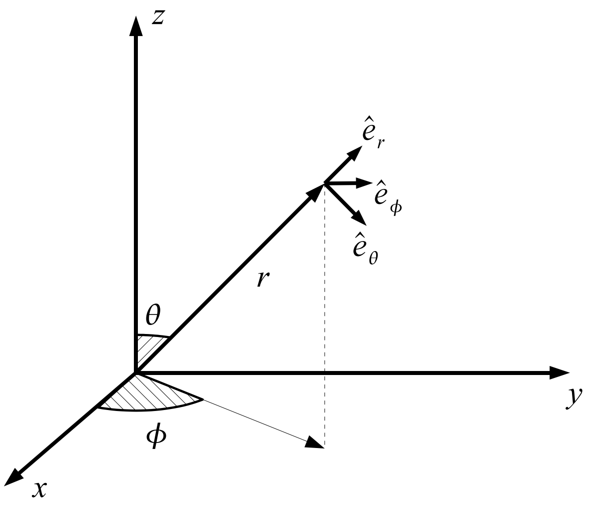

FIGURE 3.1. The Spherical Coordinates (r, θ, ϕ).

expressed in cartesian coordinates as

$$\hat{\mathbf{e}}_r = (\cos\phi\sin\theta, \sin\phi\sin\theta, \cos\theta) \tag{3.2}$$

$$\hat{\mathbf{e}}_\theta = (\cos\theta\cos\phi, \cos\theta\sin\phi, -\sin\theta) \tag{3.3}$$

$$\hat{\mathbf{e}}_\phi = (-\sin\phi, \cos\phi, 0) \tag{3.4}$$

The equation of the sphere takes the following very simple form in spherical coordinates

$$\mathbf{x} \in \partial D \quad \Longleftrightarrow \quad r = R \tag{3.5}$$

For the sphere to be a *static solution*, the velocity must be zero everywhere

$$\mathbf{u}(\mathbf{x}) = 0, \quad \mathbf{x} \in \mathbb{R}^3 \tag{3.6}$$

so that the kinematic condition (2.10) becomes the *equilibrium condition*

$$\frac{d\mathbf{x}}{dt} = 0, \quad \mathbf{x} \in \partial D \tag{3.7}$$

The pressure p is equal to a constant inside the sphere and zero outside

$$p(\mathbf{x}) = \begin{cases} \dfrac{2\gamma}{R} - \dfrac{Q^2}{32\pi^2 R^4 \epsilon_0} & , \mathbf{x} \in D \\ 0 & , \mathbf{x} \notin D \end{cases} \tag{3.8}$$

and hence equations (2.1a)-(2.1c) are trivially satisfied.

The electric potential V is equal to a constant inside and decays like r^{-1} outside of the sphere

$$V(\mathbf{x}) = \begin{cases} \dfrac{Q}{4\pi\epsilon_0 R} & , \mathbf{x} \in D \\ \dfrac{Q}{4\pi\epsilon_0 r} & , \mathbf{x} \notin D \end{cases} \tag{3.9}$$

Clearly, the potential satisfies the Laplace equation (2.5) everywhere, as well as satisfying (2.4) at the surface of the sphere.

The surface charge distribution σ is constant on the sphere

$$\sigma(\mathbf{x}) = \frac{Q}{4\pi R^2}, \quad \mathbf{x} \in \partial D \tag{3.10}$$

and satisfies the equation (2.7):

$$\int_{\partial D} \sigma(\mathbf{x}) ds(\mathbf{x}) = 4\pi R^2 \frac{Q}{4\pi R^2} = Q \tag{3.11}$$

To verify the boundary condition (2.6), note that the normal vector $\hat{\mathbf{n}}$ at any point of the sphere is equal to the base vector $\hat{\mathbf{e}}_r$ and therefore the normal derivative $\dfrac{\partial V(\mathbf{x})}{\partial n}$ of the potential V at a point $\mathbf{x}$ of the sphere is equal to the partial derivative $\dfrac{\partial V(\mathbf{x})}{\partial r}$. Furthermore, since V is constant inside the sphere, the partial derivatives there are zero and hence the jump of the normal derivative is equal to the partial derivative of the "external" branch V_{out} of (3.9) with respect to r:

$$\begin{aligned} \left[\frac{\partial V}{\partial n}\right]_{\partial D} &= \frac{\partial V_{out}}{\partial n} \\ &= \frac{\partial V_{out}}{\partial r} \\ &= \left(\frac{Q}{4\pi\epsilon_0 r}\right)'\bigg|_{r=R} \\ &= -\frac{Q}{4\pi\epsilon_0 R^2} \end{aligned} \tag{3.12}$$

which is equal to $-\dfrac{\sigma}{\epsilon_0}$ in agreement with (2.6).

Finally, the boundary condition (2.8) is also satisfied. Since the velocity $\mathbf{u}$ is zero everywhere, its partial derivatives are also zero and the stress tensor $\mathbb{S}$ reduces to

$$\mathbb{S}_{ij} = -p\delta_{ij}, \quad i, j \in \{1, 2, 3\} \tag{3.13}$$

and thus the jump on the left hand side of (2.8) is equal to

$$[\mathbb{S}\hat{\mathbf{n}}]_{\partial D} = -\,[p]_{\partial D}\,\hat{\mathbf{n}} = -(p_{out} - p_{in})\hat{\mathbf{n}} \overset{(3.8)}{=} \left(\frac{2\gamma}{R} - \frac{Q^2}{32\pi^2 R^4 \epsilon_0}\right)\hat{\mathbf{n}} \tag{3.14}$$

It is a well known fact [DoC] that the mean curvature H of a sphere of radius R is

$$H = \frac{1}{R} \tag{3.15}$$

and hence the right hand side of (2.8) is equal to the left hand side:

$$\begin{aligned} \left(2\gamma H - \frac{\sigma^2}{2\epsilon_0}\right)\hat{\mathbf{n}} &= \left(\frac{2\gamma}{R} - \frac{1}{2\epsilon_0}\left(\frac{Q}{4\pi R^2}\right)^2\right)\hat{\mathbf{n}} \\ &= \left(\frac{2\gamma}{R} - \frac{Q^2}{32\pi^2 R^4 \epsilon_0}\right)\hat{\mathbf{n}} \end{aligned} \tag{3.16}$$

3.3. The Perturbed Sphere: Linearized Solutions

Consider a sphere of radius R perturbed with the real part of the *spherical harmonic*[1] $\mathcal{Y}_l^m(\theta,\phi)$,

$$\begin{aligned} r(\theta,\phi) &= R + \epsilon Re\{\mathcal{Y}_l^m(\theta,\phi)\} \\ &= R + \epsilon \mathcal{P}_l^m(\cos\theta)\cos(m\phi) \end{aligned} \tag{3.17}$$

Here, the *spherical harmonics* $\mathcal{Y}_l^m(\theta,\phi)$ [Abr] are defined (for $l, m \in \mathbb{Z}$, $0 \le |m| \le l$) as

$$\mathcal{Y}_l^m(\theta,\phi) = \sqrt{\frac{2l+1}{4\pi}\frac{(l-m)!}{(l+m)!}}\mathcal{P}_l^m(\cos\theta)e^{im\phi} \tag{3.18}$$

The *associated Legendre polynomials* $\mathcal{P}_l^m(x)$ are defined as [Abr],

$$\mathcal{P}_l^m(x) = \frac{(-1)^m}{2^l l!}(1-x^2)^{m/2}\frac{d^{l+m}}{dx^{l+m}}(x^2-1)^l \tag{3.19}$$

A very useful identity is

$$\mathcal{P}_{l-2}^m(x) = \frac{2l-1}{l+m-1}x\mathcal{P}_{l-1}^m(x) + \frac{m-1}{l+m-1}\mathcal{P}_l^m(x) \tag{3.20}$$

which is essential to most of the following calculations.

The spherical harmonics $\mathcal{Y}_l^m(\theta,\phi)$ can be multiplied with appropriate powers of r to form *solid harmonics* which satisfy the Laplace equation $\nabla^2 f = 0$. There are two cases:

---

[1] We assume that $l \neq 0$, since in that case the only possible mode $\mathcal{Y}_0^0$ has spherical symmetry and therefore the "perturbed" sphere would actually be a perfect sphere itself.

- The solid harmonics of the form

$$f(r,\theta,\phi) = Cr^l \mathcal{Y}_l^m(\theta,\phi), \quad C \neq 0$$

  are defined in all of $\mathbb{R}^3$ and diverge as $r \to \infty$. The constant function $f \equiv 1$ is a special case, for $l = m = 0$.

- The solid harmonics of the form

$$f(r,\theta,\phi) = Cr^{-l-1} \mathcal{Y}_l^m(\theta,\phi), \quad C \neq 0$$

  are not defined for $r = 0$ and are bounded as $r \to \infty$. The function $f(r) = r^{-1}$ is a special case, again for $l = m = 0$.

Moreover, both the real and imaginary part of the solid harmonics, also satisfy the Laplace equation.

In the remainder of this section, we verify the claim that if the free boundary has the shape described by (3.17) at $t = 0$, then at time $t \geq 0$,

$$r(\theta,\phi) = R + \epsilon \mathcal{P}_l^m(\cos\theta)\cos(m\phi)e^{gt} + \mathrm{O}(\epsilon^2) \tag{3.21}$$

where we have used the “big O” notation to indicate higher order terms of the Taylor expansion with respect to ϵ (see fig. 3.2).

Here we show that the parameter g that determines the growth rate of the perturbation, is given by

$$g = \frac{l(l-1)(l+1)(2l+1)(Q^2 - 16(l+2)\pi^2 R^3 \gamma \epsilon_0)(\mu_{in} + \mu_{out})}{16\pi^2 R^4 \epsilon_0((2l^2+4l+3)\mu_{in} + 2l(l+2)\mu_{out})(2(l^2-1)\mu_{in} + (2l^2+1)\mu_{out})} \tag{3.22}$$

The algebraic manipulations that are required for the derivation of (3.22) and the verification of (3.21) are very complicated. As a result, we have made heavy use of the *Mathematica*® computer algebra system[2] [Wol] in the following calculations.

---

[2] *Mathematica* is a registered trademark of Wolfram Research, Inc.

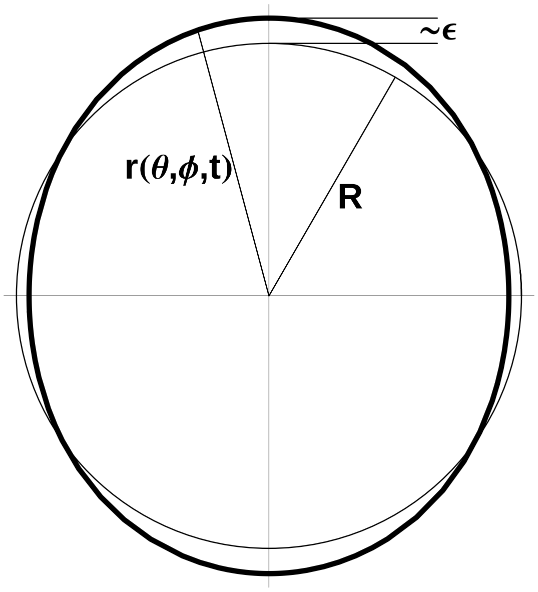

FIGURE 3.2. Sphere perturbed by a harmonic function with amplitude ϵ.

Normal Vector and Mean Curvature

First we derive the normal vector $\hat{\mathbf{n}}$ and mean curvature H at the free boundary at a time $t \geq 0$. We parametrize the surface with respect to the angles (θ, ϕ):

$$\mathbf{r}(\theta,\phi) = r(\theta,\phi)\left(\cos\phi\sin\theta, \sin\phi\sin\theta, \sin\phi\right) = r(\theta,\phi)\hat{\mathbf{e}}_r \tag{3.23}$$

The normal vector $\hat{\mathbf{n}}$ can be calculated by normalizing the cross product of the partial derivatives[3]

$$\begin{aligned}\hat{\mathbf{n}}(\theta,\phi) = \frac{\mathbf{r}_\theta \times \mathbf{r}_\phi}{|\mathbf{r}_\theta \times \mathbf{r}_\phi|} = \hat{\mathbf{e}}_r + \epsilon\frac{(l+m)\mathcal{P}_{l-1}^m(\cos\theta) - l\cos\theta\mathcal{P}_l^m(\cos\theta)}{R\sin\theta}\cos(m\phi)e^{gt}\hat{\mathbf{e}}_\theta + \\ \epsilon\frac{m}{R\sin\theta}\sin(m\phi)\mathcal{P}_l^m(\cos\theta)e^{gt}\hat{\mathbf{e}}_\phi + \mathrm{O}(\epsilon^2)\end{aligned} \tag{3.24}$$

so that

$$|\hat{\mathbf{n}}| = 1 + \mathrm{O}(\epsilon^2) \tag{3.25}$$

The mean curvature H can be found by first calculating the *second fundamental form* of the surface [DoC]. First, we calculate the coefficients $\mathfrak{E}, \mathfrak{F}, \mathfrak{G}$ of the *first fundamental form*, ignoring

---

[3] The use of the parameters θ, ϕ as subscripts denotes differentiation. For instance $\mathbf{r}_\theta = \dfrac{\partial \mathbf{r}}{\partial\theta}$ and $\mathbf{r}_{\theta\phi} = \dfrac{\partial^2\mathbf{r}}{\partial\theta\phi}$.

terms of order ϵ^2:

$$\mathfrak{E} = \mathbf{r}_\theta \cdot \mathbf{r}_\theta \tag{3.26}$$

$$\mathfrak{F} = \mathbf{r}_\phi \cdot \mathbf{r}_\theta \tag{3.27}$$

$$\mathfrak{G} = \mathbf{r}_\phi \cdot \mathbf{r}_\phi \tag{3.28}$$

and we let

$$J = \sqrt{\mathfrak{E}\mathfrak{G} - \mathfrak{F}^2} \tag{3.29}$$

Using that, we calculate the coefficients $\mathfrak{e}, \mathfrak{f}, \mathfrak{g}$ of the second fundamental form

$$\mathfrak{e} = \frac{\det\left(\mathbf{r}_{\theta\theta}\,\mathbf{r}_\phi\,\mathbf{r}_\theta\right)}{J} \tag{3.30}$$

$$\mathfrak{f} = \frac{\det\left(\mathbf{r}_{\phi\theta}\,\mathbf{r}_\phi\,\mathbf{r}_\theta\right)}{J} \tag{3.31}$$

$$\mathfrak{g} = \frac{\det\left(\mathbf{r}_{\phi\phi}\,\mathbf{r}_\phi\,\mathbf{r}_\theta\right)}{J} \tag{3.32}$$

where $\det\left(\mathbf{a}\,\mathbf{b}\,\mathbf{c}\right)$ denotes the determinant of the matrix that has the vectors $\mathbf{a}, \mathbf{b}, \mathbf{c}$ for rows. The mean curvature H is then given by

$$\begin{aligned} H(\theta, \phi) &= \frac{\mathfrak{e}\mathfrak{G} - 2\mathfrak{f}\mathfrak{F} + \mathfrak{g}\mathfrak{E}}{2J^2} \\ &= \frac{1}{R} + \epsilon\frac{l^2 + l - 2}{2R^2}\mathcal{P}_l^m(\cos\theta)\cos(m\phi)e^{gt} + \mathrm{O}(\epsilon^2) \end{aligned} \tag{3.33}$$

Electric Potential and Surface Charge Density

We claim that the electric potential V is given by

$$V(r, \theta, \phi) = \begin{cases} \dfrac{A}{R} & , r \le R \\ \dfrac{A}{r} + \epsilon B r^{-l-1}\cos(m\phi)\mathcal{P}_l^m(\cos\theta)e^{gt} + \mathrm{O}(\epsilon^2) & , r > R \end{cases} \tag{3.34}$$

with

$$A = \frac{Q}{4\pi\epsilon_0} \tag{3.35}$$

$$B = \frac{QR^{l-1}}{4\pi\epsilon_0} \tag{3.36}$$

To begin with, the exterior branch of (3.34) satisfies the Laplace equation (2.5) in the exterior of the surface, since both the zero and first order terms are *solid harmonics*, such that $V \to 0$ as $r \to \infty$. Furthermore, the function V must be continuous at the free boundary and therefore, if we substitute r with $r(\theta, \phi)$ from (3.21) in the exterior branch of (3.34), we should get $\dfrac{A}{R}$ (plus terms of order ϵ^2). After some algebraic manipulations, this condition reduces to

$$AR^l - BR = 0 \quad \Longrightarrow \quad B = AR^{l-1} \tag{3.37}$$

The continuity of V on the boundary also ensures that V is constant on the boundary (eq. (2.4)).

To check condition (2.7), we need to calculate the surface charge density at the surface first. Using (2.6), we find

$$\sigma(\theta, \phi) = \frac{A\epsilon_0}{R^2} + \epsilon\frac{A(l-1)\epsilon_0}{R^3}\cos(m\phi)\mathcal{P}_l^m(\cos\theta)e^{gt} + \mathrm{O}(\epsilon^2) \tag{3.38}$$

Integrating σ over the entire surface, we get

(3.39)

$$\begin{aligned}
\int_{\partial D} \sigma ds &= \int_0^\pi \int_0^{2\pi} \sigma(\theta, \phi) r(\theta, \phi)^2 \sin\theta \, d\phi d\theta \\
&= \int_0^\pi \int_0^{2\pi} \left\{ A\epsilon_0 \sin\theta + \epsilon\frac{A(l+1)\epsilon_0}{R}\sin\theta\cos(m\phi)\mathcal{P}_l^m(\cos\theta)e^{gt} \right\} d\phi d\theta + \mathrm{O}(\epsilon^2) \\
&= 4\pi\epsilon_0 A + \epsilon\frac{A(l+1)\epsilon_0}{R}e^{gt}\int_0^{2\pi}\cos(m\phi)d\phi\int_0^\pi \sin\theta\mathcal{P}_l^m(\cos\theta)d\theta + \mathrm{O}(\epsilon^2)
\end{aligned}$$

We can show that the first order term is zero. There are two cases:

$m \neq 0$: In this case we have

$$\int_0^{2\pi}\cos(m\phi)d\phi = \frac{\sin(2m\pi)}{m} = 0$$

since $m \in \mathbb{Z}$, and therefore the whole term vanishes.

$m = 0$: We perform the change of variables $\sin\theta \to x$ in the second integral:

$$\int_0^\pi \sin\theta\mathcal{P}_l^0(\cos\theta)d\theta = \int_{-1}^1 \mathcal{P}_l^0(x)dx$$

Then, given that $\mathcal{P}_0^0(x) = 1$,

$$\int_{-1}^1 \mathcal{P}_l^0(x)dx = \int_{-1}^1 \mathcal{P}_l^0(x)\mathcal{P}_0^0(x)dx$$

Since $l \neq 0$ by assumption, the two Legendre polynomials have different l but identical $m \equiv 0$. Because of the *orthogonality property* of the Legendre polynomials [Abr], the integral is zero and the whole term vanishes.

Since the first order term of (3.39) is zero, the condition (2.7) becomes

$$Q = 4\pi\epsilon_0 A + \mathrm{O}(\epsilon^2) \tag{3.40}$$

from which (3.35) and (3.36) follow easily.

Interior Velocity and Pressure

Next, we define a pressure p_{in} and a velocity $\mathbf{u}_{in}$ so that the Stokes equations

$$\mu_{in}\nabla^2\mathbf{u}_{in}(\mathbf{x}) = -\nabla p_{in}(\mathbf{x}) \tag{3.41a}$$

$$\nabla \cdot \mathbf{u}_{in}(\mathbf{x}) = 0 \tag{3.41b}$$

are satisfied in the interior of the droplet. We use the explicit solution of the Stokes equations in terms of the spherical harmonics $\mathcal{Y}_l^m(\theta, \phi)$ that can be found at pp. 594-597 of [Lamb].

The pressure p_{in} in the interior of the droplet has the form

$$p_{in}(r, \theta, \phi) = P_0 + \epsilon\gamma_i r^l \mathcal{P}_l^m(\cos\theta)\cos(m\phi)e^{gt} + \mathrm{O}(\epsilon^2) \tag{3.42}$$

where

$$P_0 = \frac{2\gamma}{R} - \frac{Q^2}{32\pi^2 R^4 \epsilon_0} \tag{3.43}$$

is the pressure in the interior of the (unperturbed) sphere, and γ_i is a parameter whose value we need to determine.

To derive the velocity $\mathbf{u}_{in}$, we will define a *special solution* $\mathbf{u}_s$ that satisfies the equations (3.41a)-(3.41b), and add it to the general solution $\mathbf{u}_h$ of the *homogenous problem* (the Stokes equations with $p \equiv 0$).

According to [Lamb], the special solution $\mathbf{u}_s$ has the form

$$\mathbf{u}_s = Ar^2\nabla p_{in} + Br^{2l+3}\nabla\left(\frac{p_{in}}{r^{2l+1}}\right) \tag{3.44}$$

Substituting $\mathbf{u}_s$ and p_{in} in (3.41a) yields

$$2(2l+1)\mu_{in}A - 1 = 0 \quad \Longrightarrow \quad A = \frac{1}{2(2l+1)\mu_{in}} \tag{3.45}$$

whereas substituting into (3.41b) yields

$$(l+1)(2l+3)B - 2lA = 0 \quad \overset{(3.45)}{\Longrightarrow} \quad B = \frac{1}{(l+1)(2l+3)(2l+1)\mu_{in}} \tag{3.46}$$

The general solution of the homogenous system

$$\mu_{in}\nabla^2\mathbf{u}_h(\mathbf{x}) = 0 \tag{3.47a}$$

$$\nabla \cdot \mathbf{u}_h(\mathbf{x}) = 0 \tag{3.47b}$$

is given, again according to [Lamb], by the function $\mathbf{u}_h$ defined by

$$\mathbf{u}_h = \nabla\Phi - \mathbf{x} \times \nabla X \tag{3.48}$$

where the functions Φ, X are solid harmonics of the form

$$\Phi(r,\theta,\phi) = \epsilon\alpha_i r^l \mathcal{P}_l^m(\cos\theta)\cos(m\phi)e^{gt} \tag{3.49}$$

$$X(r,\theta,\phi) = \epsilon\beta_i r^l \mathcal{P}_l^m(\cos\theta)\cos(m\phi)e^{gt} \tag{3.50}$$

The functions $\mathbf{u}_h, \mathbf{u}_s$ can be expressed in spherical coordinates as

$$\begin{aligned}\mathbf{u}_s(r,\theta,\phi) &= \epsilon r^{l+1}\gamma_i \frac{l}{2(2l+3)\mu_{in}}\mathcal{P}_l^m(\cos\theta)\cos(m\phi)e^{gt}\hat{\mathbf{e}}_r \\ &+ \epsilon r^{l+1}\gamma_i \frac{(l+3)\left(l\cos\theta\mathcal{P}_l^m(\cos\theta) - (l+m)\mathcal{P}_{l-1}^m(\cos\theta)\right)}{2(l+1)(2l+3)\mu_{in}\sin\theta}\cos(m\phi)e^{gt}\hat{\mathbf{e}}_\theta \\ &- \epsilon r^{l+1}\gamma_i \frac{(l+3)m}{2(l+1)(2l+3)\mu_{in}\sin\theta}\mathcal{P}_l^m(\cos\theta)\sin(m\phi)e^{gt}\hat{\mathbf{e}}_\phi + \mathrm{O}(\epsilon^2)\end{aligned} \tag{3.51}$$

and

$$\begin{aligned}\mathbf{u}_h(r,\theta,\phi) &= \epsilon r^{l-1}\alpha_i l\mathcal{P}_l^m(\cos\theta)\cos(m\phi)e^{gt}\hat{\mathbf{e}}_r \\ &- \epsilon r^{l-1}\frac{\alpha_i(l+m)\cos(m\phi)\mathcal{P}_{l-1}^m(\cos\theta) + \left(\beta_i rm\sin(m\phi) - \alpha_i l\cos\theta\cos(m\phi)\right)\mathcal{P}_l^m(\cos\theta)}{\sin\theta}e^{gt}\hat{\mathbf{e}}_\theta \\ &+ \epsilon r^{l-1}\frac{\beta_i r(l+m)\cos(m\phi)\mathcal{P}_{l-1}^m(\cos\theta) - \left(\alpha_i m\sin(m\phi) + \beta_i rl\cos\theta\cos(m\phi)\right)\mathcal{P}_l^m(\cos\theta)}{\sin\theta}e^{gt}\hat{\mathbf{e}}_\phi\end{aligned} \tag{3.52}$$

$$+ \mathrm{O}(\epsilon^2)$$

The velocity of the fluid in the interior of the droplet is the sum of the two velocities

(3.53) $$\mathbf{u}_{in} = \mathbf{u}_s + \mathbf{u}_h$$

for values of the parameters α_i, β_i and γ_i which remain to be determined by the boundary conditions.

Exterior Velocity and Pressure

In the exterior of the droplet, the velocity $\mathbf{u}_{out}$ and the pressure p_{out} satisfy the Stokes equations

(3.54a) $$\mu_{out}\nabla^2\mathbf{u}_{out}(\mathbf{x}) = -\nabla p_{out}(\mathbf{x})$$

(3.54b) $$\nabla \cdot \mathbf{u}_{out}(\mathbf{x}) = 0$$

Furthermore, we require that both the velocity and pressure vanish as $r \to \infty$, and therefore the pressure p_{out} has the form

(3.55) $$p_{out}(r,\theta,\phi) = \epsilon\gamma_o r^{-l-1}\mathcal{P}_l^m(\cos\theta)\cos(m\phi)e^{gt} + \mathrm{O}(\epsilon^2)$$

where γ_o is a parameter that we need to determine. This is analogous to the definition of the pressure in the interior, except for the fact that we used the appropriate solid harmonic for the (infinite) exterior domain and we omitted the constant term P_0, in agreement with the requirement that $P \to 0$ as $r \to \infty$.

Exactly as in the case of the interior domain, we define a special solution $\mathbf{u}_s$ and the general solution $\mathbf{u}_h$ of the homogenous problem and add them to arrive at the velocity $\mathbf{u}_{out}$. For the special solution $\mathbf{u}_s$, we use the definition (3.44) again:

(3.56) $$\mathbf{u}_s = Ar^2\nabla p_{out} + Br^{2l+3}\nabla\left(\frac{p_{out}}{r^{2l+1}}\right)$$

but with (potentially) different A and B. Indeed, substituting $\mathbf{u}_s$ and p_{out} into (3.54a), it reduces to

(3.57) $$2(2l+1)(A+2B)\mu_{out} + 1 = 0$$

whereas substituting into (3.54b) yields

$$2(l+1)A - (2l^2 - 5l - 4)B = 0 \tag{3.58}$$

Solving the system (3.57)-(3.58), we get

$$A = \frac{2l^2 - 5l + 4}{2l(1-2l)(2l+1)\mu_{out}} \tag{3.59}$$

$$B = \frac{l+1}{l(1-2l)(2l+1)\mu_{out}} \tag{3.60}$$

The general solution of the homogenous system

$$\mu_{out}\nabla^2 \mathbf{u}_h(\mathbf{x}) = 0 \tag{3.61a}$$

$$\nabla \cdot \mathbf{u}_h(\mathbf{x}) = 0 \tag{3.61b}$$

is given, exactly like in the interior domain and according to [Lamb], by the function $\mathbf{u}_h$ defined by

$$\mathbf{u}_h = \nabla\Phi - \mathbf{x} \times \nabla X \tag{3.62}$$

where the functions Φ, X are solid harmonics of the form

$$\Phi(r,\theta,\phi) = \epsilon\alpha_o r^{-l-1}\mathcal{P}_l^m(\cos\theta)\cos(m\phi)e^{gt} \tag{3.63}$$

$$X(r,\theta,\phi) = \epsilon\beta_o r^{-l-1}\mathcal{P}_l^m(\cos\theta)\cos(m\phi)e^{gt} \tag{3.64}$$

Expressed in spherical coordinates,

$$\begin{aligned}\mathbf{u}_s(r,\theta,\phi) = {} & \epsilon r^{-l}\gamma_o \frac{l+1}{2(2l-1)\mu_{out}}\mathcal{P}_l^m(\cos\theta)\cos(m\phi)e^{gt}\hat{\mathbf{e}}_r \\ & + \epsilon r^{-l}\gamma_o \frac{(l-2)\left((l+m)\mathcal{P}_{l-1}^m(\cos\theta) - l\cos\theta\mathcal{P}_l^m(\cos\theta)\right)}{2l(2l-1)\mu_{out}\sin\theta}\cos(m\phi)e^{gt}\hat{\mathbf{e}}_\theta \\ & + \epsilon r^{-l}\gamma_o \frac{(l-2)m}{2l(2l-1)\mu_{out}\sin\theta}\mathcal{P}_l^m(\cos\theta)\sin(m\phi)e^{gt}\hat{\mathbf{e}}_\phi + \mathrm{O}(\epsilon^2)\end{aligned} \tag{3.65}$$

and

$$\mathbf{u}_h(r,\theta,\phi) = -\epsilon r^{-l-2}\alpha_o(l+1)\mathcal{P}_l^m(\cos\theta)\cos(m\phi)e^{gt}\hat{\mathbf{e}}_r \tag{3.66}$$

$$
\begin{aligned}
&- \epsilon r^{-l-2}\frac{\alpha_o(l+m)\cos(m\phi)\mathcal{P}_{l-1}^m(\cos\theta)+\left(\beta_o rm\sin(m\phi)-\alpha_o l\cos\theta\cos(m\phi)\right)\mathcal{P}_l^m(\cos\theta)}{\sin\theta}e^{gt}\hat{\mathbf{e}}_\theta \\
&+ \epsilon r^{-l-2}\frac{\beta_o r(l+m)\cos(m\phi)\mathcal{P}_{l-1}^m(\cos\theta)-\left(\alpha_o m\sin(m\phi)+\beta_o rl\cos\theta\cos(m\phi)\right)\mathcal{P}_l^m(\cos\theta)}{\sin\theta}e^{gt}\hat{\mathbf{e}}_\phi \\
&\qquad + \mathrm{O}(\epsilon^2)
\end{aligned}
$$

The velocity of the fluid in the exterior of the droplet is the sum of the two velocities

$$\mathbf{u}_{out} = \mathbf{u}_s + \mathbf{u}_h \tag{3.67}$$

for values of the parameters α_o, β_o and γ_o which remain to be determined by the boundary conditions.

Boundary Conditions

The values of the parameters $(\alpha_i, \beta_i, \gamma_i, \alpha_o, \beta_o, \gamma_o)$ can be determined with the help of the boundary conditions of the mathematical model.

The velocity field must be *continuous* at the free boundary, hence

$$\mathbf{u}_{in}(r(\theta,\phi),\theta,\phi) = \mathbf{u}_{out}(r(\theta,\phi),\theta,\phi), \quad \theta \in [0,\pi], \phi \in (0,2\pi] \tag{3.68}$$

where $r(\theta,\phi)$ is given by (3.21) and $\mathbf{u}_{in}, \mathbf{u}_{out}$ by (3.53) and (3.67) respectively.

Furthermore, the velocity field must satisfy the *traction boundary condition*

$$\left(\mathbb{S}_{out} - \mathbb{S}_{in}\right)\hat{\mathbf{n}} = \left(2\gamma H - \frac{\sigma^2}{2\epsilon_0}\right)\hat{\mathbf{n}} \tag{3.69}$$

where

$$(\mathbb{S}_{out})_{ij} = -p_{out}\delta_{ij} + \mu_{out}\left(\frac{\partial(\mathbf{u}_{out})_i}{\partial \mathbf{x}_j} + \frac{\partial(\mathbf{u}_{out})_j}{\partial \mathbf{x}_i}\right) \tag{3.70}$$

$$(\mathbb{S}_{in})_{ij} = -p_{in}\delta_{ij} + \mu_{in}\left(\frac{\partial(\mathbf{u}_{in})_i}{\partial \mathbf{x}_j} + \frac{\partial(\mathbf{u}_{in})_j}{\partial \mathbf{x}_i}\right) \tag{3.71}$$

and the quantities[4] $\hat{\mathbf{n}}, H, \sigma, p_{in}, p_{out}$ and the partial derivatives of $\mathbf{u}_{in}, \mathbf{u}_{out}$ are evaluated at the spherical coordinates $(r(\theta,\phi),\theta,\phi)$.

---

[4] Defined in (3.24),(3.33),(3.38),(3.42) and (3.55) respectively

The boundary conditions (3.68) and (3.69) yield a total of six algebraic equations with the parameters $(\alpha_i, \beta_i, \gamma_i, \alpha_o, \beta_o, \gamma_o)$ as unknowns. Their solution is

$$\alpha_i = \frac{(l-1)(l+1)R^{-l-3}\left(Q^2 - 16(l+2)\pi^2 R^3 \gamma \epsilon_0\right)\left((2l^2+4l+3)\mu_{out} + 2l(l+2)\mu_{in}\right)}{32\pi^2\epsilon_0\left((2l^2+4l+3)\mu_{in} + 2l(l+2)\mu_{out}\right)\left((2l^2+1)\mu_{out} + 2(l^2-1)\mu_{in}\right)} \tag{3.72}$$

$$\beta_i = 0 \tag{3.73}$$

$$\gamma_i = -\frac{(l-1)(l+1)(2l+3)R^{-l-5}\left(Q^2 - 16(l+2)\pi^2 R^3 \gamma \epsilon_0\right)\mu_{in}}{16\pi^2\epsilon_0\left((2l^2+4l+3)\mu_{in} + 2l(l+2)\mu_{out}\right)} \tag{3.74}$$

and

$$\alpha_o = \frac{(l-1)lR^{l-2}\left(Q^2 - 16(l+2)\pi^2 R^3 \gamma \epsilon_0\right)\left((2l^2+1)\mu_{in} + 2(l^2-1)\mu_{out}\right)}{32\pi^2\epsilon_0\left((2l^2+4l+3)\mu_{in} + 2l(l+2)\mu_{out}\right)\left((2l^2+1)\mu_{out} + 2(l^2-1)\mu_{in}\right)} \tag{3.75}$$

$$\beta_o = 0 \tag{3.76}$$

$$\gamma_o = \frac{(l-1)l(2l-1)R^{l-4}\left(Q^2 - 16(l+2)\pi^2 R^3 \gamma \epsilon_0\right)\mu_{out}}{16\pi^2\epsilon_0\left((2l^2+1)\mu_{out} + 2(l^2-1)\mu_{in}\right)} \tag{3.77}$$

Finally, from the *kinematic condition*

$$\frac{d\mathbf{r}}{dt} = \mathbf{u}(\mathbf{r}, t) \tag{3.78}$$

where $\mathbf{r}$ is given by (3.21) and $\mathbf{u}$ is either[5] $\mathbf{u}_{in}$ or $\mathbf{u}_{out}$ evaluated at $(r(\theta,\phi),\theta,\phi)$, we can derive the explicit expression (3.22) for the parameter g.

3.4. Stability Analysis of the Linearized Solutions

In the previous section, we established that the linearized solution that corresponds to the mode $\mathcal{Y}_l^m$ has the form

$$r(\theta,\phi) = R + \epsilon \mathcal{P}_l^m(\cos\theta)\cos(m\phi)e^{gt} + \mathrm{O}(\epsilon^2)$$

with

$$g = \frac{l(l-1)(l+1)(2l+1)(Q^2 - 16(l+2)\pi^2 R^3 \gamma \epsilon_0)(\mu_{in} + \mu_{out})}{16\pi^2 R^4 \epsilon_0((2l^2+4l+3)\mu_{in} + 2l(l+2)\mu_{out})(2(l^2-1)\mu_{in} + (2l^2+1)\mu_{out})}$$

For any given mode, there are three possibilities:

---

[5] Because of (3.68), $\mathbf{u}_{in}$ and $\mathbf{u}_{out}$ are equal on the free boundary.

- If $g < 0$, then the perturbation vanishes as t goes to infinity and the free boundary will tend to relax into a sphere with radius R. This is an indication that the solution of the nonlinear problem is *stable*.
- If $g > 0$, then the perturbation tends to grow exponentially with time. This is an indication that the solution of the nonlinear problem is *unstable*.
- If $g = 0$, then the analysis is inconclusive.[6]

To study the dependency of the stability on l and m, as well as on the various physical parameters of the model, it is convenient to assume that the two viscosities are equal. Assuming that $\mu_{out} = \mu_{in} \equiv \mu$, the equation for g becomes

$$g = \frac{(l-1)l(l+1)(Q^2 - 16(l+2)\pi^2 R^3 \gamma \epsilon_0)}{8(2l-1)(2l+1)(2l+3)\pi^2 R^4 \mu \epsilon_0} \tag{3.79}$$

For $l = 0$ or $l = 1$, $g \equiv 0$ regardless of the values of the remaining parameters. This is expected, since perturbing a sphere with the modes $\mathcal{Y}_0^0$, $\mathcal{Y}_1^0$ or $\mathcal{Y}_1^{\pm 1}$ results in a translated sphere and we have already proven that a sphere of any radius is an equilibrium.

For $l \geq 2$, all the factors except for $Q^2 - 16(l+2)\pi^2 R^3 \gamma \epsilon_0$ are strictly positive, and therefore g has the same sign as that factor. More specifically, if we define the *critical charge* Q_{cr} as

$$Q_{cr} = 4\pi\sqrt{(l+2)R^3\gamma\epsilon_0} \tag{3.80}$$

then

$$Q < Q_{cr} \iff g < 0 \qquad \textit{Stable} \tag{3.81}$$

$$Q = Q_{cr} \iff g = 0 \qquad \textit{Inconclusive} \tag{3.82}$$

$$Q > Q_{cr} \iff g > 0 \qquad \textit{Unstable} \tag{3.83}$$

In general, a surface of the form $r \equiv r(\theta, \phi)$ is a superposition of various modes. Hence, it is interesting to compare the value of g for various values of l, when the other parameters are

---

[6] The solution could be a (quadratically unstable) equilibrium, but in this case our stability analysis is not useful.

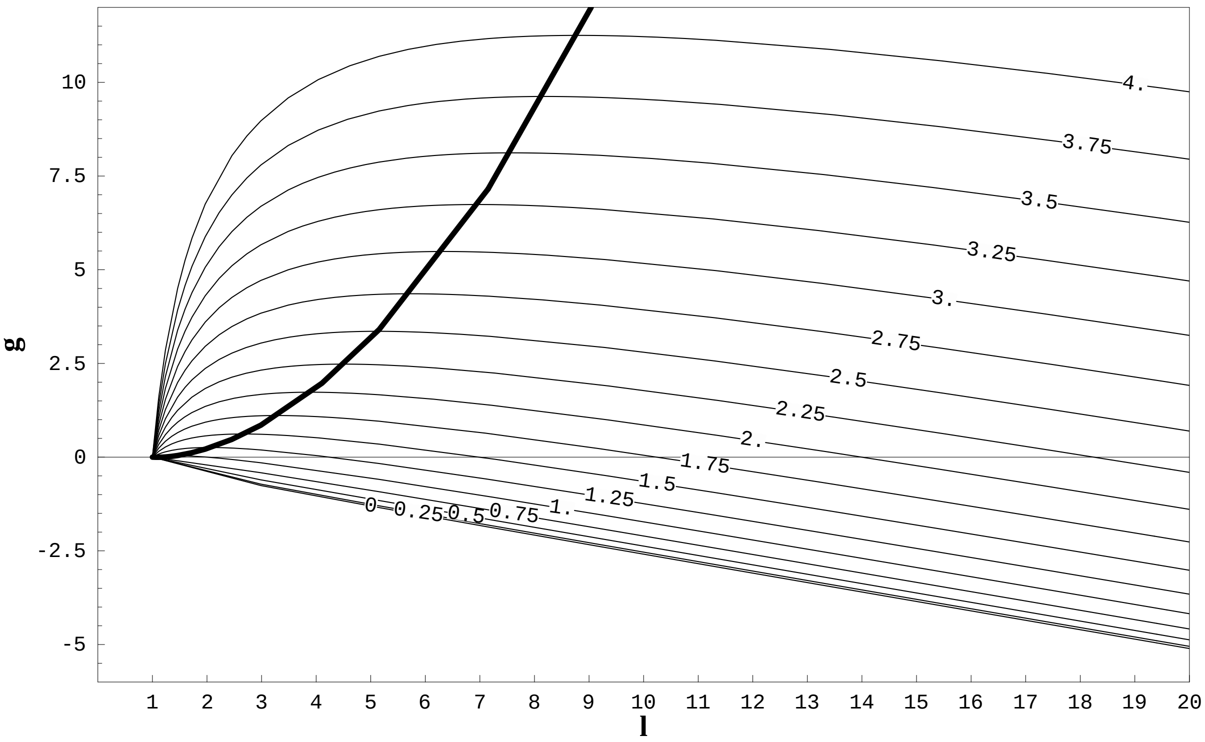

FIGURE 3.3. Plot of g as a function of l for various values of q. The heavy line on the left part of the graph is the locus of the maxima of g (as we vary q).

fixed. It is convenient to introduce a *dimensionless charge* q defined as

$$q = \frac{Q}{Q_2} \tag{3.84}$$

where $Q_2 = 8\pi\sqrt{R^3\gamma\epsilon_0}$ is the critical charge Q_{cr} for the $\mathcal{Y}_2^0$ mode. We also introduce a *characteristic time* τ defined as

$$\tau = \frac{R\mu}{\gamma} \tag{3.85}$$

Using these definitions, g simplifies to

$$g = \frac{2(l-1)l(l+1)(4q^2-l-2)}{(2l-1)(2l+1)(2l+3)}\,\tau^{-1} \tag{3.86}$$

The behavior of g as a function of l and q is presented in figure 3.3. We distinguish three cases:

For $q < 1$, g is negative and strictly decreasing for all $l \geq 2$. It follows that all the modes vanish as $t \to \infty$ and the free boundary tends to a sphere of radius R.

For $q = 1$, g is zero for $l = 2$ and negative for all the other modes.

For $q > 1$, g is positive and increasing up to $l = l_{max}$, where it has a maximum, and then it decreases monotonically, changing sign at $l = l_0$. From (3.87) we have

(3.87) $$l_0 = 4q^2 - 2$$

and[7]

(3.88) $$l_{max} \approx q\sqrt{6} - 1$$

By solving (3.88) for q, we conclude that a mode $\mathcal{Y}_l^m$ is *dominant*, in the sense that it will outgrow modes with different l as $t \to \infty$, for values of q close to

(3.89) $$q_{max} = \frac{l+1}{\sqrt{6}}$$

When the two viscosities μ_{in}, μ_{out} are different, one can show that the evolution of the free boundary is approximately the same with the case where both viscosities are identical and equal to the *arithmetic mean* $\dfrac{\mu_{in} + \mu_{out}}{2}$.

3.5. Visualization of the Linearized Solutions

In the figures of this section, we plot various quantities of interest for the following modes:

- The mode $\mathcal{Y}_2^0$ which has *cylindrical symmetry around the z axis*.
- The mode $\mathcal{Y}_3^2$ which has *tetrahedral symmetry*.
- The superposition $\lambda\mathcal{Y}_4^0 + \mathcal{Y}_4^3$ with $\lambda = \sqrt{\frac{7}{40}}$ of the modes $\mathcal{Y}_4^0$ and $\mathcal{Y}_4^3$, which has *cubical symmetry*.

All the graphs correspond to *subcritical* ($Q < Q_{cr}$) values of Q.

---

[7] The approximation becomes better as $l \to \infty$, but even for small l it is accurate to at least 3 significant digits.

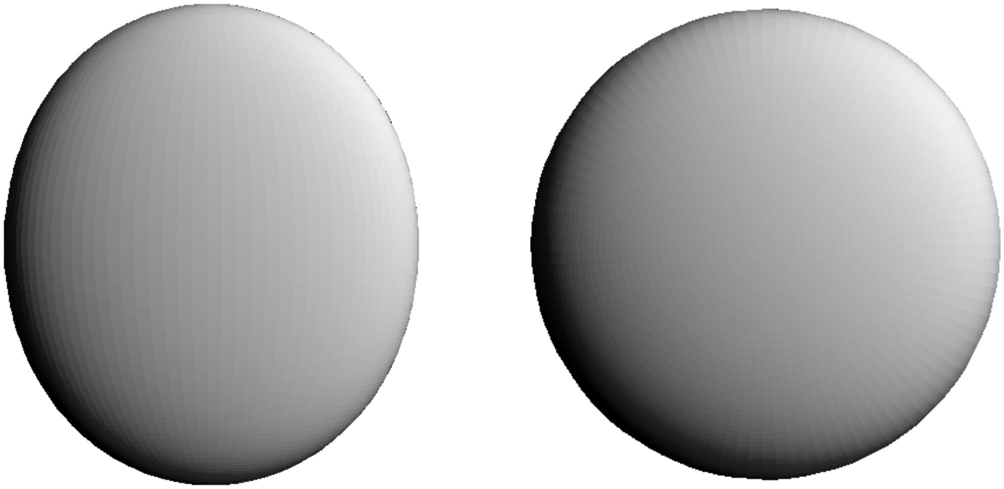

FIGURE 3.4. Sphere perturbed with $\mathcal{Y}_2^0$: The free surface viewed from the y and z directions. The surface has cylindrical symmetry around the z axis.

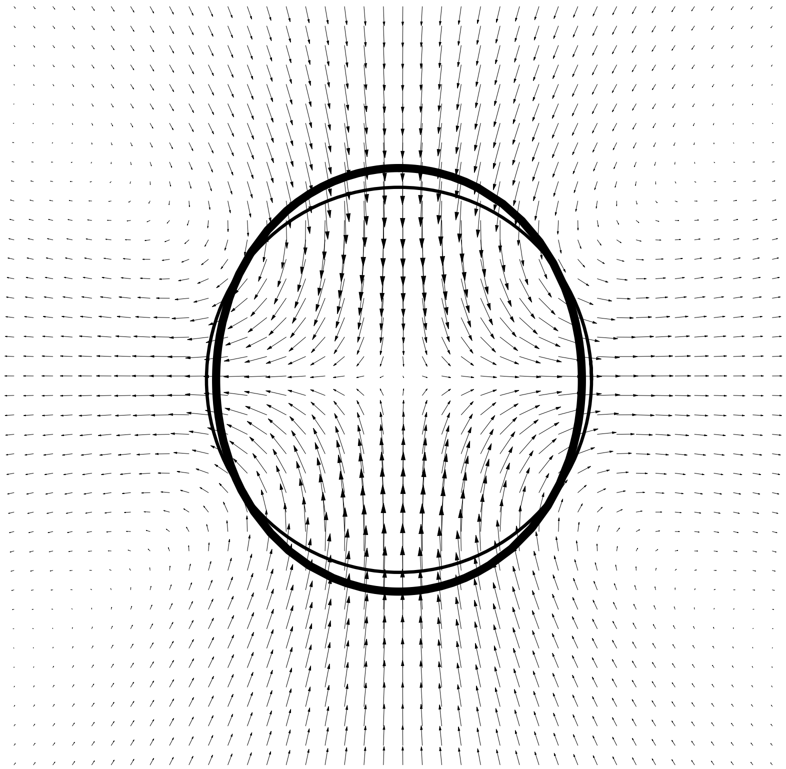

FIGURE 3.5. Sphere perturbed with $\mathcal{Y}_2^0$: The velocity field on the xz plane. The intersection of the free surface and the unperturbed sphere with the xz plane is also visible.

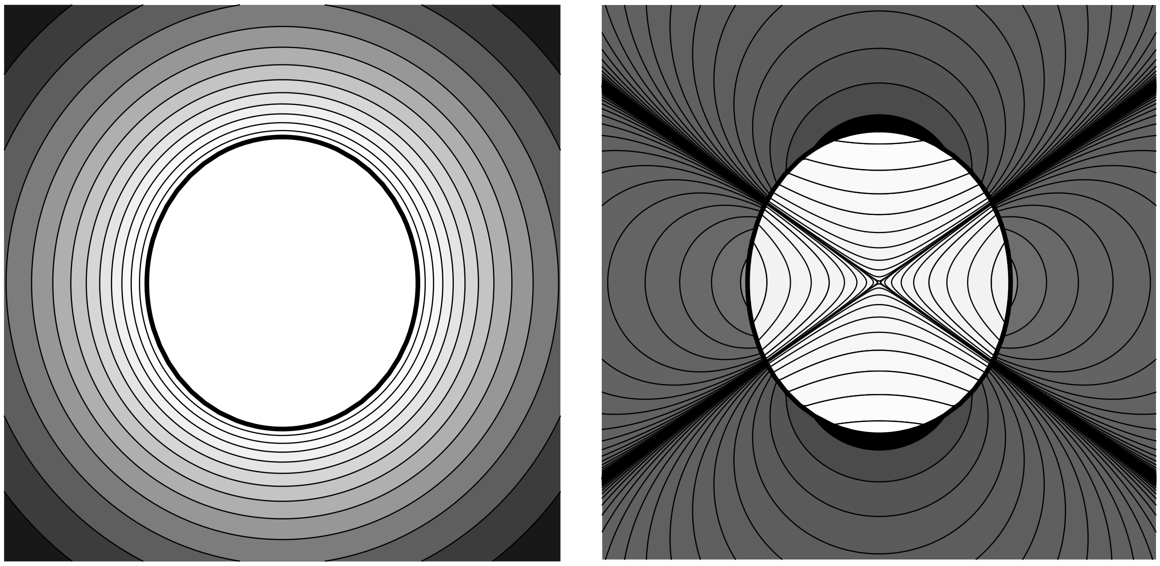

FIGURE 3.6. Sphere perturbed with $\mathcal{Y}_2^0$ mode: Contours of the potential V and the pressure of the fluid p (xz plane). Brighter areas correspond to higher values.

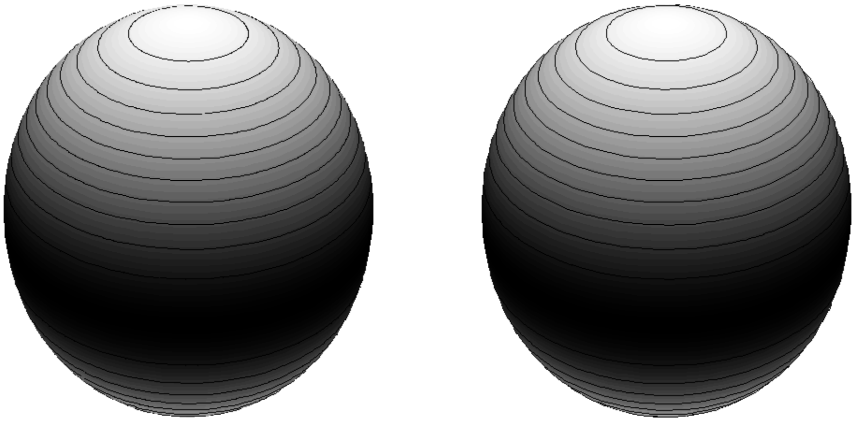

FIGURE 3.7. Sphere perturbed with $\mathcal{Y}_2^0$: The mean curvature H and the surface charge density σ on the free surface. Brighter areas of the surface correspond to higher values. H and σ are constant along the contour lines. The two graphs are identical, since H and σ vary in the same manner along the surface.

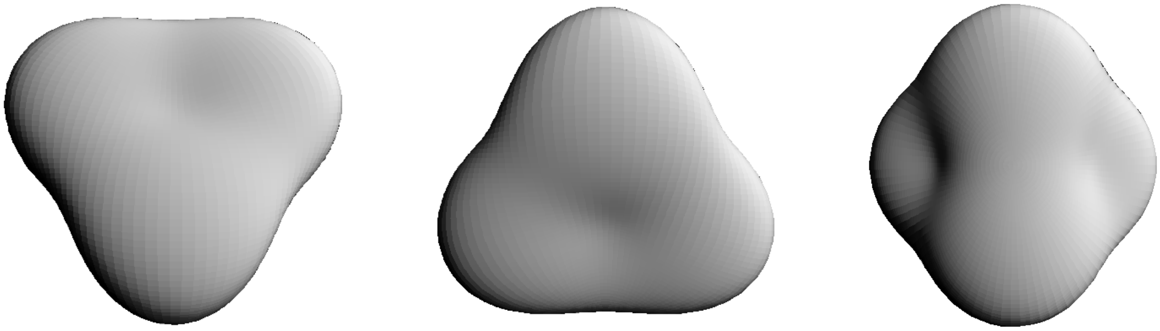

FIGURE 3.8. Sphere perturbed with $\mathcal{Y}_3^2$: The free surface viewed from the x, y and z directions. The surface has tetrahedral symmetry.

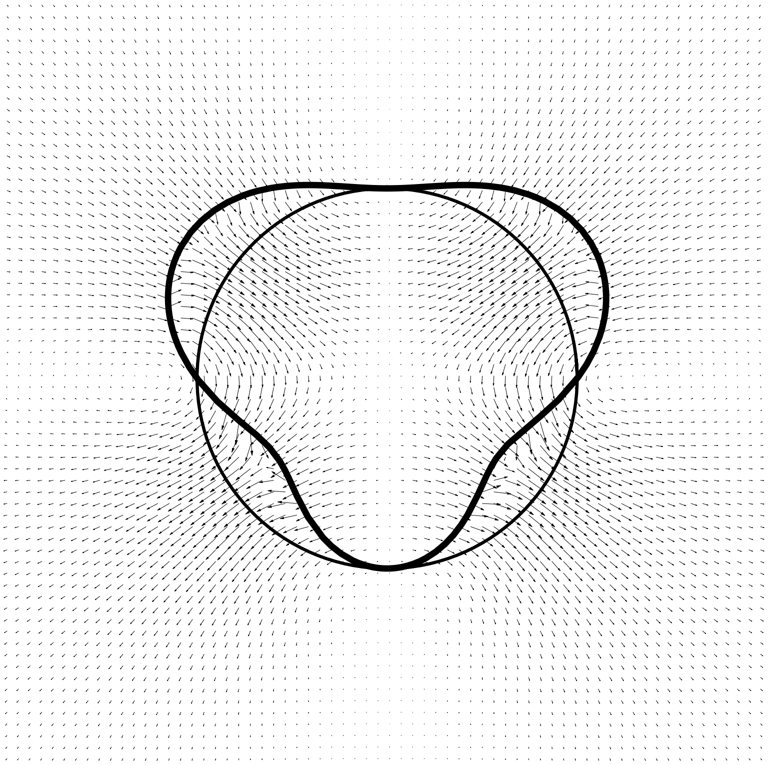

FIGURE 3.9. Sphere perturbed with $\mathcal{Y}_3^2$ mode: The velocity field on the xz plane. The intersection of the free surface and the unperturbed sphere with the xz plane is also visible.

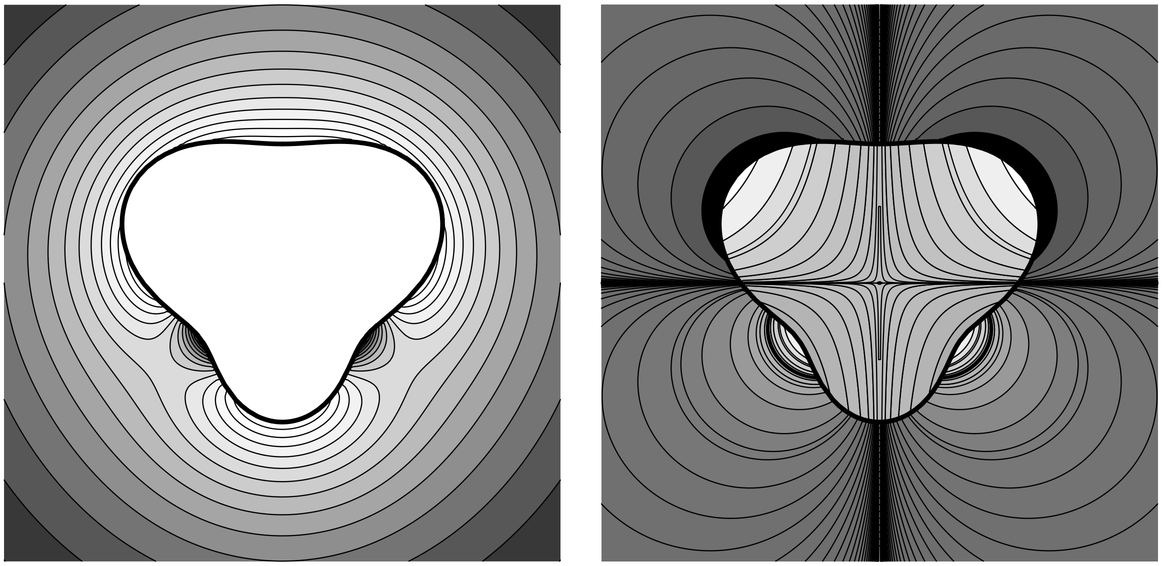

FIGURE 3.10. Sphere perturbed with $\mathcal{Y}_3^2$: Contours of the potential V and the pressure of the fluid p (xz plane). Brighter areas correspond to higher values.

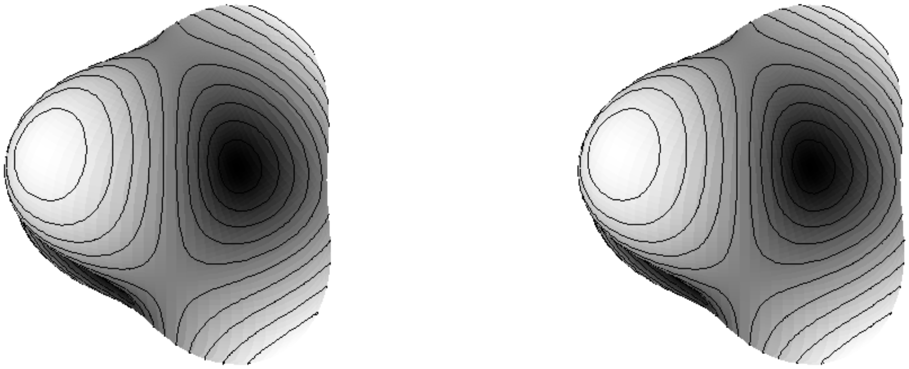

FIGURE 3.11. Sphere perturbed with $\mathcal{Y}_3^2$: The mean curvature H and the surface charge density σ on the free surface. Brighter areas of the surface correspond to higher values. H and σ are constant along the contour lines. The two graphs are identical, since H and σ vary in the same manner along the surface.

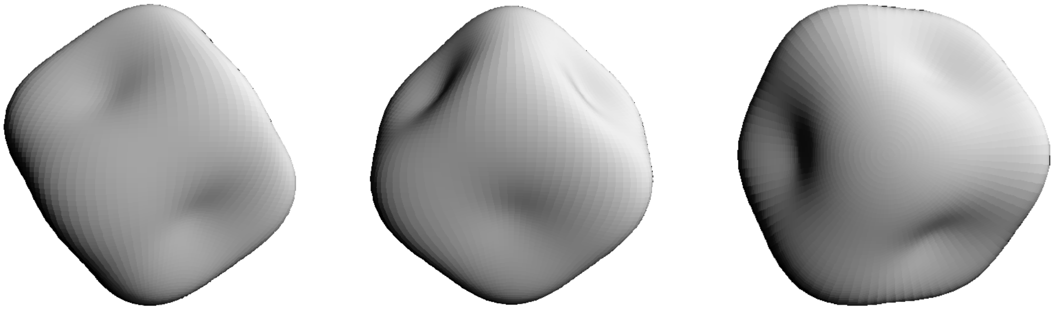

FIGURE 3.12. Sphere perturbed with $\lambda\mathcal{Y}_4^0 + \mathcal{Y}_4^3$: The free surface viewed from the x, y and z directions. The surface has cubical symmetry.

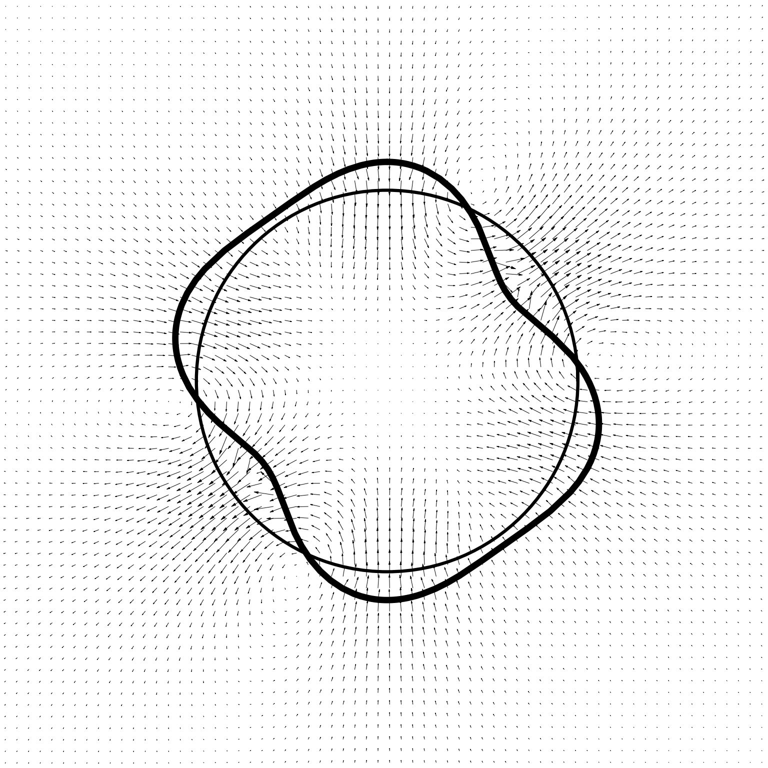

FIGURE 3.13. Sphere perturbed with $\lambda\mathcal{Y}_4^0 + \mathcal{Y}_4^3$: The velocity field on the xz plane. The intersection of the free surface and the unperturbed sphere with the xz plane is also visible.

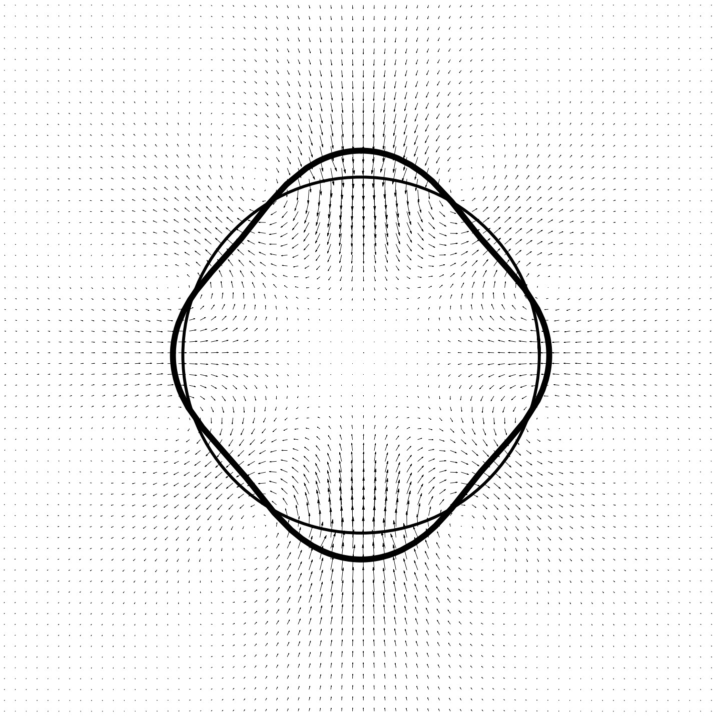

FIGURE 3.14. Sphere perturbed with $\lambda\mathcal{Y}_4^0 + \mathcal{Y}_4^3$: The velocity field on the yz plane. The intersection of the free surface and the unperturbed sphere with the yz plane is also visible.

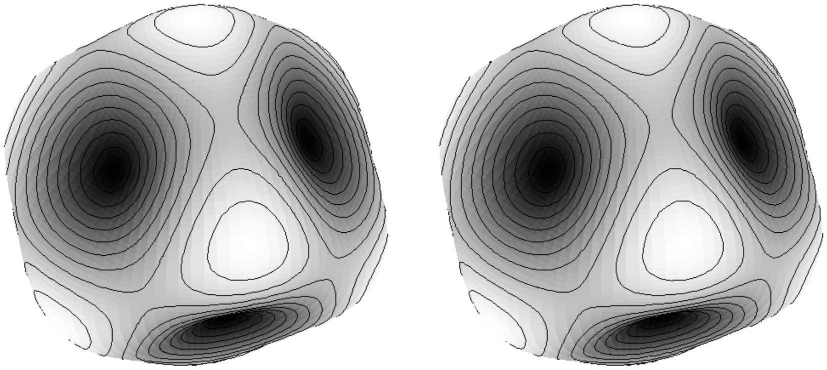

FIGURE 3.15. Sphere perturbed with $\lambda\mathcal{Y}_4^0 + \mathcal{Y}_4^3$: The mean curvature H and the surface charge density σ on the free surface. Brighter areas correspond to higher values. H and σ are constant along the contour lines. The two graphs are identical, since H and σ vary in the same manner along the surface.

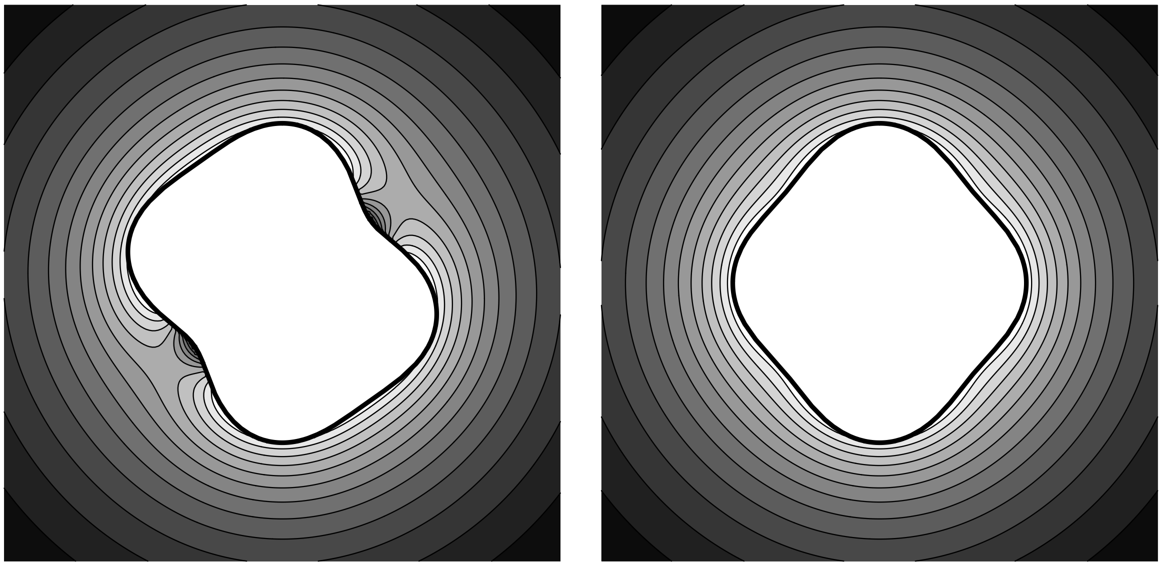

FIGURE 3.16. Sphere perturbed with $\lambda\mathcal{Y}_4^0 + \mathcal{Y}_4^3$: Contours of the potential V on the xz and yz planes. Brighter areas correspond to higher values.

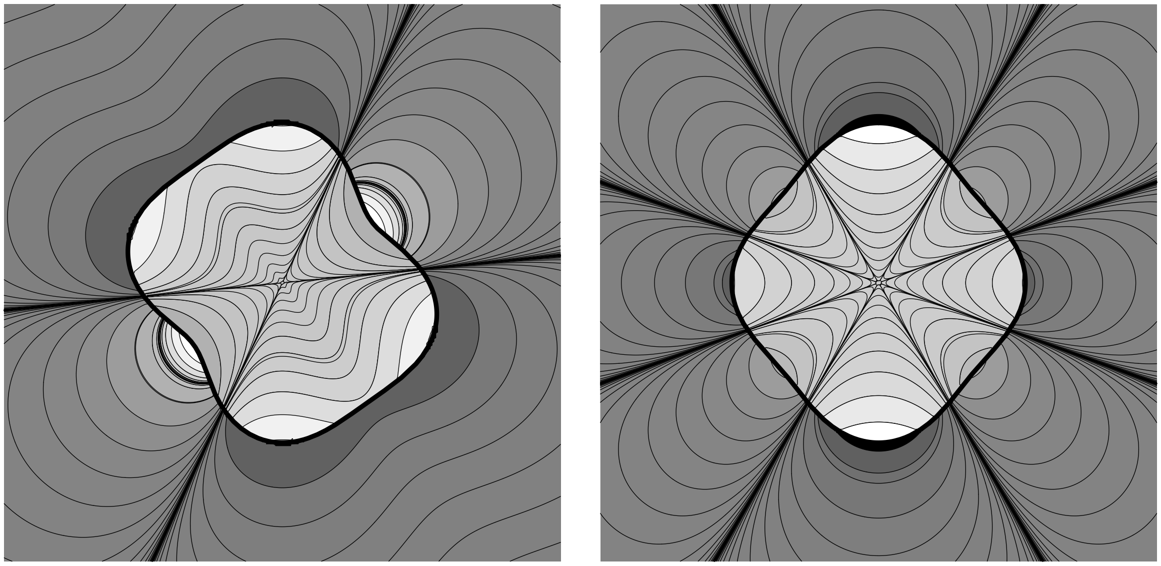

FIGURE 3.17. Sphere perturbed with $\lambda\mathcal{Y}_4^0 + \mathcal{Y}_4^3$: Contours of the pressure p of the fluid on the xz and yz planes. Brighter areas correspond to higher values.

CHAPTER 4

NUMERICAL SIMULATION WITH BEM

4.1. The Boundary Integral Equations

Although the equations of the chapter 2 are an accurate mathematical model of the physical problem, they are inconvenient with regard to their usefulness as a basis for a *numerical* treatment of the problem. For instance, note that although we only need the value of the surface charge density σ on the free boundary, equation (2.6) forces us to calculate the electric potential V (using (2.4) and (2.5)) in $\mathbb{R}^3$ as an intermediate step. Likewise, the Stokes flow equations (2.1a)-(2.1c), force us to calculate the pressure field p, since it is coupled with the velocity field $\mathbf{u}$. Again, despite the fact that we are only interested in the (2-dimensional) free boundary, we have to perform intermediate calculations in the (3-dimensional) ambient space as well. The answer to this problem is to recast the original equations as a set of *boundary integral equations* [Poz, Cun], where the unknown quantities are located only at the free boundary.

The first such equation captures the electrostatic part of the problem (eq. (2.4)-(2.7))

$$V_0 = \frac{1}{4\pi\epsilon_0} \int_{\partial D} \sigma(\mathbf{x}') K(\mathbf{x}, \mathbf{x}') ds(\mathbf{x}'), \quad \mathbf{x} \in \partial D \tag{4.1}$$

where the kernel of the integral is

$$K(\mathbf{x}, \mathbf{x}') = \frac{1}{|\mathbf{x} - \mathbf{x}'|} \tag{4.2}$$

The second equation is equivalent to the Stokes flow equations (2.1a)-(2.1c) together with the boundary condition (2.8) [Poz]. Since a number of vectors and tensors are involved, it is convenient to write it in *component form*[1]:

---

[1] The notation $\mathbf{v}_i$ denotes the ith-component ($\mathbf{v}_1$,$\mathbf{v}_2$ or $\mathbf{v}_3$) of the vector $\mathbf{v}$. Furthermore, in this and subsequent equations we make (heavy) use of the *Einstein summation convention*, whereby *repeated indices within products are summed over all possible values.*

$$\text{(4.3)}\quad \mathbf{u}_j(\mathbf{x}) = -\frac{1}{4\pi(\mu_{in}+\mu_{out})}\int_{\partial D}\Delta T_i(\mathbf{x}')\mathbb{G}_{ij}(\mathbf{x},\mathbf{x}')ds(\mathbf{x}') \\ -\frac{\mu_{out}-\mu_{in}}{4\pi(\mu_{in}+\mu_{out})}\int_{\partial D}\mathbf{u}_i(\mathbf{x}')\mathbb{T}_{ijk}(\mathbf{x},\mathbf{x}')\hat{\mathbf{n}}_k(\mathbf{x}')ds(\mathbf{x}'),\quad \mathbf{x}\in\partial D$$

where

$$\text{(4.4)}\qquad \Delta T = \left(2\gamma H - \frac{\sigma^2}{2\epsilon_0}\right)\hat{\mathbf{n}}$$

and, if we define $r = |\mathbf{x}' - \mathbf{x}|$ and $\hat{\mathbf{x}} = \dfrac{\mathbf{x}'-\mathbf{x}}{|\mathbf{x}'-\mathbf{x}|}$ and let δ_{ij} be the *Kronecker delta* symbol, we can write the kernels as [Cun]:

$$\text{(4.5)}\qquad \mathbb{G}_{ij} = \frac{\delta_{ij}}{r} + \frac{\hat{\mathbf{x}}_i\hat{\mathbf{x}}_j}{r}$$

$$\text{(4.6)}\qquad \mathbb{T}_{ijk} = -6\frac{\hat{\mathbf{x}}_i\hat{\mathbf{x}}_j\hat{\mathbf{x}}_k}{r^2}$$

The *stokeslet* $\mathbb{G}$ and the *tenselet* $\mathbb{T}$, that serve as kernels for the boundary integrals, are the *free-space Green's functions* for the Stokes flow equations and the function ΔT is the *traction* at the free boundary.

Note that as a special case, if the viscosity is the same inside and outside ($\mu_{in} = \mu_{out} = \mu$), then the equation (4.3) yields an explicit representation of the velocity

$$\text{(4.7)}\qquad \mathbf{u}_j(\mathbf{x}) = -\frac{1}{8\pi\mu}\int_{\partial D}\Delta T_i(\mathbf{x}')\mathbb{G}_{ij}(\mathbf{x},\mathbf{x}')ds(\mathbf{x}'),\quad \mathbf{x}\in\partial D$$

For the remainder of the thesis we work with this equation instead of (4.3). Numerical experiments with circular symmetry indicate that the qualitative evolution of the free boundary is independent of the ratio of the viscosities, provided that $\mu_{in} > \mu_{out}$ [Bet].

The new equations have the following advantages over the old set:

- The remaining physical quantities are never evaluated at points that lie outside of the free boundary.
- Both the electric potential V and the pressure p have been eliminated from the equations.

The main disadvantage of the boundary integral equations is the singular nature of the kernels $K(\mathbf{x},\mathbf{x}')$ in (4.1) and $\mathbb{G}(\mathbf{x},\mathbf{x}')$, $\mathbb{T}(\mathbf{x},\mathbf{x}')$ in (4.3); as the integration covers the entire free boundary, $\mathbf{x}'$ must eventually take the value $\mathbf{x}\in\partial D$ as well. Unfortunately, as $\mathbf{x}'\to\mathbf{x}$, $r\to 0$ and then

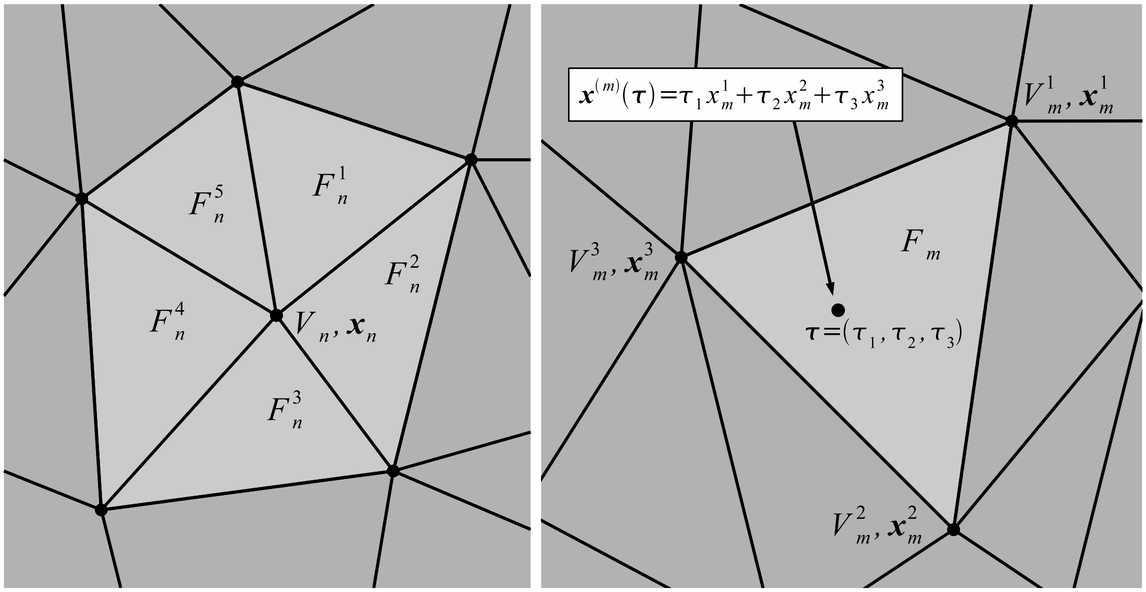

FIGURE 4.1. Structure of the mesh M close to a vertex $V_n \in \mathcal{V}$ and a face $F_m \in \mathcal{F}$. The vertex V_n is surrounded by a number of faces $\mathcal{F}_n = \{F_m^1, \ldots, F_m^N\}$ and has coordinates $\mathbf{x}_n$. The face F_m has three vertices $\mathcal{V}_m = \{V_m^1, V_m^2, V_m^3\}$ with coordinates $\mathbf{x}_m^1, \mathbf{x}_m^2, \mathbf{x}_m^3$ respectively. A point on the face with barycentric coordinates $\boldsymbol{\tau}$ has cartesian coordinates $\mathbf{x}^{(m)}(\boldsymbol{\tau})$.

the kernels diverge[2]. As a result, the boundary integrals should be handled with extreme caution [Poz2, Kat, Zin, Baz, Pel, Bet, Feng].

4.2. Discretization

Having established the boundary integral equations (4.1) and (4.3), we turn to the introduction of an appropriate discretization of both the free boundary and all the quantities $(\mathbf{u}, \sigma, H)$ that are defined on it.

We approximate the free boundary ∂D with a *triangular mesh* M. The mesh is a (three-dimensional) *polyhedron* with *vertices* $\mathcal{V} = \{V_1, \ldots, V_N\}$ and *faces* $\mathcal{F} = \{F_1, \ldots, F_M\}$ (see fig. 4.1 and 4.2). We denote the three vertices of the face $F_m \in \mathcal{F}$ with

$$\mathcal{V}_m = \{V_m^1, V_m^2, V_m^3\} \subset \mathcal{V} \tag{4.8}$$

---

[2] The kernels K and $\mathbb{G}$ diverge like r^{-1}, whereas $\mathbb{T}$ diverges like r^{-2}.

The superscripts indicate the order of the vertices as we traverse the face in the clockwise direction (as seen from outside[3] ∂D) (fig. 4.1).

Each vertex $V_n \in \mathcal{V}$ has its own set of cartesian coordinates $\mathbf{x}_n \in \mathbb{R}^3$. Furthermore, we define $\mathcal{F}_n$ to be the set of all the faces containing V_n (see fig. 4.1) :

$$\mathcal{F}_n = \{F_n^1, \dots, F_n^{N_n}\} = \{F_m \in \mathcal{F} : V_n \in \mathcal{V}_m\} \subset \mathcal{F} \tag{4.9}$$

Again, the superscripts reflect the order of the faces around V_n as we move in the clockwise direction around it (fig. 4.1). For every face $F_m \in \mathcal{F}_n$, we also define the *index* $\mathcal{I}(n,m)$ of the vertex V_n in $\mathcal{V}_m$ to be the unique integer that satisfies

$$V_m^{\mathcal{I}(n,m)} \equiv V_n \in \mathcal{V}_m \tag{4.10}$$

A useful notion is the *adjacency function* $\alpha : \mathcal{V} \times \mathcal{V} \to \{0,1\}$, defined as

$$\alpha_{ij} \equiv \alpha(V_i, V_j) = \begin{cases} 1, & \text{if } V_i, V_j \text{ are connected by an edge} \\ 0, & \text{otherwise} \end{cases} \tag{4.11}$$

Note that the α_{ij} are the elements of the *adjacency matrix* [Cha].

Finally, we define the *degree* $\deg(V_n)$ of a vertex [Cha] as

$$\deg(V_n) = |\mathcal{F}_n| \tag{4.12}$$

The underlying assumption behind this discretization is that the vertices $\mathcal{V}$ lie on ∂D, so that $\mathbf{x}_n \in \partial D$, and the rest of the surface is approximated via *linear interpolations*, to produce the faces $\mathcal{F}$ (see fig. 4.1). To be more specific, any point $\mathbf{x} \in F_m$ is a *convex linear combination* of the vertices $\mathcal{V}_m$:

$$\mathbf{x} = \mathbf{x}^{(m)}(\boldsymbol{\tau}) = \tau_1 \mathbf{x}_m^1 + \tau_2 \mathbf{x}_m^2 + \tau_3 \mathbf{x}_m^3 \tag{4.13}$$

---

[3] We assume that ∂D is an *orientable* surface, as the existence of the continuous normal vector field $\hat{\mathbf{n}}$ on ∂D implies.

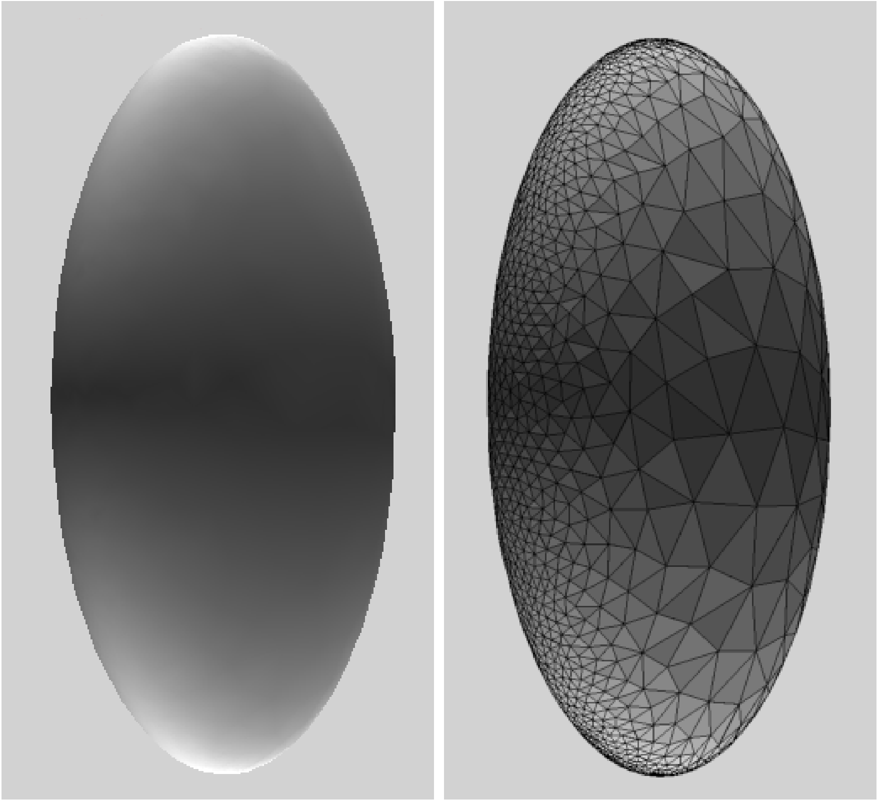

FIGURE 4.2. A surface S with a function f defined on it (represented by grayscale shading on S) and an mesh M that approximates it. The function f can be approximated by a piecewise linear function $\widetilde{f}$ on M.

where $\mathbf{x}_m^i$ is the position of the vertex $V_m^i \in \mathcal{V}_m$, and the unique $\boldsymbol{\tau} = (\tau_1, \tau_2, \tau_3)$ are the *barycentric coordinates* of the point [Cox1] with respect to the vertices $\mathcal{V}_j$, normalized[4] so that $\tau_1 + \tau_2 + \tau_3 = 1$.

The mesh M is simply the union of all the faces $F_m \in \mathcal{F}$:

$$M = \bigcup_{F_m \in \mathcal{F}} F_m \tag{4.14}$$

This leads naturally to the idea that a (real or vector valued) function f defined on ∂D can be approximated by a function $\widetilde{f}$ defined on the mesh M, if we know the value of f at the vertices:

$$f_1 = f(\mathbf{x}_1), \ldots, f_N = f(\mathbf{x}_N) \tag{4.15}$$

---

[4] When normalized, the barycentric coordinates are also called *aerial coordinates* [Cox1].

We can do this by using linear interpolation to define $\widetilde{f}$ as a piecewise linear function (see fig. 4.2). If $\mathbf{x} \in F_m$ with barycentric coordinates $\boldsymbol{\tau} = (\tau_1, \tau_2, \tau_3)$, then we let

$$\widetilde{f}(\mathbf{x}) = f^{(m)}(\boldsymbol{\tau}) = \tau_1 f_m^1 + \tau_2 f_m^2 + \tau_3 f_m^3 \tag{4.16}$$

where $f^{(m)}$ is the (linear) restriction[5] of $\widetilde{f}$ on $\mathcal{F}_m$ and $f_m^i = f(\mathbf{x}_m^i)$, $i \in \{1, 2, 3\}$, is the value of f at the vertex $V_m^i \in \mathcal{V}_m$.

4.3. The Boundary Elements Method

After approximating the free boundary ∂D by a mesh M and defining appropriate approximations on M of the various quantities of our model, we can attempt to discretize the boundary integral equations (4.1) and (4.3). The key observation is that the boundary integral of a function f over ∂D can now be approximated by the integral of its approximation f_{app} over the mesh[6] M,

$$\int_{\partial D} f(x) ds(x) \approx \int_M f_{app}(x) ds(x) = \sum_{F_m \in \mathcal{F}} \int_{F_m} f_{app}(x) ds(x) \tag{4.17}$$

where we used the fact that the mesh M is simply the union of the faces $F_m \in \mathcal{F}$.

Furthermore, the integral of a function f defined over a triangle F_m can be estimated by a finite sum with the use of a *quadrature formula*

$$\int_{F_m} f(\mathbf{x}) ds(\mathbf{x}) \approx \sum_{p=1}^{P} f(\mathbf{x}^{(m)}(\boldsymbol{\tau}_p)) A_m w_p \tag{4.18}$$

where P is the number of *quadrature points*, $\boldsymbol{\tau}_p = (\tau_1^p, \tau_2^p, \tau_3^p)$ their *barycentric coordinates*, w_p their *integration weights* and A_m is the *area* of the face F_m (see fig. 4.3).

The area A_m of a face F_m, used in (4.18), can be calculated by

$$A_m = \frac{1}{2} \left| (\mathbf{x}_m^2 - \mathbf{x}_m^1) \times (\mathbf{x}_m^3 - \mathbf{x}_m^1) \right| \tag{4.19}$$

and the normal $\hat{\mathbf{n}}_m$ of the face is given by the normalized cross product

$$\hat{\mathbf{n}}_m = \frac{(\mathbf{x}_m^2 - \mathbf{x}_m^1) \times (\mathbf{x}_m^3 - \mathbf{x}_m^1)}{|(\mathbf{x}_m^2 - \mathbf{x}_m^1) \times (\mathbf{x}_m^3 - \mathbf{x}_m^1)|} \tag{4.20}$$

---

[5] Expressed in the local (barycentric) coordinates $\boldsymbol{\tau}_1, \boldsymbol{\tau}_2, \boldsymbol{\tau}_3$.

[6] This is where the *boundary elements method* takes its name from; we replace the boundary integrals over ∂D with finite sums of integrals over the boundary elements F_m.

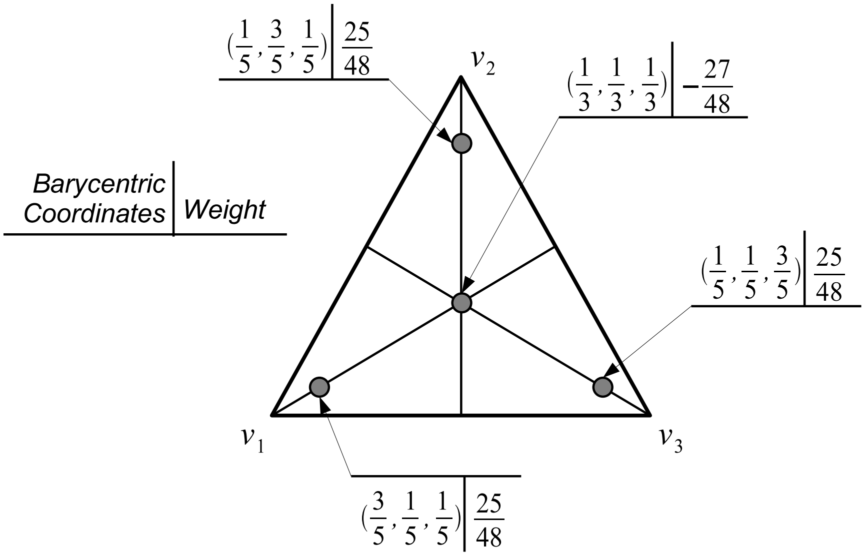

Figure 4.3. A four-point quadrature formula for triangular domains. We list the barycentric coordinates $\boldsymbol{\tau}_p = (\tau_1^p, \tau_2^p, \tau_3^p)$ of the quadrature points and their corresponding weights w_p, for $p = 1, \ldots, 4$. The accuracy of the formula is $\mathrm{O}(L^4)$, where L is the typical side length of the triangle.

By replacing the integral over ∂D with a sum of quadratures over the F_m and substituting σ with its linear approximations on M, we can turn equation (4.1) into

$$V_0 = \frac{1}{4\pi\epsilon_0} \sum_{F_m \in \mathcal{F}} \sum_{p=1}^{P} \sigma^{(m)}(\boldsymbol{\tau}_p) K\left(\mathbf{x}, \mathbf{x}^{(m)}(\boldsymbol{\tau}_p)\right) A_m w_p, \quad \mathbf{x} \in M \tag{4.21}$$

or, after expanding $\sigma^{(m)}(\boldsymbol{\tau}_p)$,

$$V_0 = \frac{1}{4\pi\epsilon_0} \sum_{F_m \in \mathcal{F}} \sum_{p=1}^{P} \left(\sigma_m^1 \tau_1^p + \sigma_m^2 \tau_2^p + \sigma_m^3 \tau_3^p\right) K\left(\mathbf{x}, \mathbf{x}^{(m)}(\boldsymbol{\tau}_p)\right) A_m w_p, \quad \mathbf{x} \in M \tag{4.22}$$

Now, keeping in mind that for any $i \in \{1, 2, 3\}$ and $F_m \in \mathcal{F}$, there exists a $V_n \in \mathcal{V}$ such that $\sigma_m^i = \sigma_m^{\mathcal{I}(n,m)} \equiv \sigma_n$, we can reorganize the sums in (4.22) like this:

$$V_0 = \frac{1}{4\pi\epsilon_0} \sum_{V_n \in \mathcal{V}} \left(\sum_{F_m \in \mathcal{F}_n} \sum_{p=1}^{P} \tau_{\mathcal{I}(n,m)}^p K\left(\mathbf{x}, \mathbf{x}^{(m)}(\boldsymbol{\tau}_p)\right) A_m w_p \right) \sigma_n, \quad \mathbf{x} \in M \tag{4.23}$$

The unknown quantities in equation (4.23) are the values of the surface charge density σ_n at the vertices $V_n \in \mathcal{V}$. We can derive a (linear) system of N equations with N unknowns, by setting $\mathbf{x} = \mathbf{x}_n \in M$ in (4.23) for every vertex[7] $V_n \in \mathcal{V}$:

$$4\pi\epsilon_0 V_0 = \sum_{V_t \in \mathcal{V}} \mathbb{A}_{nt}\sigma_t, \quad V_n \in \mathcal{V} \tag{4.24}$$

where the coefficient matrix $\mathbb{A}$ of the linear system is given by

$$\mathbb{A}_{nt} = \sum_{F_m \in \mathcal{F}_t} \sum_{p=1}^{P} \tau^p_{\mathcal{I}(t,m)} K\left(\mathbf{x}_n, \mathbf{x}^{(m)}(\boldsymbol{\tau}_p)\right) A_m w_p, \quad V_n, V_t \in \mathcal{V} \tag{4.25}$$

Following a similar discretization procedure, the boundary integral equation (4.7) becomes

$$\mathbf{u}_j(\mathbf{x}_n) = -\frac{1}{8\pi\mu} \sum_{F_m \in \mathcal{F}} \sum_{p=1}^{P} \Delta T^{(m)}(\boldsymbol{\tau}_p)\hat{\mathbf{n}}^m_i \mathbb{G}_{ij}\left(\mathbf{x}_n, \mathbf{x}^{(m)}(\boldsymbol{\tau}_p)\right) A_m w_p, \quad V_n \in \mathcal{V} \tag{4.26a}$$

$$\Delta T^{(m)}(\boldsymbol{\tau}_p) = 2\gamma H^{(m)}(\boldsymbol{\tau}_p) - \frac{1}{2\epsilon_0}\left(\sigma^{(m)}(\boldsymbol{\tau}_p)\right)^2 \tag{4.26b}$$

where we have replaced σ and H with their linear approximations on F_m and the normal vector $\hat{\mathbf{n}}$ at a point on F_m with the normal vector $\hat{\mathbf{n}}_m = (\hat{\mathbf{n}}^m_1, \hat{\mathbf{n}}^m_2, \hat{\mathbf{n}}^m_3)$ of the face itself. Note that the right hand side is free of the velocities $\mathbf{u}_n$ at the vertices, so we can calculate them directly if we know the mean curvature H_n and the surface charge density σ_n at all the vertices $V_n \in \mathcal{V}$.

Singularity Removal

Unfortunately, the equations above can not be used in practice, as they are. The reason is the singular nature of the kernels $K(\mathbf{x}, \mathbf{x}')$ in (4.1) and $\mathbb{G}$ in (4.7). Specifically, consider the calculation of $\mathbb{A}_{nt}$ in equation (4.25), when $\mathcal{F}_n \cap \mathcal{F}_t \neq \emptyset$. In this case we need to calculate the quantity $K\left(\mathbf{x}_n, \mathbf{x}^{(m)}(\boldsymbol{\tau}_p)\right)$ where both $\mathbf{x}_n \in F_m$ and $\mathbf{x}^{(m)}(\boldsymbol{\tau}_p) \in F_m$. Since the two points belong to the same face, the distance r between them can become zero, resulting in the divergence of $K\left(\mathbf{x}_n, \mathbf{x}^{(m)}(\boldsymbol{\tau}_p)\right) = r^{-1}$. This results in the numerical error of the integration becoming very large, and the loss of convergence as we refine the mesh M.

This situation can be resolved by using the *singularity removal* technique. Consider the part of the boundary integral of (4.1) that corresponds to the face F_m and furthermore assume that the collocation point $\mathbf{x}' \equiv \mathbf{x}^i_m$ is one of the vertices V^i_m of the face F_m. We can rewrite the

---

[7] In common BEM terminology, we choose the vertices V_n as the *collocation points* of our method.

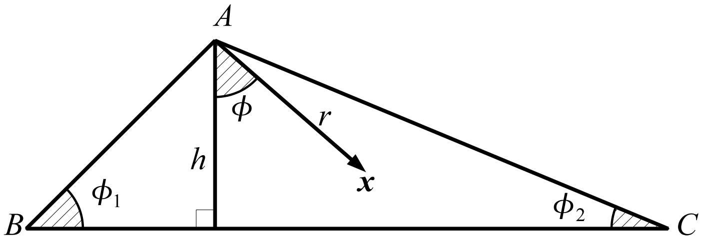

FIGURE 4.4. The triangle ABC of equation (4.31). The integral of r^{-1} over the triangle is calculated by using the polar coordinates (r, ϕ) pictured above.

integral as follows:

$$\begin{aligned}\int_{F_m} \sigma(\mathbf{x}')K(\mathbf{x}^i_m, \mathbf{x}')ds(\mathbf{x}') &= \int_{F_m} (\sigma(\mathbf{x}') - \sigma^i_m)K(\mathbf{x}^i_m, \mathbf{x}')ds(\mathbf{x}') + \sigma^i_m \int_{F_m} K(\mathbf{x}^i_m, \mathbf{x}')ds(\mathbf{x}') \\ &= \int_{F_m} \frac{\sigma(\mathbf{x}') - \sigma^i_m}{|\mathbf{x}' - \mathbf{x}^i_m|} ds(\mathbf{x}') + \sigma^i_m \int_{F_m} \frac{ds(\mathbf{x}')}{|\mathbf{x}' - \mathbf{x}^i_m|}\end{aligned} \tag{4.27}$$

If we assume that the surface charge density σ is a *Lipschitz function* then

$$|\sigma(\mathbf{x}') - \sigma(\mathbf{x})| \le C\,|\mathbf{x}' - \mathbf{x}|\,, \quad C > 0,\, \mathbf{x}', \mathbf{x} \in \partial D \tag{4.28}$$

It follows that the integrand of the first integral is bounded

$$\frac{\sigma(\mathbf{x}') - \sigma^i_m}{|\mathbf{x}' - \mathbf{x}^i_m|} \le C \tag{4.29}$$

and therefore we can safely calculate it numerically:

$$\begin{aligned}\int_{F_m} \frac{\sigma(\mathbf{x}') - \sigma^i_m}{|\mathbf{x}' - \mathbf{x}^i_m|} ds(\mathbf{x}') &= \int_{F_m} (\sigma(\mathbf{x}') - \sigma^i_m)K(\mathbf{x}', \mathbf{x}^i_m)ds(\mathbf{x}') \\ &\approx \sum_{p=1}^{P} (\sigma^{(m)}(\boldsymbol{\tau}_p) - \sigma^i_m)K\left(x^{(m)}(\boldsymbol{\tau}_p), \mathbf{x}^i_m\right) A_m w_p\end{aligned} \tag{4.30}$$

The second integral in (4.27) can be calculated analytically. Specifically, the integral of r^{-1}, where r is measured from the vertex A, over a triangle ABC (fig. 4.4) is

$$\begin{aligned}\int_{ABC} \frac{ds(\mathbf{x})}{|\mathbf{x}_A - \mathbf{x}|} &= h \int_{-\theta_1}^{\theta_2} \frac{d\phi}{\cos(\phi)} \\ &= h\left(\tanh^{-1}(\cos(\phi_1)) + \tanh^{-1}(\cos(\phi_2))\right)\end{aligned} \tag{4.31}$$

where $\theta_1 = \frac{\pi}{2} - \phi_1$ and $\theta_2 = \frac{\pi}{2} - \phi_2$.

Putting everything together, when the collocation point $\mathbf{x} \equiv \mathbf{x}_m^i$ lies on the face F_m then

$$\int_{F_m} \sigma(\mathbf{x}')K(\mathbf{x},\mathbf{x}')ds(\mathbf{x}') \approx \sum_{p=1}^{P}(\sigma^{(m)}(\boldsymbol{\tau}_p) - \sigma_m^i)K\left(x^{(m)}(\boldsymbol{\tau}_p), \mathbf{x}_m^i\right) A_m w_p + \sigma_m^i S_m^i \tag{4.32}$$

where S_m^i denotes the integral

$$S_m^i = \int_{F_m} \frac{ds(\mathbf{x}')}{|\mathbf{x}' - \mathbf{x}_m^i|}$$

calculated with (4.31).

The coefficients of the linear system (4.24) remain the same, except for the diagonal entries which become

$$\mathbb{A}_{nn} = \sum_{F_m \in \mathcal{F}_n} \left(\sum_{p=1}^{P} \left(\tau_{\mathcal{I}(n,m)}^p - 1\right) K\left(\mathbf{x}_n, \mathbf{x}^{(m)}(\boldsymbol{\tau}_p)\right) A_m w_p + S_m^{\mathcal{I}(n,m)} \right), \quad V_n \in \mathcal{V} \tag{4.33}$$

Equation (4.26a) suffers from a similar singularity as (4.21), since the kernel $\mathbb{G}(\mathbf{x},\mathbf{x}')$ is also singular. It follows that we need to apply the singularity removal technique in this case as well. The key observation is the fact that when the collocation point $\mathbf{x}' \equiv \mathbf{x}_m^i$ lies on the face, then

$$\begin{aligned} \hat{\mathbf{n}}_i^m \mathbb{G}_{ij} &= \hat{\mathbf{n}}_i^m \left(\frac{\delta_{ij}}{r} + \frac{\hat{\mathbf{x}}_i \hat{\mathbf{x}}_j}{r} \right) \\ &= \frac{\hat{\mathbf{n}}_i^m \delta_{ij}}{r} + \frac{\hat{\mathbf{n}}_i^m \hat{\mathbf{x}}_i \hat{\mathbf{x}}_j}{r} \\ &= \frac{\hat{\mathbf{n}}_j^m}{r} + \frac{(\hat{\mathbf{n}}_m \cdot \hat{\mathbf{x}})\hat{\mathbf{x}}_j}{r} \end{aligned} \tag{4.34}$$

The dot product $\hat{\mathbf{n}}_m \cdot \hat{\mathbf{x}}$ vanishes, since the vector $\hat{\mathbf{x}}$ lies on the same plane with the face and is therefore perpendicular to the normal vector $\hat{\mathbf{n}}_m$. Hence

$$\hat{\mathbf{n}}_i^m \mathbb{G}_{ij} = \frac{\hat{\mathbf{n}}_j^m}{r} \tag{4.35}$$

and, after the singularity removal, equation (4.26a) becomes

$$\begin{aligned} \mathbf{u}_j(\mathbf{x}_n) = &-\frac{1}{8\pi\mu} \sum_{F_m \in \mathcal{F} \setminus \mathcal{F}_n} \sum_{p=1}^{P} \Delta T^{(m)}(\boldsymbol{\tau}_p) \hat{\mathbf{n}}_i^m \mathbb{G}_{ij}\left(\mathbf{x}_n, \mathbf{x}^{(m)}(\boldsymbol{\tau}_p)\right) A_m w_p \\ &- \frac{1}{8\pi\mu} \sum_{F_m \in \mathcal{F}_n} \left\{ \sum_{p=1}^{P} \frac{\Delta T^{(m)}(\boldsymbol{\tau}_p) - \Delta T_n}{|\mathbf{x}^{(m)}(\boldsymbol{\tau}_p) - \mathbf{x}_n|} A_m w_p + \Delta T_n S_m^{\mathcal{I}(n,m)} \right\} \hat{\mathbf{n}}_j^m \end{aligned} \tag{4.36}$$

with S_m^i defined as in (4.32) and

$$\Delta T_n = 2\gamma H_n - \frac{1}{2\epsilon_0}(\sigma_n)^2 \tag{4.37}$$

The BEM algorithm

At this point, we can outline an algorithm for tracking the evolution of the free boundary (algorithm 1).

Algorithm 1 Tracking the Evolution of the Free Boundary with BEM.

```
Input: The position of all the vertices $\mathbf{x}_n$ at an initial time $t_0$.
1: $t \leftarrow t_0$
2: while $t < t_{max}$ do
3:     Calculate the surface charge density $\sigma_n$ at the vertices, by solving the linear system (4.24)
       numerically.
4:     Calculate the mean curvature $H_n$ at the vertices using the iterative paraboloid fitting
       method (see section 4.4).
5:     Calculate the velocity $\mathbf{u}_n$ at the vertices using equation (4.36).
6:     Select an appropriate time step $\Delta t$ and numerically integrate the system of ODEs
           $\frac{d\mathbf{x}_n}{dt} = \mathbf{u}_n, \quad V_n \in \mathcal{V}$
       to find the position $\mathbf{x}_n$ of the vertices at the new time $t + \Delta t$.
7:     $t \leftarrow t + \Delta t$
Output: The position of the vertices $\mathbf{x}_n$ at a final time $t_{max}$.
```

The linear system at step 3 can be solved numerically by using either a direct (eg. LU decomposition) or iterative (eg. Gauss-Seidel) method. We use the *successive over-relaxation* (SOR) iterative method [Eng].

The numerical integration of the ODEs at step 6 can be performed using the Euler method, a Runge-Kutta method or even a predictor-corrector scheme [Eng]. We use the *improved Euler-Cauchy method*, which is a second order Runge-Kutta method.

Regardless of the method used, the choice of the time step Δt is critical for the stability of the algorithm. The basic condition that should be satisfied is that *the displacement of any vertex during a single time step should be smaller than the length of any edge that is connected to the vertex*:

$$\Delta t < \min_{V_i \in \mathcal{V}} \frac{d_i}{|\mathbf{u}(\mathbf{x}_i)|} \tag{4.38}$$

where $\mathbf{u}(\mathbf{x}_i)$ is the velocity of the fluid at the vertex V_i and d_i is the length of the shortest edge of the vertex:

$$d_i = \min_{\substack{V_j \in \mathcal{V} \\ \alpha_{ij} \neq 0}} |\mathbf{x}_i - \mathbf{x}_j| \tag{4.39}$$

The stability analysis in chapter 2 introduced a *characteristic time* τ for the model, defined as

$$\tau = \frac{R\mu}{\gamma} \tag{4.40}$$

where R is the "size" of the droplet.[8] In addition to the condition (4.38), we require that the time step should not be larger than a fraction of τ:

$$\Delta t < c\tau \tag{4.41}$$

for a fixed constant $0 < c < 1$.

4.4. Iterative Paraboloid Fitting

The accuracy of algorithm 1 is heavily dependent on the accuracy with which the *mean curvature* H is estimated at the vertices of the mesh M. There are many methods to estimate H on a triangulated surface [Sur]. We describe here the *iterative paraboloid fitting* method.

The method is based on the notion of the *osculating paraboloid*[9] [DoC, Sur] of a twice-differentiable surface $S \subseteq \mathbb{R}^3$ at one of its points $\mathbf{x}$. If we define a coordinate system with the origin at $\mathbf{x}$ and the z axis aligned with the normal vector $\hat{\mathbf{n}}$, then the surface is locally the graph

---

[8] In practice, we can let R be the largest linear dimension of the droplet or even the cube root of its volume.

[9] Note that beyond the surfaces of revolution (see fig. 4.5) that are commonly associated with the term, there are also *elliptic* paraboloids, which are not axisymmetric, as well as *hyperbolic* paraboloids, which are saddle surfaces. It follows that the osculating paraboloid can have a number of different shapes.

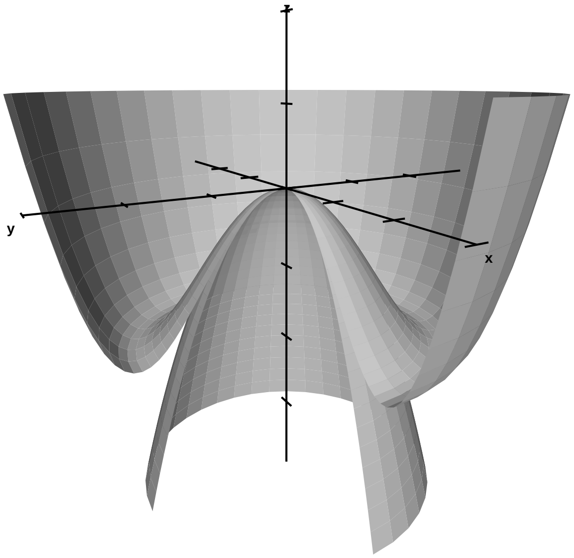

FIGURE 4.5. A surface (top) and its osculating paraboloid (bottom) in local coordinates. The surface and its osculating paraboloid have the same mean curvature H and normal vector $\hat{\mathbf{n}}$ at the contact point. A section of the two surfaces is missing, to allow an unobstructed view of the contact point at the origin.

of a function of the form $z = f(x, y)$. Neglecting third and higher order terms in the Taylor series of f, we get the following approximation of the surface:

$$z = ax^2 + bxy + cy^2 \tag{4.42}$$

where

$$a = \frac{1}{2}\frac{\partial^2 f}{\partial x^2}, \quad b = \frac{\partial^2 f}{\partial x \partial y}, \quad c = \frac{1}{2}\frac{\partial^2 f}{\partial y^2} \tag{4.43}$$

The quadratic surface (4.42) is the osculating paraboloid (fig. 4.5).

If the z axis of the local coordinate system is not perfectly aligned with the normal vector $\hat{\mathbf{n}}$ of the surface S, then the osculating paraboloid has an equation of the form[10]

$$z = ax^2 + bxy + cy^2 + dx + ey \tag{4.44}$$

---

[10] Assuming that the surface S has the form $z = f(x, y)$ in the local coordinates.

The mean curvature H of the paraboloid at the origin is

$$H = \frac{(1+e^2)a - bed + (1+d^2)c}{(1+d^2+e^2)^{3/2}} \tag{4.45}$$

and its normal vector at the origin (in local coordinates) is

$$\hat{\mathbf{n}}_P = \left(-\frac{d}{\sqrt{1+d^2+e^2}}, -\frac{e}{\sqrt{1+d^2+e^2}}, \frac{1}{\sqrt{1+d^2+e^2}}\right) \tag{4.46}$$

The key observation is that the mean curvature and normal vector of the surface at the point $\mathbf{x}$ are equal to the mean curvature (4.45) and the normal vector (4.46) of the osculating paraboloid at the origin [DoC].

Algorithm 2 Iterative Paraboloid Fitting

```
Input: The coordinates $\mathbf{x}$ of a vertex and $\mathbf{x}_1, \ldots, \mathbf{x}_n$ of its neighboring vertices, an estimate of
    the normal vector $\hat{\mathbf{n}}$ of $S$ at $\mathbf{x}$, and the tolerance $e_{max}$.
repeat
    Transform the $\mathbf{x}_i$ so that $\mathbf{x} \to O$ and $\hat{\mathbf{n}} \to \hat{\mathbf{z}}$.
    Perform a linear least squares fitting of the function $z(x,y) = ax^2 + bxy + cy^2 + dx + ey$
    on the vertices $\mathbf{x}_1, \ldots, \mathbf{x}_n$ to find $(a,b,c,d,e)$.
    $\hat{\mathbf{n}}_P \leftarrow \left(-\frac{d}{\sqrt{1+d^2+e^2}}, -\frac{e}{\sqrt{1+d^2+e^2}}, \frac{1}{\sqrt{1+d^2+e^2}}\right)$
    Return $\hat{\mathbf{n}}_P$ to the original coordinates.
    $e \leftarrow |\hat{\mathbf{n}}_P - \hat{\mathbf{n}}|$
    $\hat{\mathbf{n}} \leftarrow \hat{\mathbf{n}}_P$
until $e < e_{max}$
$H \leftarrow \frac{(1+e^2)a - bed + (1+d^2)c}{(1+d^2+e^2)^{3/2}}$
Output: The coefficients of the osculating paraboloid $(a,b,c,d,e)$, the mean curvature $H$ and
    the normal vector $\hat{\mathbf{n}}$ of $S$ at the vertex.
```

The iterative paraboloid fitting method (algorithm 2) calculates the mean curvature H and normal vector $\hat{\mathbf{n}}$ at a vertex V of the mesh, given the coordinates $\mathbf{x}$ of V and the coordinates $(\mathbf{x}_1, \ldots, \mathbf{x}_n)$ of the adjacent vertices. If we have an initial estimate of the normal vector $\hat{\mathbf{n}}$ of the surface at $\mathbf{x}$, we can change the coordinates so that V is at the origin and $\hat{\mathbf{n}}$ is aligned with the z-axis. By performing a *linear least squares fitting* [Eng] of (4.44) on the new coordinates $(\mathbf{x}'_1, \ldots, \mathbf{x}'_n)$ of the adjacent vertices, we can estimate the coefficients (a, b, c, d, e) of the osculating paraboloid. Then (4.46) yields a new estimate for the normal vector at $\mathbf{x}$ and we can restart the process. We iterate until the successive $\hat{\mathbf{n}}$ converge[11] and then we use (4.45) to estimate the mean curvature H of the surface at $\mathbf{x}$. The normal vector calculated during the last iteration can be used as an estimate of the normal vector of the surface at $\mathbf{x}$.

A transformation that satisfies the conditions of step 2 of the algorithm is the composition of a *translation* by $-\mathbf{x}$,

$$\mathbf{x}_i \leftarrow \mathbf{x}_i - \mathbf{x} \tag{4.47}$$

and a *rotation* by 180° around the *half-way vector*

$$\hat{\mathbf{h}} = \frac{\hat{\mathbf{n}} + \hat{\mathbf{z}}}{|\hat{\mathbf{n}} + \hat{\mathbf{z}}|} \tag{4.48}$$

The rotation can be written as[12]

$$\mathbf{x}_i \leftarrow \mathbf{x}_i - (\hat{\mathbf{h}} \cdot \mathbf{x}_i)\hat{\mathbf{h}} \tag{4.49}$$

Step 5 of the algorithm can be performed easily by simply applying the rotation around $\hat{\mathbf{h}}$ on $\hat{\mathbf{n}}_P$.

4.5. The Adaptive Mesh

To accurately keep track of the evolution of the free boundary with algorithm 1, one must ensure that the mesh M satisfies certain appropriate conditions [Tho, Chu]. In this section we introduce these conditions, as well as the procedures that we use to enable the mesh to adapt to changes in the geometry of the evolving free boundary.

Intuitively, it is clear that the triangles that make up the mesh should be "small enough" for the mesh to be a good approximation of the free boundary. In a search for a *characteristic length* with which one could measure exactly how small "small enough" is, the local *radius of curvature* stands out. The radius of curvature ρ at a point $\mathbf{x}$ of a *curve* γ is defined as the reciprocal of

---

[11] If the mesh is not "smooth" enough, there is a chance the $\hat{\mathbf{n}}_P$ might not converge. In practice we deal with this by forcing the mesh to satisfy certain appropriate conditions. See section 4.5.

[12] This is a special case of the general rotation formula in [Wei1], for $\Phi = \pi$ and $\hat{\mathbf{n}} = \hat{\mathbf{h}}$.

the curvature κ at that point [DoC]. For a surface S, there are two radii of curvature ρ_1 and ρ_2, derived from the two principal curvatures κ_1 and κ_2. For our purposes, we let

$$\rho =\in \{\rho_1, \rho_2\} \tag{4.50}$$

be *the* local radius of curvature at a point of S. The radius of curvature ρ can be calculated by using the output of the *iterative paraboloid fitting* method (see algorithm 3). The calculation is based on the fact that the principal curvatures κ_1, κ_2 are the solutions of the quadratic

$$x^2 + Kx + H = 0 \tag{4.51}$$

where K and H are the Gaussian and mean curvatures respectively.[13]

Algorithm 3 Radius of Curvature

```
Input: The coefficients $(a, b, c, d, e)$ of the osculating paraboloid at a vertex $V_i$.
1: Calculate the mean curvature $H$:
   $H \leftarrow \frac{(1+e^2)a - bed + (1+d^2)c}{(1+d^2+e^2)^{3/2}}$
2: Calculate the Gaussian curvature $K$:
   $K \leftarrow \frac{4ac - b^2}{(1+d^2+e^2)^2}$
3: Calculate the maximum principal curvature $\kappa_{max} := \max\{|\kappa_1|, |\kappa_2|\}$:
   $\kappa_{max} \leftarrow |H| + \sqrt{H^2 - K}$
4: $\rho \leftarrow \frac{1}{\kappa_{max}}$
Output: The radius of curvature $\rho_i$ at the vertex.
```

We can quantify the requirement that the size of the triangles should be "small enough" by requiring that the length L of any edge of the mesh should be smaller than a specified fraction $c > 0$ of the local radius of curvature:

$$L \leq c\rho \tag{4.52}$$

Smaller values of c imply a finer triangulation and therefore higher accuracy. An advantage of (4.52) over a uniform bound of the form $L \leq c$ is that it allows the triangulation to be relatively

---

[13] Follows immediately from the definitions $H = \frac{\kappa_1 + \kappa_2}{2}$ and $K = \kappa_1 \kappa_2$ [DoC].

coarse in areas of low curvature, while ensuring high resolution in areas of high curvature. Given that the "interesting" part of the free boundary is exactly the high curvature areas, the condition (4.52) yields a good compromise between accuracy and reasonable computation times.

It is a well known fact that the accuracy and stability of the boundary elements method suffer greatly in the presence of *thin triangles*, ie. triangles where one of the angles is very small. An equivalent definition is that a triangle is "thin" when the ratio of two of its edges is very small. Hence, we require that the triangles of the mesh should be as close to being equilateral as possible. We can combine this requirement with (4.52), by requiring that all the sides of the triangle be comparable with the local radius of curvature (times a constant c_{cond}) and consequently with each other. We define the *condition of the mesh M* as

$$\operatorname{cond}(M) = \frac{1}{2N_{edges}} \sum_{\substack{V_i, V_j \in \mathcal{V} \\ \alpha_{ij} \neq 0}} \left| 1 - \frac{c_{cond}\rho_{ij}}{d_{ij}} \right| \tag{4.53}$$

where N_{edges} is the number of edges, α_{ij} is the adjacency function (4.11) and

$$d_{ij} = |\mathbf{x}_i - \mathbf{x}_j| \tag{4.54}$$

$$\rho_{ij} = \frac{\rho_i + \rho_j}{2} \tag{4.55}$$

and we require that the mesh M should have a minimal $\operatorname{cond}(M)$. Again, a smaller constant c_{cond} implies a finer triangulation and thus higher accuracy, coupled with longer computation times.

Another condition that the mesh M must satisfy is that for any vertex $V_i \in \mathcal{V}$, its degree must be strictly larger than 4:

$$\deg(V_i) > 4 \tag{4.56}$$

The reason is that since the osculating paraboloid equation (4.44) has 5 parameters, we need at least 5 different equations in step 3 of algorithm 2 for the nonlinear square fit to work properly. It is relatively straightforward to remove all the 3- and 4-degree vertices from a mesh and therefore we assume that the mesh always satisfies condition (4.56).

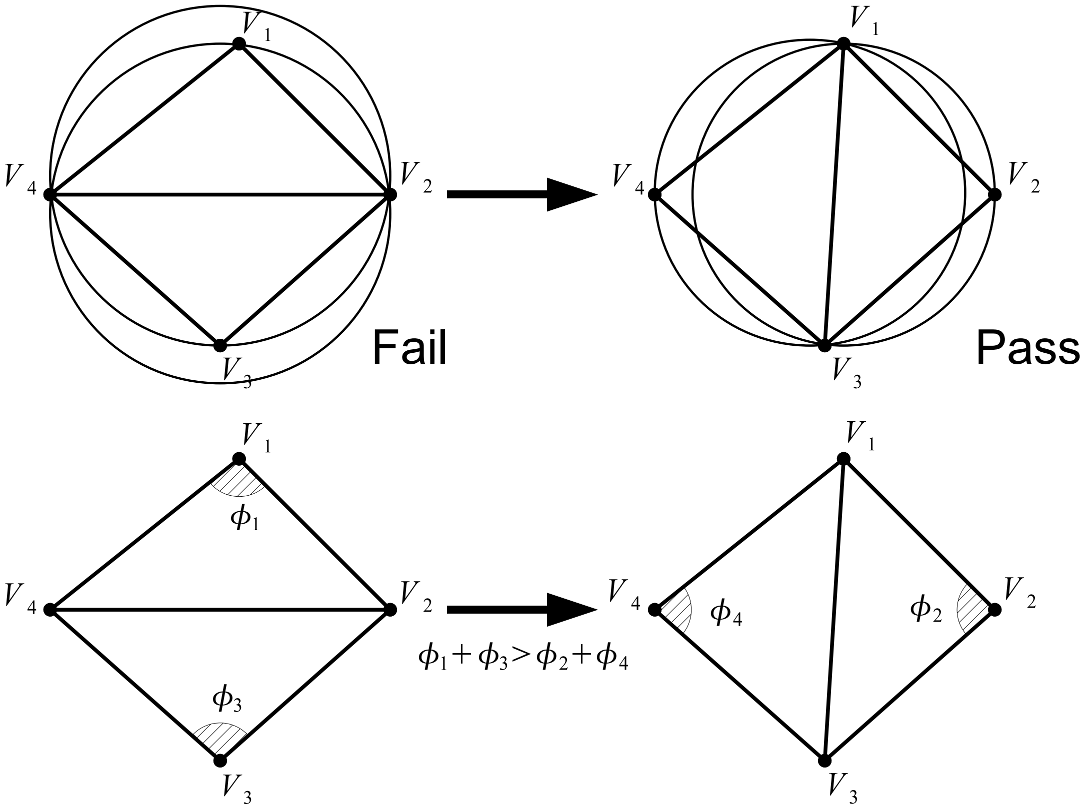

FIGURE 4.6. The Delaunay criterion requires that the interior of the circumcircle of the faces should be free of any vertices. An *edge flip* can rectify a configuration of two faces that fails the criterion. We can restate the criterion in terms of the angles of the faces.

We should also note that in general it is advantageous when the degree of the vertex is not very large either. Fortunately, if $\mathrm{cond}(M)$ is sufficiently small then all the triangles are almost equilateral and therefore the mesh is locally (almost) *regular*. This implies that the degrees of the vertices should be on average equal to six, which is the degree of the vertices of a *regular triangular grid*:

$$\deg(V_i) \approx 6 \tag{4.57}$$

In the rest of this section, we introduce the three procedures that we use to control the condition of the mesh.

Delaunay Remeshing

Given a number of points on a plane, there are many ways one can connect them to form a triangulation. There exists a unique triangulation T such that *the circumcircle of any triangle in T does not contain any vertices of T in its interior* (fig. 4.6), and it is called the *Delaunay triangulation* [Ber]. The Delaunay triangulation is *angle-optimal*, which means that its *minimal angle*, ie. the smallest among the angles of all of its triangles, is maximal among all the other possible triangulations.[14] It follows that the Delaunay triangulation is optimal in avoiding thin triangles.

Given an initial (non-Delaunay) triangulation T_0, we can find the Delaunay triangulation by applying a sequence of *edge flips* (fig. 4.6). Note that we perform an edge flip whenever the sum of the two angles on each side of the new edge is smaller than the sum of the corresponding angles on each side of the current edge, which is equivalent to the circumcircle criterion. When there are no more possible edge flips, the triangulation is angle-optimal.

Algorithm 4 Delaunay Remeshing

```
Input: The initial mesh $M$.
repeat
    for all edges $e$ do
        The edge $e$ is the diagonal $V_2V_4$ of a quadrilateral $V_1V_2V_3V_4$ (see fig. 4.6).
        $\phi_1 \leftarrow \widehat{V_4V_1V_2}$; $\phi_2 \leftarrow \widehat{V_1V_2V_3}$; $\phi_3 \leftarrow \widehat{V_2V_3V_1}$; $\phi_4 \leftarrow \widehat{V_3V_4V_1}$
        $\omega_1 \leftarrow (V_4V_1\widehat{V_2, V_2}V_3V_1)$; $\omega_2 \leftarrow (V_1V_2\widehat{V_3, V_3}V_4V_1)$
        if $\phi_1 + \phi_3 + |\pi - \omega_1| > \phi_2 + \phi_4 + |\pi - \omega_2|$ and $V_1, V_3$ are not connected then
            Replace the faces $(V_4, V_1, V_2)$ and $(V_4, V_1, V_2)$ with two new faces $(V_1, V_2, V_3)$ and $(V_3, V_4, V_1)$.
until no edges were replaced in this iteration.
Output: A mesh $M'$.
```

Regarding the related problem of connecting points on a *surface* instead of a plane, we can apply the same process. As long as the triangulation is locally almost planar (if the condition

---

[14] See [Ber] for a more precise definition based on the *angle-vector* of the triangulation.

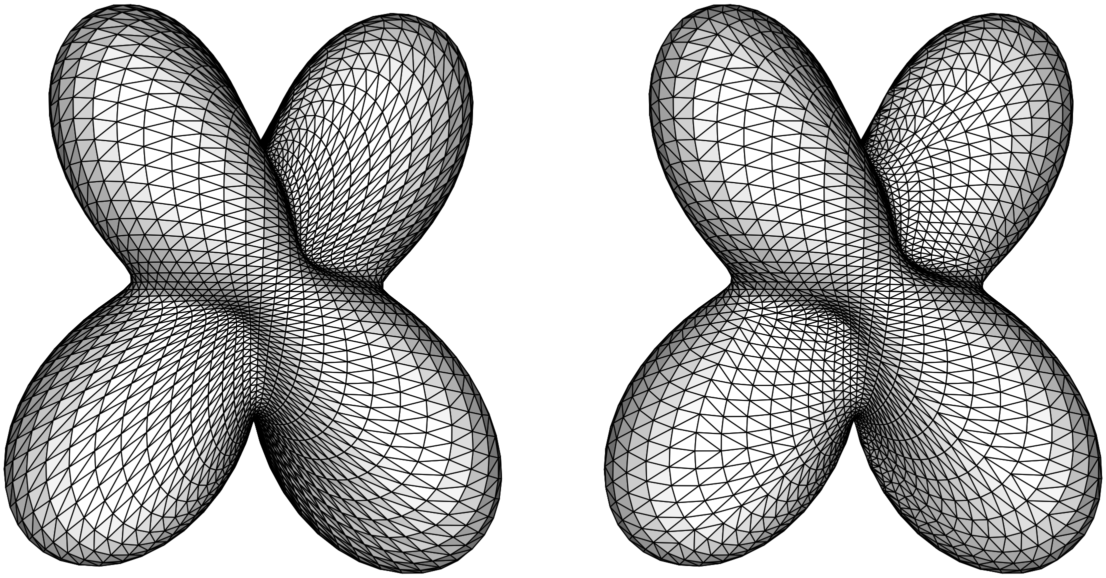

FIGURE 4.7. A mesh before and after the application of Delaunay remeshing (algorithm 4). The purpose of remeshing is to reduce the presence of "thin" triangles in the mesh and to make it as much (locally) planar as possible.

(4.52) is met) then one can expect beneficial results similar to the planar case. Nevertheless, if the triangulation is (locally) far from being planar, then the effects of edge flipping might actually be detrimental. We can compensate for this by penalizing any deviations from local planarity. This is achieved easily by changing the criterion $\phi_1 + \phi_3 > \phi_2 + \phi_4$ to

$$\phi_1 + \phi_3 + \left|\pi - (V_4V_1\widehat{V_2, V_4}V_2V_3)\right| > \phi_2 + \phi_4 + \left|\pi - (V_1V_2\widehat{V_3, V_1}V_3V_4)\right| \tag{4.58}$$

where $(AB\widehat{C, D}EF)$ denotes the *dihedral angle* between the two planes defined by the triangles ABC and DEF respectively. When the dihedral angles are close to π, the criterion reduces to the original version. An extra consideration is that the new edge might already exist. In that case "flipping" might damage the topology of the mesh and should be avoided. See figure 4.7 for an example of the effects of Delaunay remeshing (algorithm 4) on a mesh.

Adaptive Relaxation

Unfortunately, remeshing is not enough to keep the condition of the mesh in check. We also need a way to redistribute the vertices along the free boundary, in order to achieve a local density of nodes compatible with the objective of minimizing $\mathrm{cond}(M)$. A crude way to do this is to essentially *diffuse* the vertices along the free boundary by repeatedly applying an operation of the form

$$\mathbf{x}_i^{(n+1)} = \mathbf{x}_i^{(n)} + h \sum_{\substack{V_j \in \mathcal{V} \\ \alpha_{ij} \neq 0}} \left(\mathbf{x}_j^{(n)} - \mathbf{x}_i^{(n)} \right) \tag{4.59}$$

with $h > 0$ sufficiently small.

An interpretation of (4.59) is to picture the mesh as a set of small masses (the vertices) connected by springs (the edges) with an extremely high damping constant. If the masses can move freely, the effect is identical to (4.59). This is why the operation (4.59) is called *relaxation*. The net effect is similar to an anisotropic diffusion of the vector field $\mathbf{x}$.

If the vertices are allowed to move in an unconstrained manner under the influence of (4.59), they tend to escape the free boundary. This effect can be countered easily, by removing the *normal component* of the sum:

$$\mathbf{x}_i^{(n+1)} = \mathbf{x}_i^{(n)} + h \left\{ \Delta\mathbf{x}_i - (\Delta\mathbf{x}_i \cdot \hat{\mathbf{n}}_i)\hat{\mathbf{n}}_i \right\} \tag{4.60}$$

where

$$\Delta\mathbf{x}_i = \sum_{\substack{V_j \in \mathcal{V} \\ \alpha_{ij} \neq 0}} \left(\mathbf{x}_j^{(n)} - \mathbf{x}_i^{(n)} \right) \tag{4.61}$$

Although relaxing the mesh using (4.60) does make it more uniform, it does not decrease $\mathrm{cond}(M)$. The problem is that the relaxation tends to move vertices from areas of high curvature (where the density of the nodes should be high) toward areas of lower curvature. The solution is to combine (4.60) with an appropriate *weighted Laplace operator* [Tho]:

$$\Delta\mathbf{x}_i = \sum_{\substack{V_j \in \mathcal{V} \\ \alpha_{ij} \neq 0}} w_{ij} \left(\mathbf{x}_j^{(n)} - \mathbf{x}_i^{(n)} \right) \tag{4.62}$$

where, using the same notation with (4.53),

$$w_{ij} = 1 - \frac{c_{cond}\rho_{ij}}{d_{ij}} \tag{4.63}$$

This particular choice of weights becomes obvious if we combine the interpretation of the relaxation in terms of springs with the fact that for $\mathrm{cond}(M)$ to be minimized, all the edges must have length approximately equal to $c_{cond}\rho_{ij}$. The immediate conclusion is that we should set the *rest length* of every edge-spring to be exactly $c_{cond}\rho_{ij}$, which is equivalent to defining the weights w_{ij} as above.

Algorithm 5 Adaptive Relaxation

```
Input: The initial mesh $M$ and an upper bound $C$ for $\mathrm{cond}(M)$.
repeat
    $h_{min} \leftarrow \infty$
    for all the vertices $V_i \in \mathcal{V}$ do
        Calculate $\Delta\mathbf{x}_i$ according to (4.62).
        $\Delta\mathbf{x}_i \leftarrow \Delta\mathbf{x}_i - (\Delta\mathbf{x}_i \cdot \hat{\mathbf{n}}_i)\hat{\mathbf{n}}_i$
        Calculate the minimum edge length $d_i$ and the local radius of curvature $\rho_i$.
        $h \leftarrow \min\{c\frac{d_i}{|\Delta\mathbf{x}_i|}, c'\rho_i\} \qquad (c, c' < 1)$
        if $h < h_{min}$ then $h_{min} \leftarrow h$
    for all the $V_i \in \mathcal{V}$ do
        $\mathbf{x}_i \leftarrow \mathbf{x}_i + h_{min}\Delta\mathbf{x}_i$
    (Optional) Perform Delaunay remeshing on $M$.
until $\mathrm{cond}(M) < C$
Output: The relaxed mesh $M'$.
```

The step size h in (4.60) can be determined by enforcing the stability condition

$$h < \min_{V_i \in \mathcal{V}} \frac{d_i}{|\Delta\mathbf{x}_i|} \tag{4.64}$$

where d_i is the length of the shortest edge of the vertex V_i (see eq.(4.39)). We have found in practice that h should also be smaller than a (fixed) fraction of the radius of curvature ρ at every vertex.

Selective Refinement

The adaptive relaxation can improve the distribution of the vertices along the free boundary, but it can not introduce new ones. Hence, if there are not enough vertices available, relaxing the

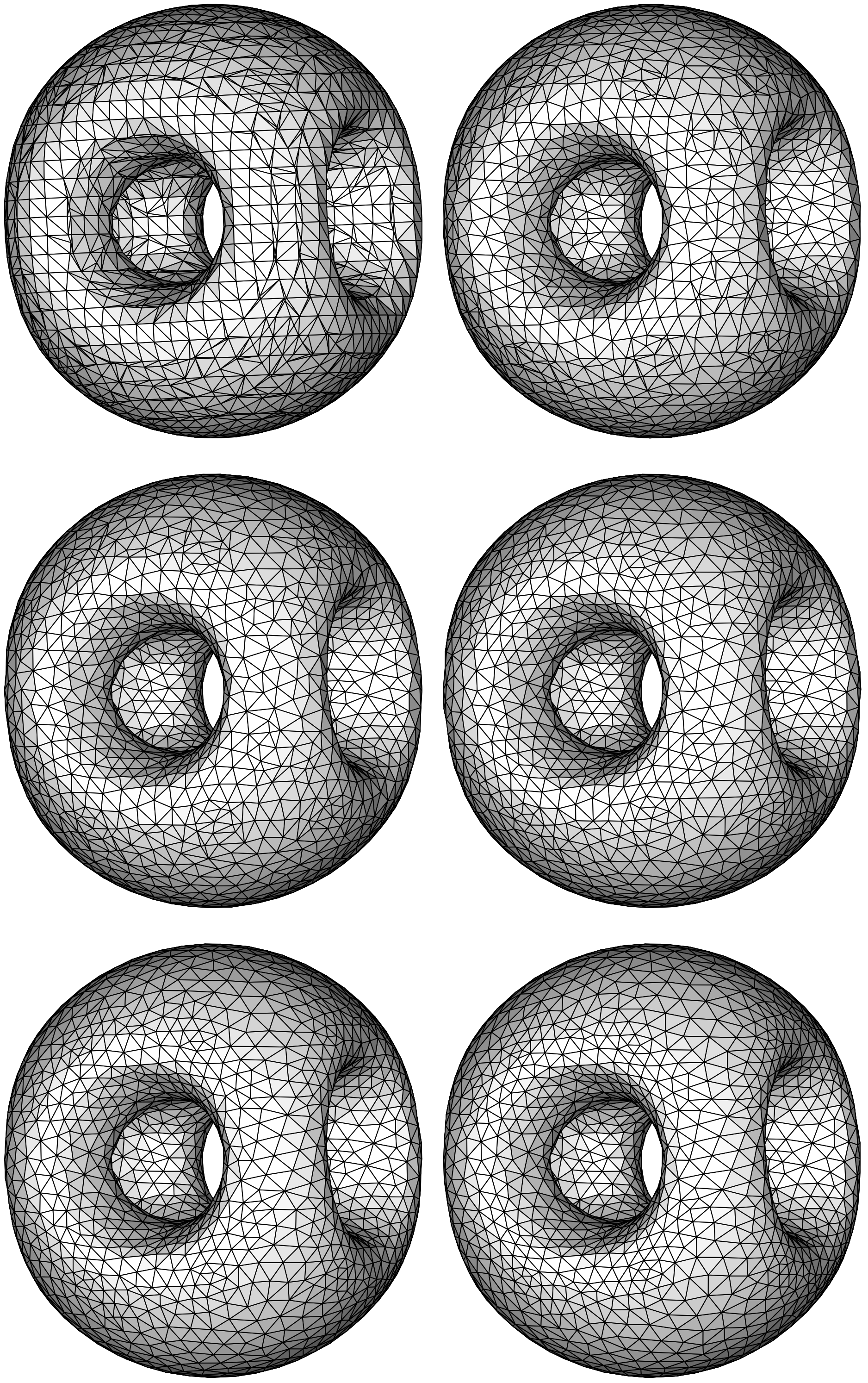

FIGURE 4.8. Example of adaptive relaxation. We started from the top left mesh ($\mathrm{cond}(M) = .74$) and allowed it to relax until we got the bottom right mesh ($\mathrm{cond}(M) = .41$). The effect of the relaxation is a more uniform distribution of the vertices along the surface.

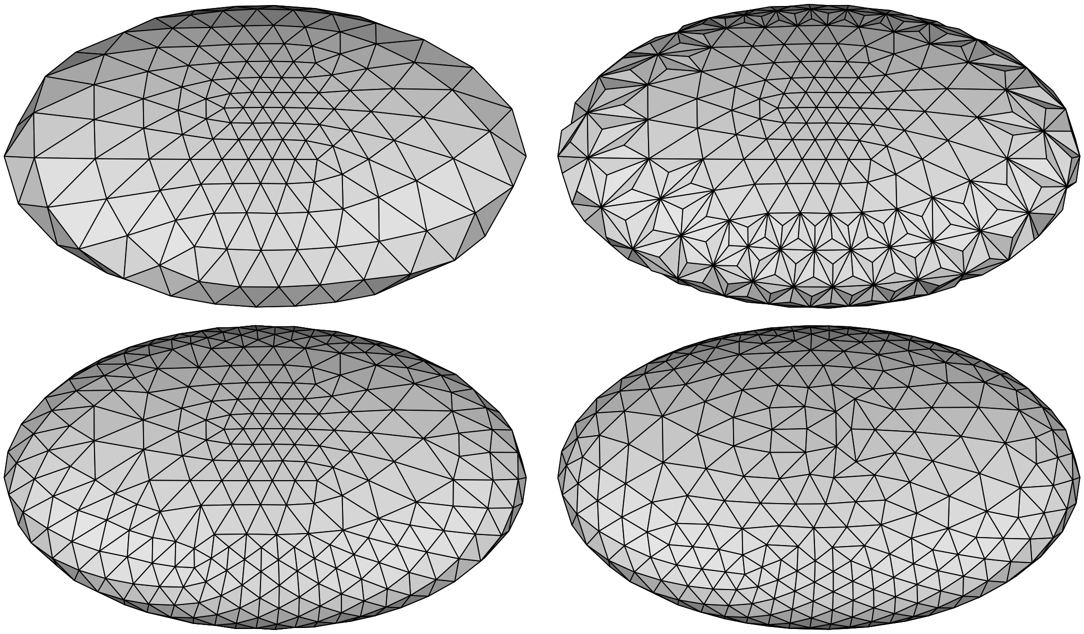

FIGURE 4.9. Example of Selective Refinement. We refine the mesh by adding extra vertices at areas of high curvature. The new vertices are the projection of the centers of existing faces on the surface (top right). After refining, we apply remeshing (bottom left) and relaxation (bottom right).

mesh will reduce $\mathrm{cond}(M)$ only up to a certain point. It is clear that we need a way to increase the number of vertices in the mesh, a process that is commonly called *mesh refinement*.

The basic idea is to locate faces that are, in a sense, too large and to subdivide them into a number of smaller faces, by adding the necessary number of new vertices. We subdivide a face $F_m \in \mathcal{F}$, when its area A_m *fails* the following criterion:

$$A_m \leq (c_{ref}\rho_m)^2 \frac{\sqrt{3}}{4} \tag{4.65}$$

where ρ_m is the average of the local radii of curvature at the three vertices of the face and $c_{ref} = 1.75c_{cond}$.

The right hand side is essentially the area of an equilateral triangle with side $c_{ref}\rho_m$. If an edge belongs to a face that fails the criterion, its length d_{ij} is approximately $c_{ref}\rho_m \approx 1.75c_{cond}\rho_{ij}$ and therefore it has a positive contribution to $\mathrm{cond}(M)$. By subdividing it appropriately, we can get a number of smaller faces whose edges are closer to the right length. Assuming that the new edges are roughly half as long as the old ones, we can justify the coefficient 1.75 in the definition of c_{ref} by noting that if we use a coefficient closer to 1, the new faces are going to be too small and $\mathrm{cond}(M)$ will not decline. Values larger than 2, on the other hand, increase the number of required subdivisions and are therefore not efficient.

Algorithm 6 Selective Refining

```
Input: The initial mesh $M$.
repeat
    for all the faces $F_m \in \mathcal{F}$ do
        Calculate the area $A_m$.
        Calculate the average $\rho_m$ of the local radii of curvature of the vertices.
        if $A_m \leq (c_{ref}\rho_m)^2 \frac{\sqrt{3}}{4}$ then
            Calculate the center of mass $\mathbf{c}$ of the face.
            for all the vertices $V_m^i \in \mathcal{V}_m$ of the face do
                Find the osculating paraboloid at $V_m^i$ using the iterative paraboloid fitting.
                Find the projection $\mathbf{c}_i$ of $\mathbf{c}$ on the paraboloid.
            Add a new vertex $V_{new}$ positioned at the average of the $\mathbf{c}_i$.
            Replace the face $F_m$ with the new faces $(V_{new}, V_m^2, V_m^3)$, $(V_m^1, V_{new}, V_m^3)$ and
            $(V_m^1, V_m^2, V_{new})$.
    Perform Delaunay remeshing on $M$.
    (Optional) Perform adaptive relaxation on $M$.
until no face were subdivided in tis iteration.
Output: The refined mesh $M'$.
```

The subdivision scheme that we use is straightforward (algorithm 6). First, we calculate the *center of mass* $\mathbf{c}$ of the face F_m that we want to subdivide:

$$\mathbf{c} = \frac{\mathbf{x}_m^1 + \mathbf{x}_m^2 + \mathbf{x}_m^3}{3} \tag{4.66}$$

Then we calculate the projections $\mathbf{c}_1, \mathbf{c}_2, \mathbf{c}_3$ of $\mathbf{c}$ on the osculating paraboloids of the three vertices of the face (see section 4.4) and use their average as the coordinates of the new vertex V_{new}.

Finally, we replace the face F_m with the three triangles that are formed when we join V_{new} with the three vertices of F_m. If we do this for all the faces that fail the criterion (4.65), we get something that looks like the top left mesh of figure 4.9, where several faces have been replaced by small pyramids.

It is clear that despite having more faces and vertices, the condition of the resulting mesh is probably worse than the original. It is only after remeshing using algorithm 4 that we arrive at an acceptable refined mesh (bottom left mesh of fig. 4.9). In practice, instead of just remeshing we perform a few iterations of the adaptive relaxation (algorithm 5), to make the transition between subdivided and non-subdivided regions of the mesh more smooth (bottom right mesh of fig. 4.9). The subdivision process is repeated until all the faces meet the criterion (4.65).

CHAPTER 5

VALIDATION

In this section, we check the validity of the numerical approximations by comparing the results for situations where the solution is known in advance. In the dynamical case, the only known solution is the linearized solution. As we show below, the numerical approximations yield results with very good accuracy.

5.1. Curvature and Surface Charge Density of an Ellipsoid

To check the accuracy of the numerical calculation of the mean curvature H and the surface charge density σ, we used the case of a droplet with the shape of an ellipsoid, for which exact expressions for H and σ are known. We calculated H and σ for an ellipsoid with semi axes 1,1 and 3 using meshes of various degrees of refinement. Some of them are shown in figure 5.1. In figures 5.2 and 5.3, we show a log-log plot of the relative numerical error versus the number of faces.

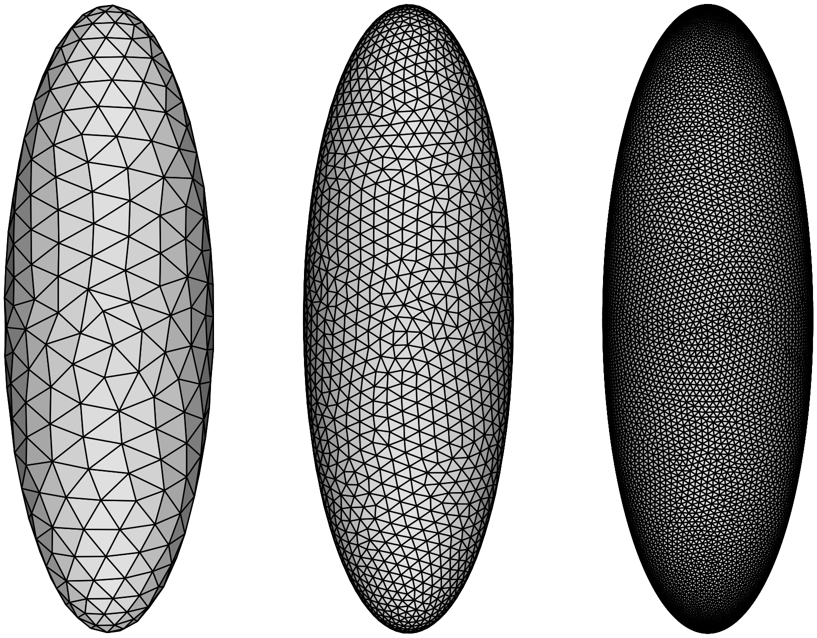

FIGURE 5.1. Meshes with 782, 3998 and 23604 faces that approximate the ellipsoid with dimensions 1,1 and 3.

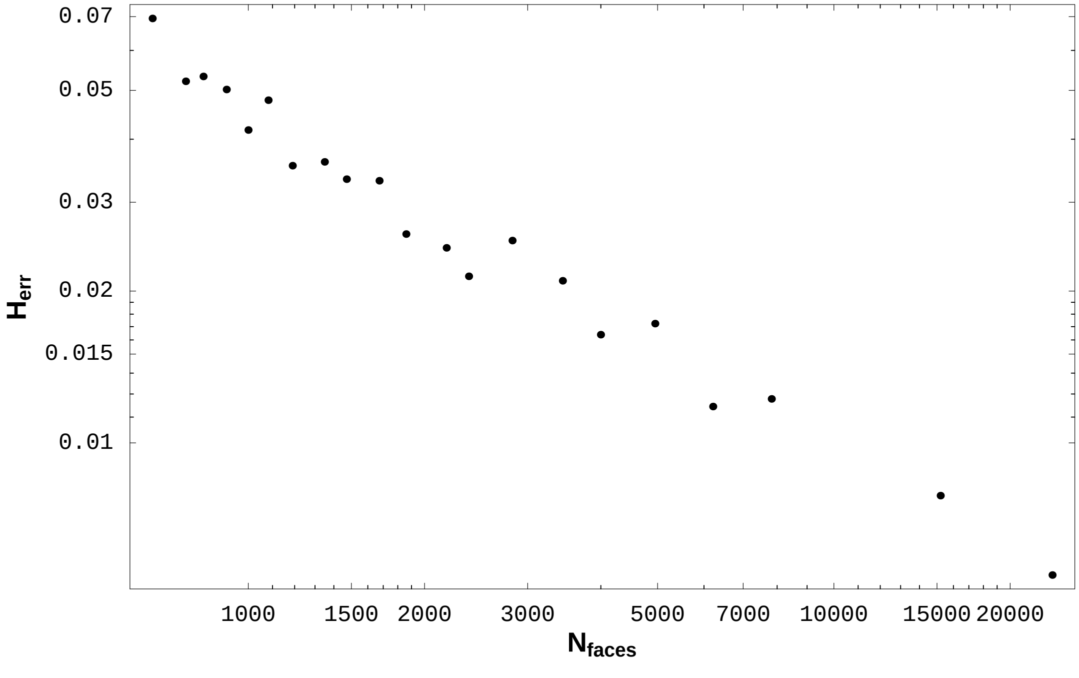

FIGURE 5.2. Log-log plot of the relative numerical error of the mean curvature H versus the number of faces.

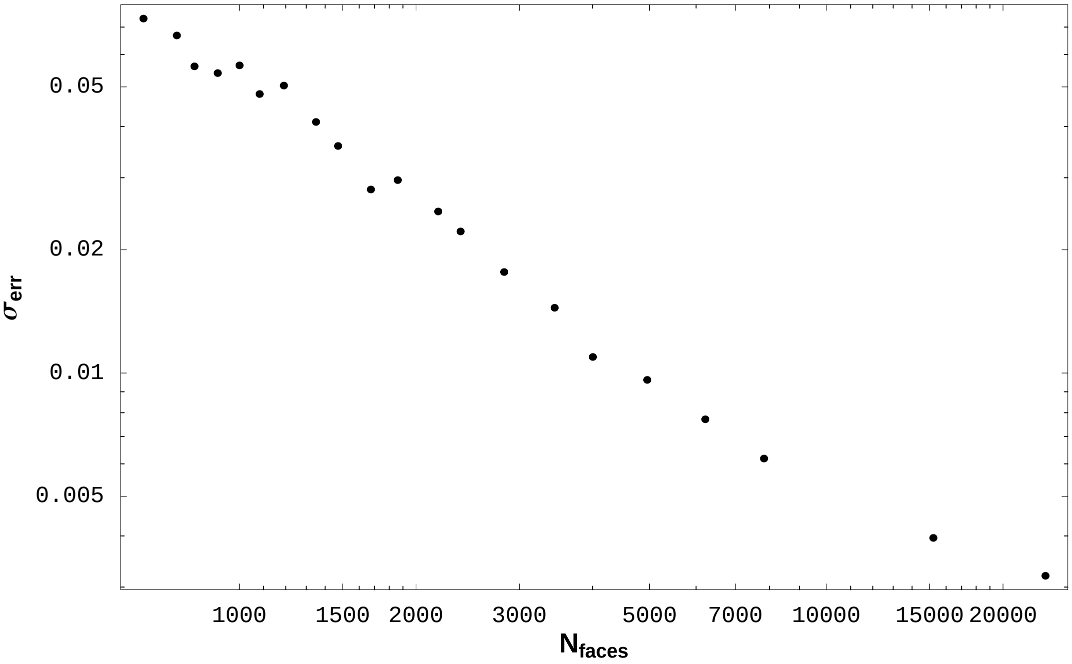

FIGURE 5.3. Log-log plot of the relative numerical error of the surface charge density σ versus the number of faces.

5.2. Comparison with the Linearized Solutions

The $\mathcal{Y}_2^0$ mode: Axisymmetric Case

We have calculated numerically the evolution of a sphere perturbed with the $\mathcal{Y}_2^0$ mode for $\epsilon = 0.02$ for subcritical $Q = \frac{1}{2}Q_{cr}$ and supercritical $Q = 2Q_{cr}$ values of the charge. We compared with the corresponding linearized solution (see sections 3.3 and 3.4) and verified that the error is of the order $\mathrm{O}(\epsilon^2)$ (for small enough t) as expected.

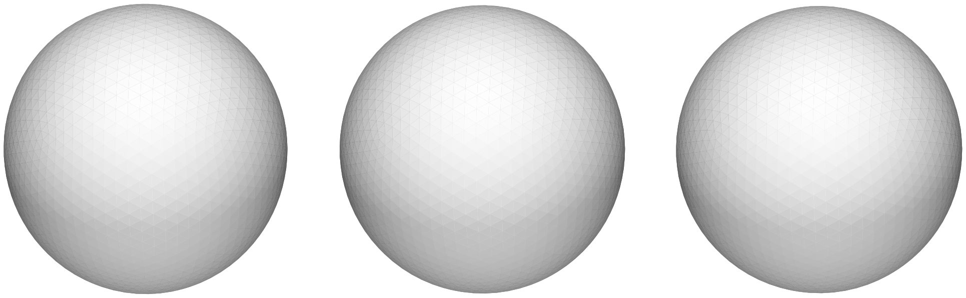

FIGURE 5.4. *Subcritical case* $(Q = \frac{1}{2}Q_{cr})$. The droplet for $t = 0$, $t = 2.5\tau$ and $t = 5\tau$.

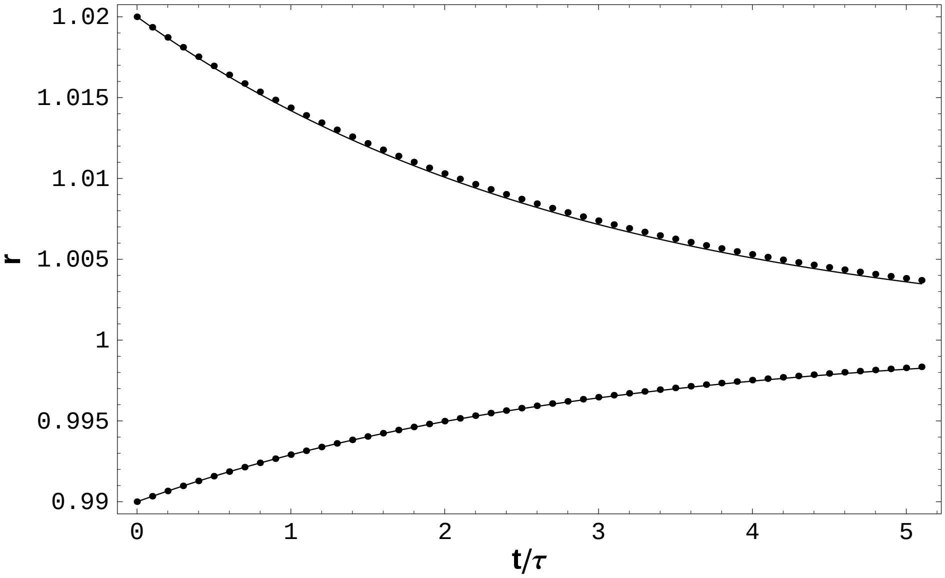

FIGURE 5.5. *Subcritical case* $(Q = \frac{1}{2}Q_{cr})$. Plot of the minimum and maximum radii r of the droplet versus (dimensionless) time . Both radii converge to the radius of the unperturbed sphere R. The numerical data are represented by dots and the linearized solution with a solid line.

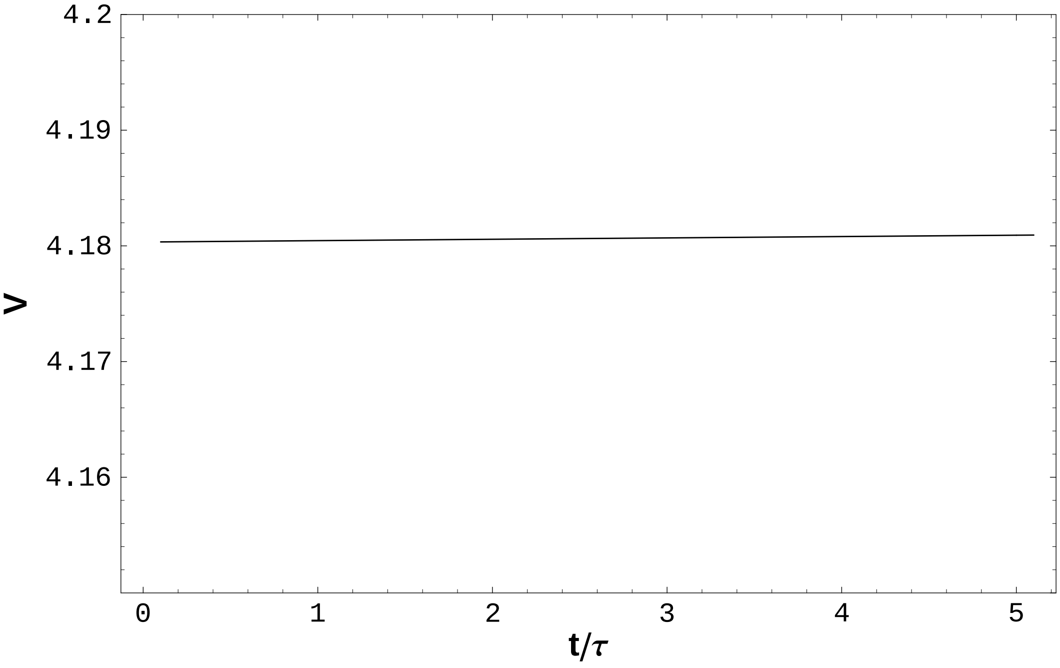

FIGURE 5.6. *Subcritical case* $(Q = \frac{1}{2}Q_{cr})$. Plot of the volume V of the droplet versus (dimensionless) time. The volume is conserved, as expected.

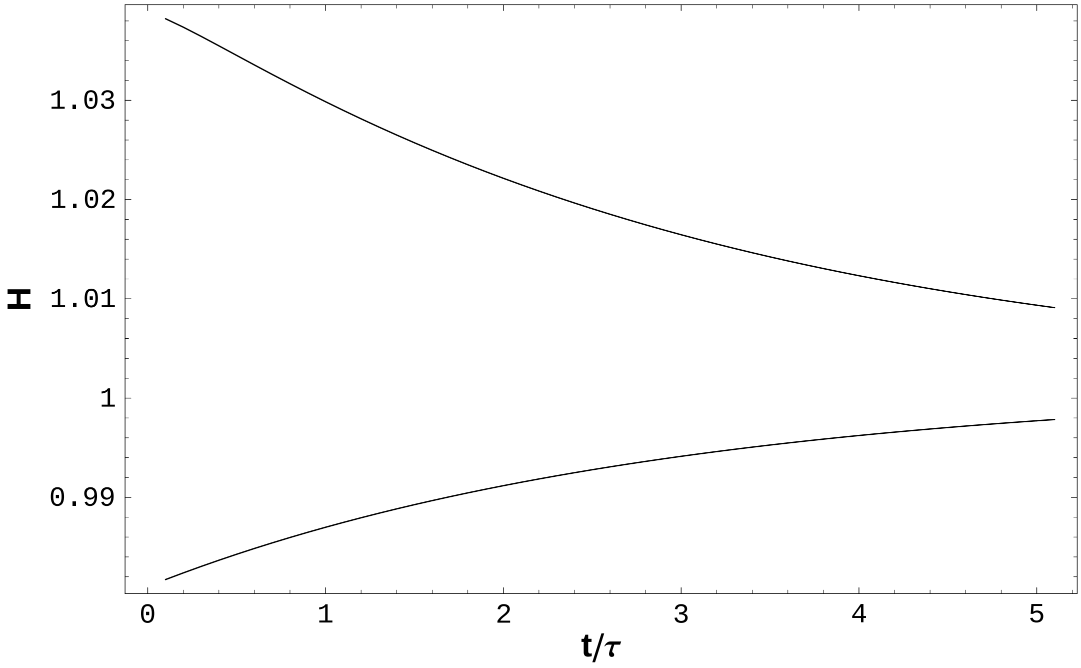

FIGURE 5.7. *Subcritical case* $(Q = \frac{1}{2}Q_{cr})$. Plot of the minimum and maximum mean curvature H of the droplet versus (dimensionless) time. Both curvatures converge to 1, the curvature of the unperturbed sphere R.

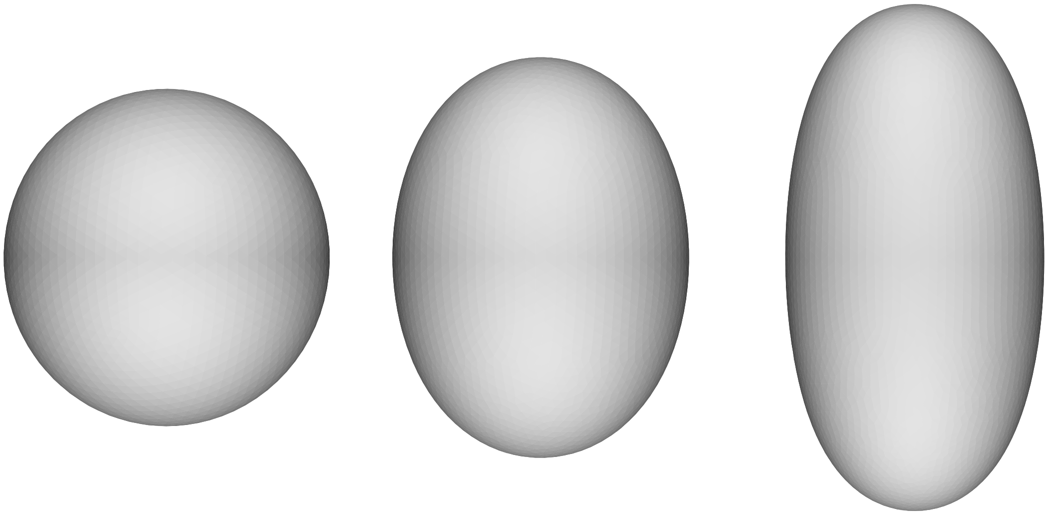

FIGURE 5.8. *Supercritical case* $(Q = 2Q_{cr})$. The droplet for $t = 0$, $t = 1.75\tau$ and $t = 2.5\tau$.

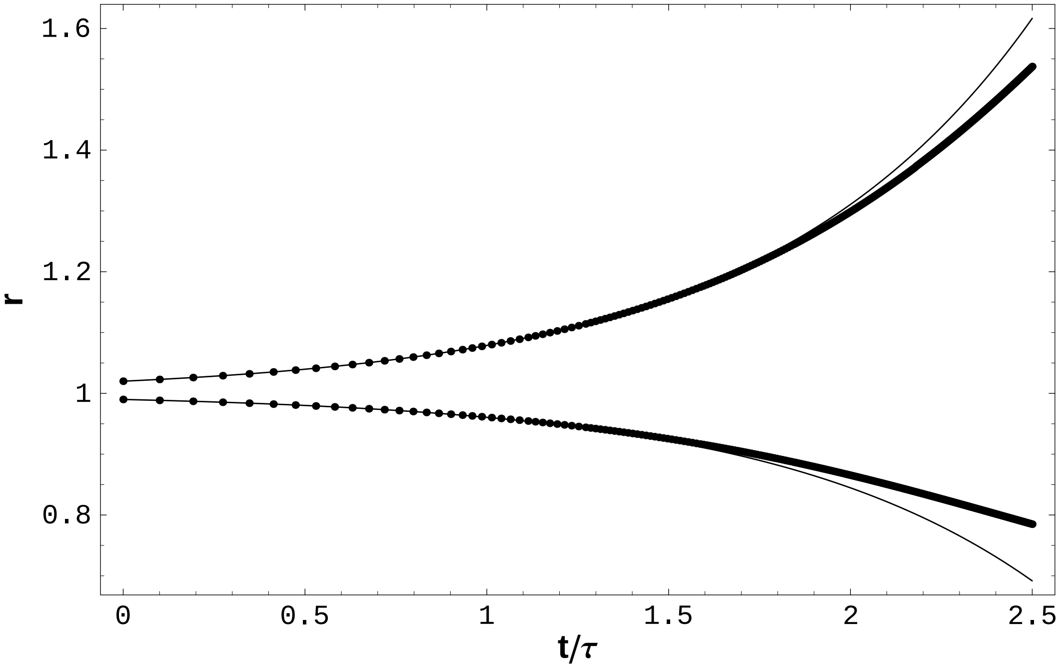

FIGURE 5.9. *Supercritical case* ($Q = 2Q_{cr}$). Plot of the minimum and maximum radius r of the droplet versus (dimensionless) time. The linearized and the numerical solutions agree in the region where the perturbation is small. For larger t, the non-linear regime dominates, and the lines diverge as expected.

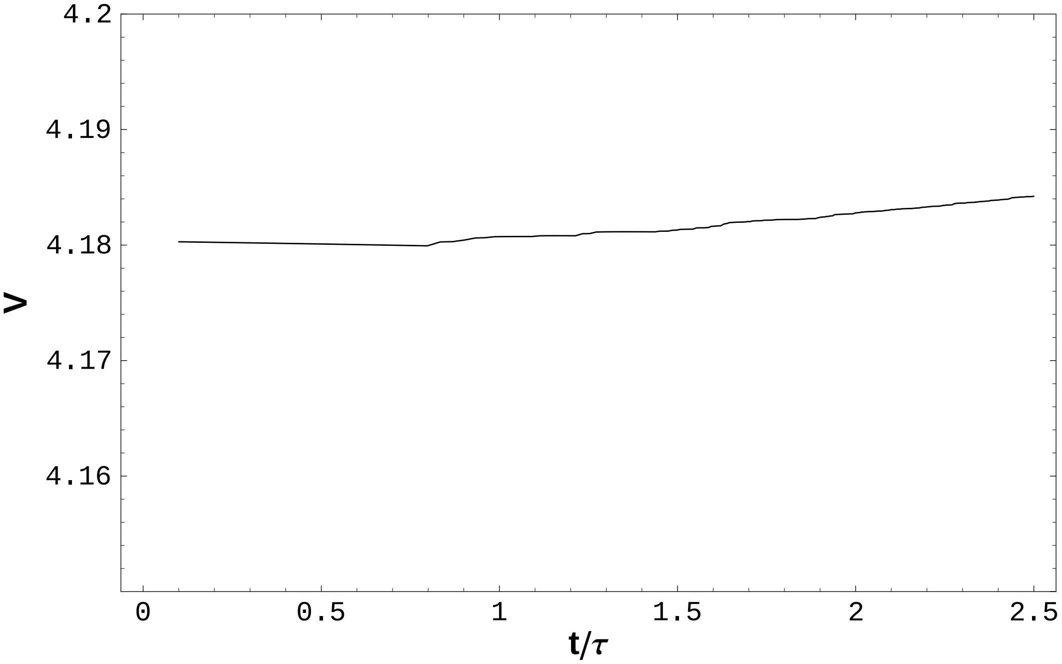

FIGURE 5.10. *Supercritical case* ($Q = 2Q_{cr}$). Plot of the volume V of the droplet versus (dimensionless) time. The volume is conserved within $.1\%$.

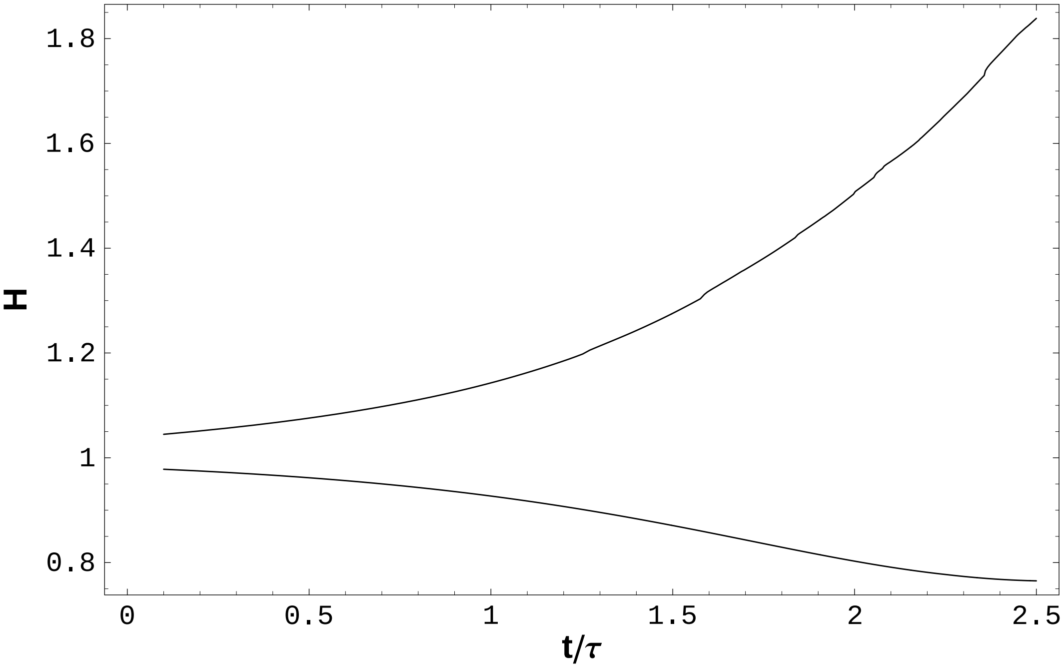

FIGURE 5.11. *Supercritical case* $(Q = 2Q_{cr})$. Plot of the minimum and maximum mean curvature H of the droplet versus (dimensionless) time.

The $\mathcal{Y}_3^2$ mode: Tetrahedral Symmetry

We have calculated numerically the evolution of a sphere perturbed with the $\mathcal{Y}_3^2$ mode for $\epsilon \approx 0.006$ for subcritical $Q = \frac{1}{2}Q_{cr}$ and supercritical $Q = 2Q_{cr}$ values of the charge. We compared with the corresponding linearized solution (see sections 3.3 and 3.4) and verified that the error is of the order $\mathrm{O}(\epsilon^2)$ (for small enough t) as expected.

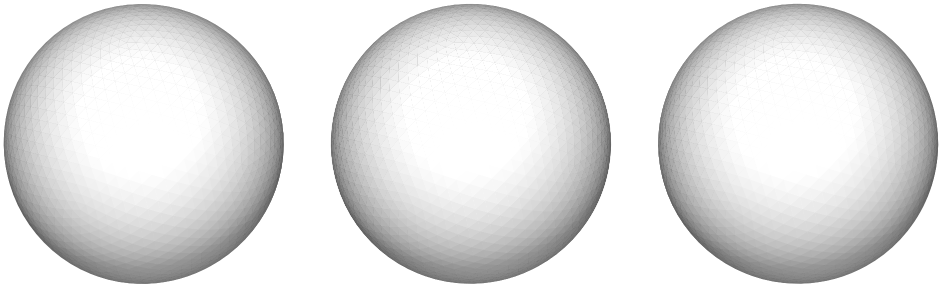

FIGURE 5.12. *Subcritical case* ($Q = \frac{1}{2}Q_{cr}$). The droplet for $t = 0$, $t = 2.5\tau$ and $t = 5\tau$.

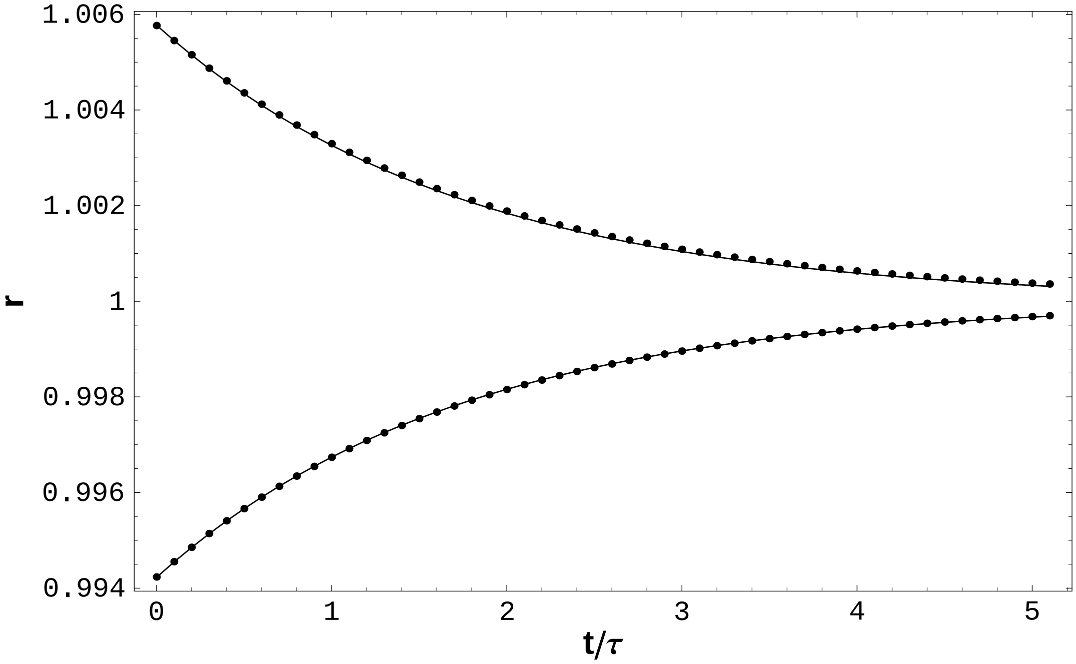

FIGURE 5.13. *Subcritical case* ($Q = \frac{1}{2}Q_{cr}$). Plot of the minimum and maximum radius r of the droplet versus (dimensionless) time. Both radii converge to the radius of the unperturbed sphere R.

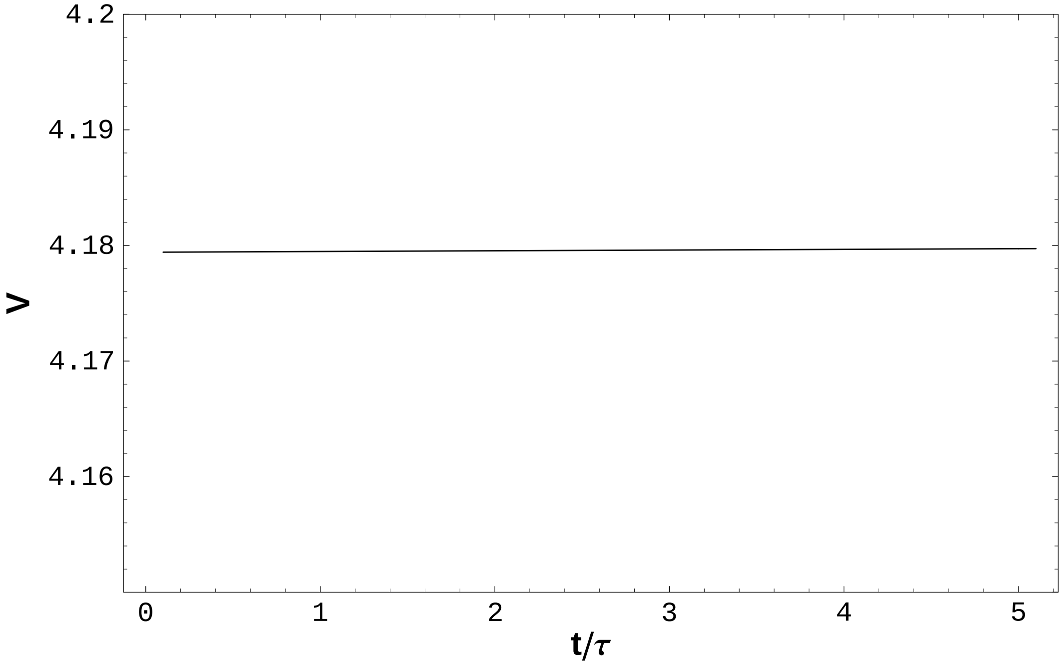

FIGURE 5.14. *Subcritical case* ($Q = \frac{1}{2}Q_{cr}$). Plot of the volume V of the droplet versus (dimensionless) time. The volume should be conserved.

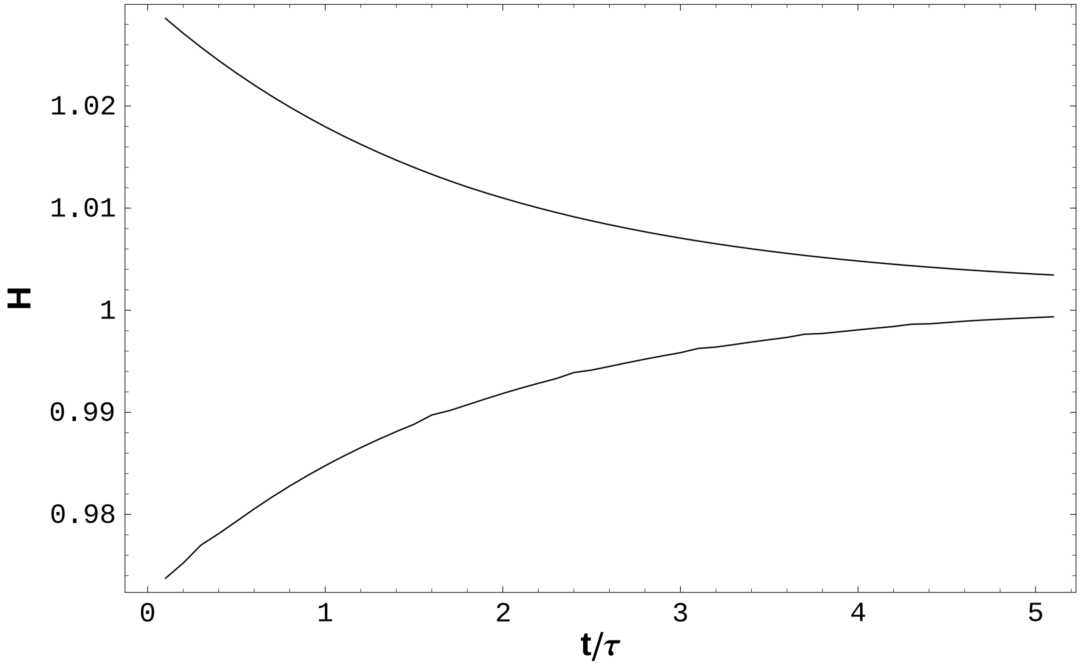

FIGURE 5.15. *Subcritical case* ($Q = \frac{1}{2}Q_{cr}$). Plot of the minimum and maximum mean curvature H of the droplet versus (dimensionless) time. Both curvatures converge to 1, the curvature of the unperturbed sphere R.

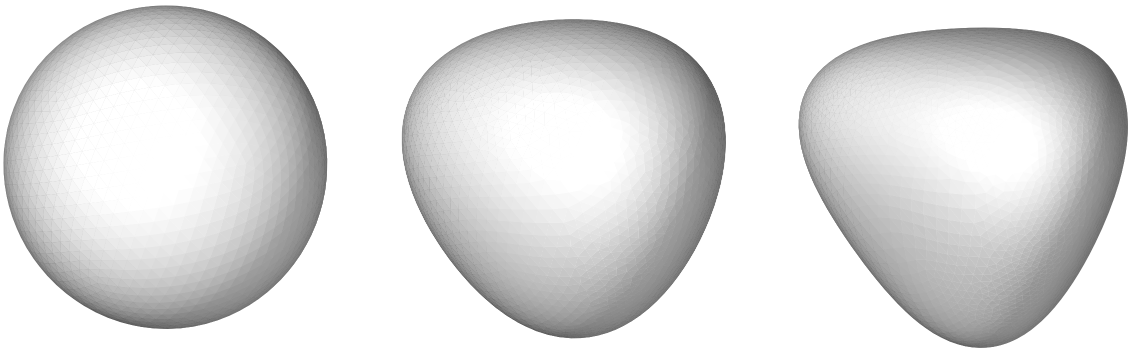

FIGURE 5.16. *Supercritical case* $(Q = 2Q_{cr})$. The droplet for $t = 0$, $t = 1.25\tau$ and $t = 1.75\tau$.

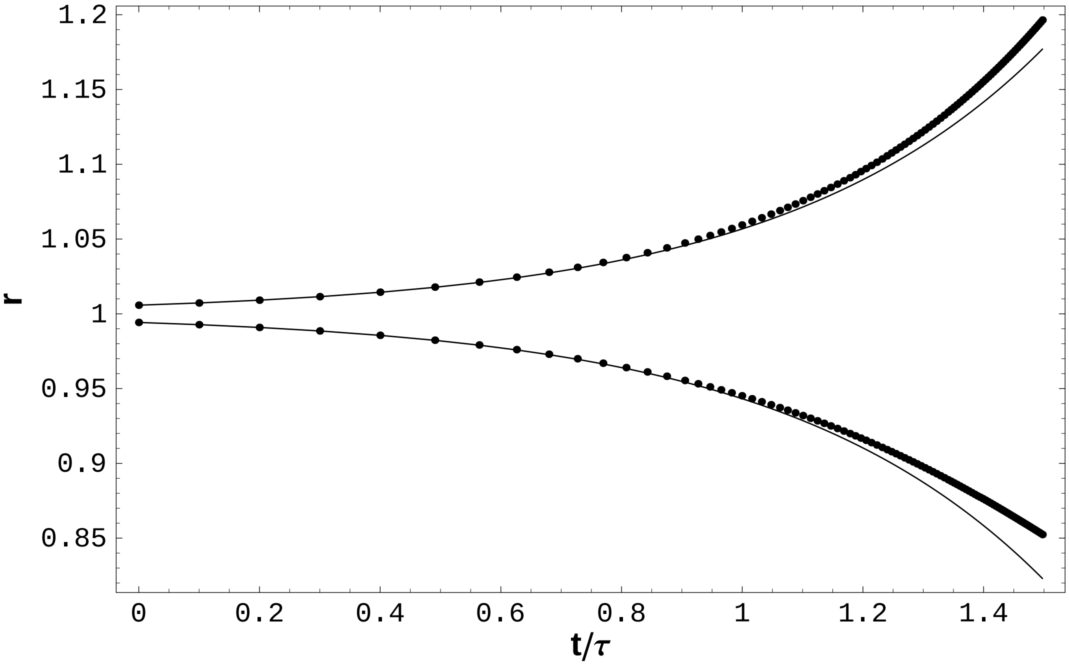

FIGURE 5.17. *Supercritical case* $(Q = 2Q_{cr})$. Plot of the minimum and maximum radius r of the droplet versus (dimensionless) time. The linearized and the numerical solutions agree in the region where the perturbation is small. For larger t, the non-linear regime dominates.

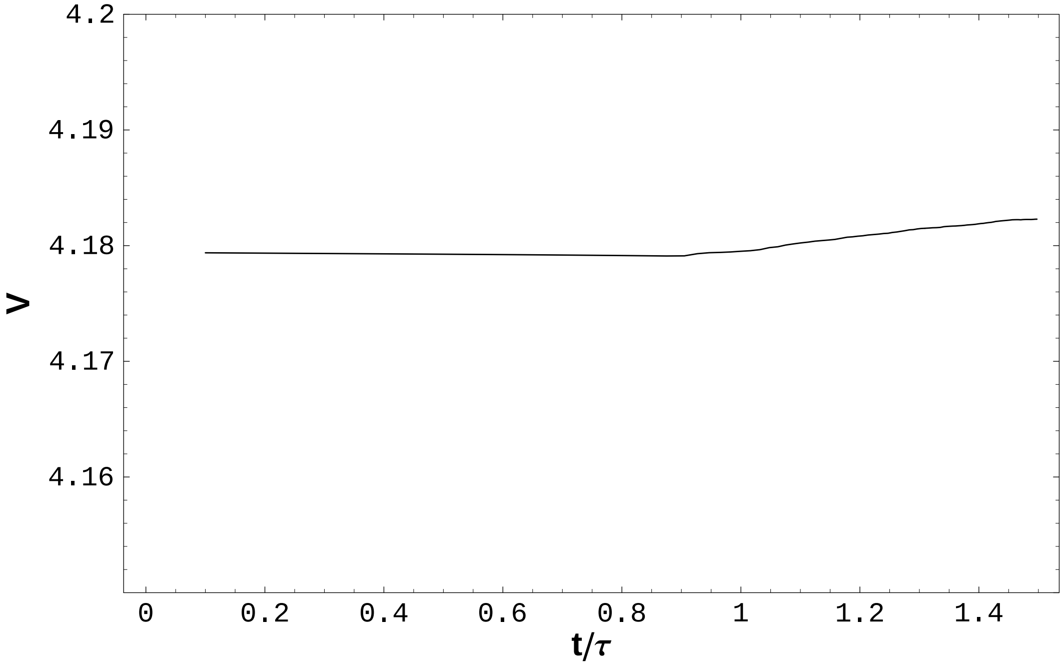

FIGURE 5.18. *Supercritical case* $(Q = 2Q_{cr})$. Plot of the volume V of the droplet versus (dimensionless) time. The volume should be conserved.

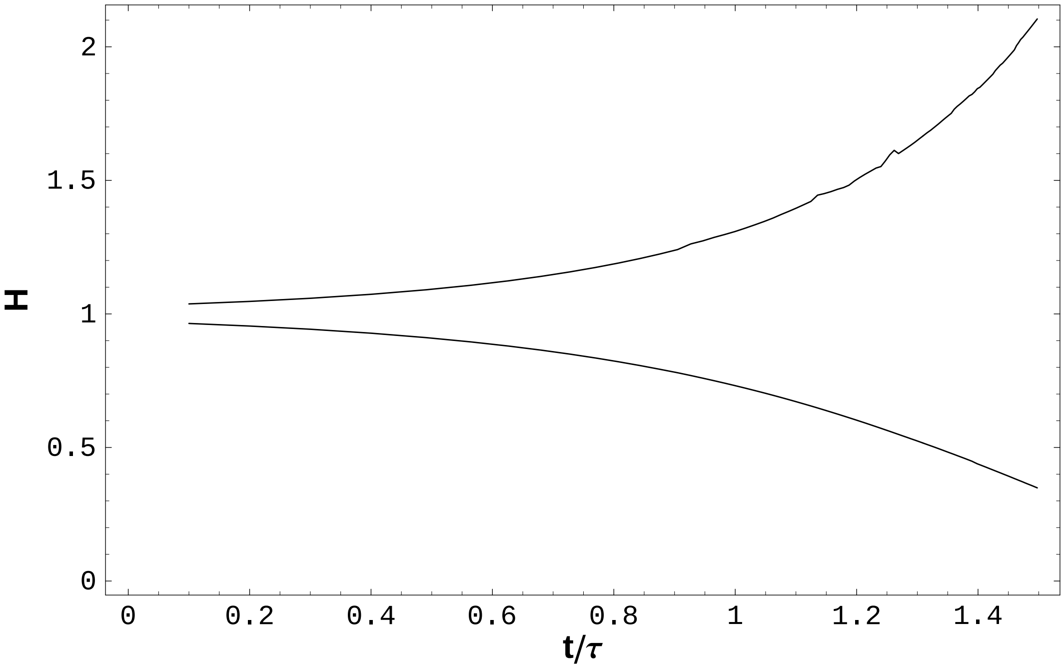

FIGURE 5.19. *Supercritical case* $(Q = 2Q_{cr})$. Plot of the minimum and maximum mean curvature H of the droplet versus (dimensionless) time.

The $\lambda\mathcal{Y}_4^0 + \mathcal{Y}_4^3$ mode: Cubic Symmetry

We have calculated numerically the evolution of a sphere perturbed with the $\lambda\mathcal{Y}_4^0 + \mathcal{Y}_4^3$, $\lambda = \sqrt{\frac{7}{40}}$, mode for $\epsilon \approx 0.022$ for subcritical $Q = \frac{1}{2}Q_{cr}$ and supercritical $Q = 2Q_{cr}$ values of the charge. We compared with the corresponding linearized solution (see sections 3.3 and 3.4) and verified that the error is of the order $\mathrm{O}(\epsilon^2)$ (for small enough t) as expected.

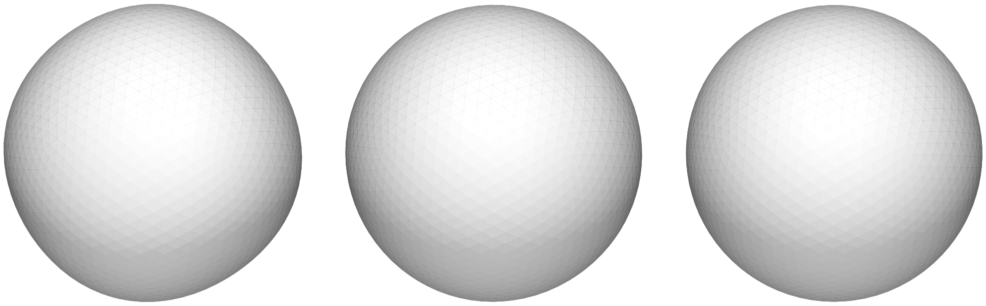

FIGURE 5.20. *Subcritical case* ($Q = \frac{1}{2}Q_{cr}$). The droplet for $t = 0$, $t = 2.5\tau$ and $t = 5\tau$.

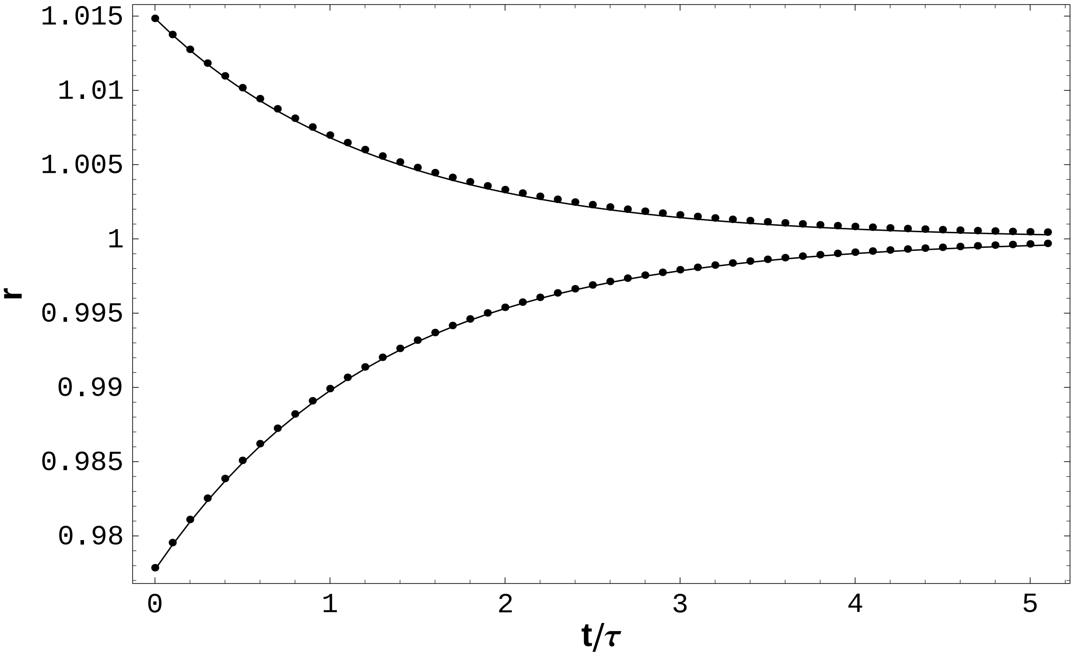

FIGURE 5.21. *Subcritical case* ($Q = \frac{1}{2}Q_{cr}$). Plot of the minimum and maximum radius r of the droplet versus (dimensionless) time. Both radii converge to the radius of the unperturbed sphere R.

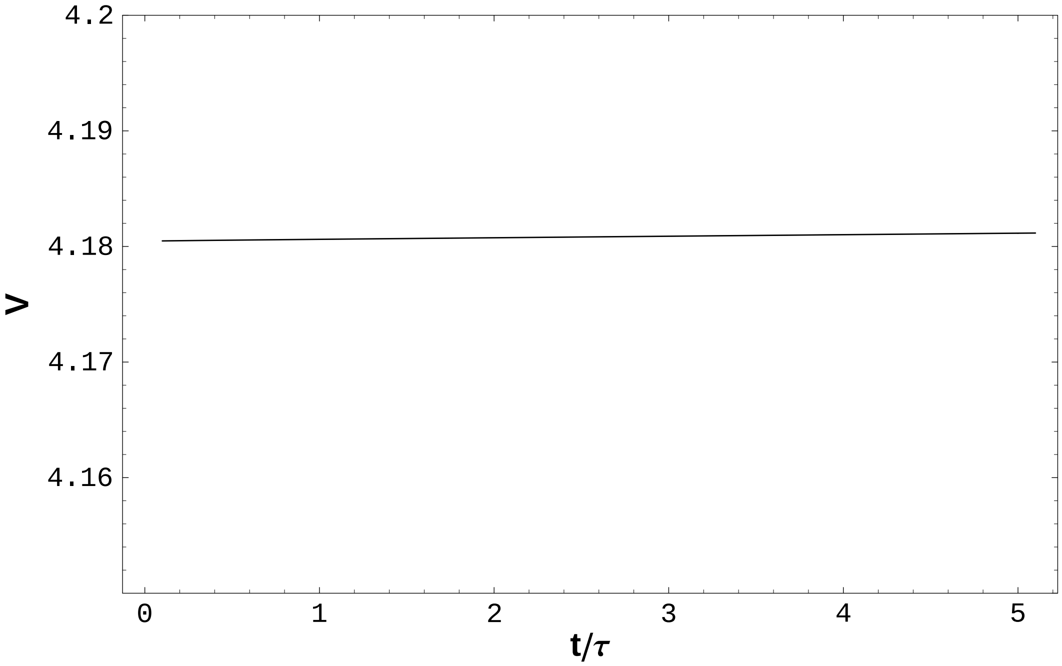

FIGURE 5.22. *Subcritical case* ($Q = \frac{1}{2}Q_{cr}$). Plot of the volume V of the droplet versus (dimensionless) time . The volume should be conserved.

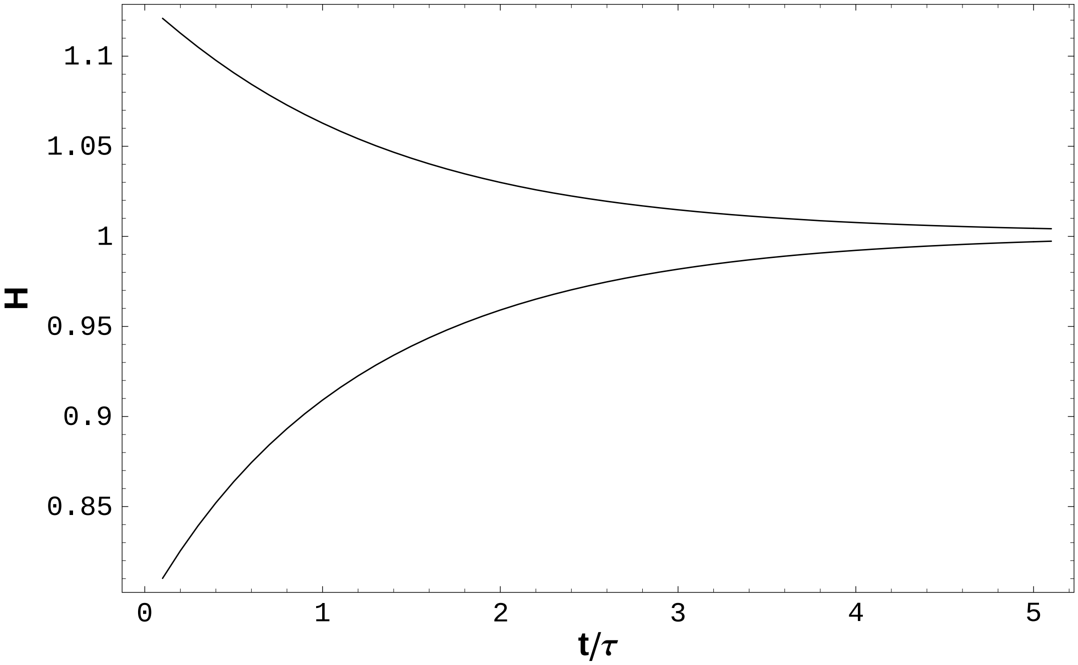

FIGURE 5.23. *Subcritical case* ($Q = \frac{1}{2}Q_{cr}$). Plot of the minimum and maximum mean curvature H of the droplet versus (dimensionless) time . Both curvatures converge to 1, the curvature of the unperturbed sphere R.

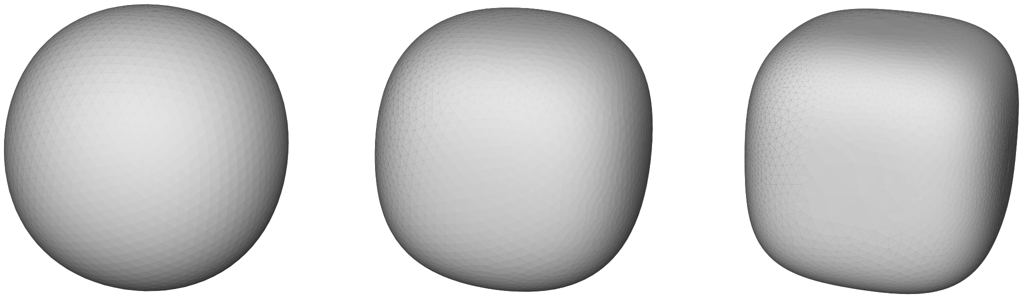

FIGURE 5.24. *Supercritical case* ($Q = 2Q_{cr}$). The droplet for $t = 0$, $t = 0.4\tau$ and $t = 0.6\tau$.

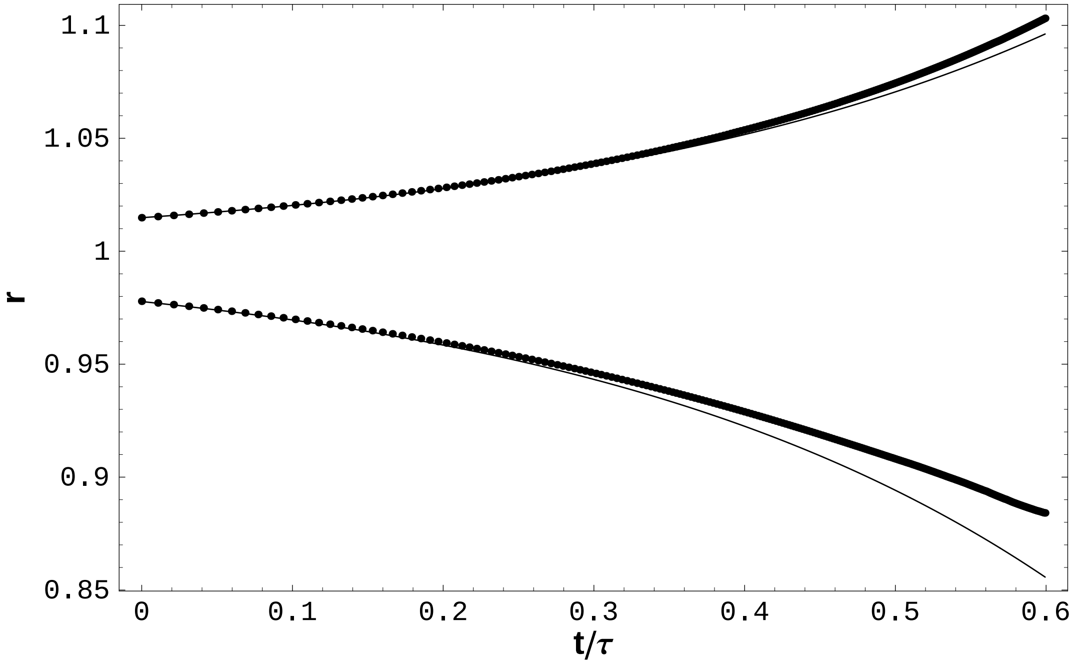

FIGURE 5.25. *Supercritical case* ($Q = 2Q_{cr}$). Plot of the minimum and maximum radius r of the droplet versus (dimensionless) time . The linearized and the numerical solutions agree in the region where the perturbation is small. For larger t, the non-linear regime dominates.

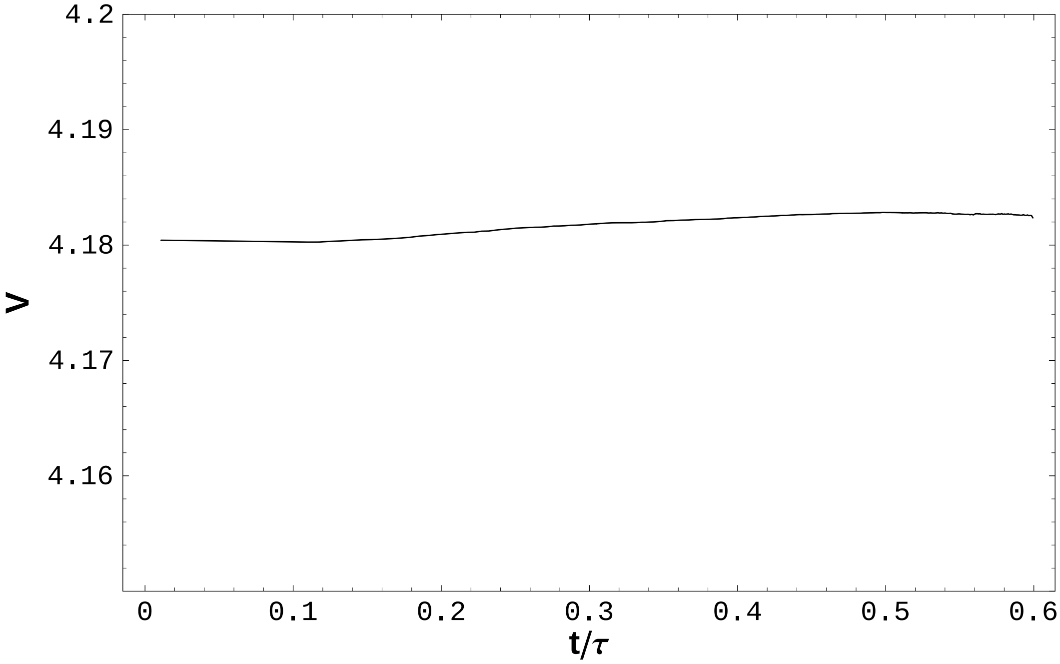

FIGURE 5.26. *Supercritical case* $(Q = 2Q_{cr})$. Plot of the volume V of the droplet versus (dimensionless) time . The volume should be conserved.

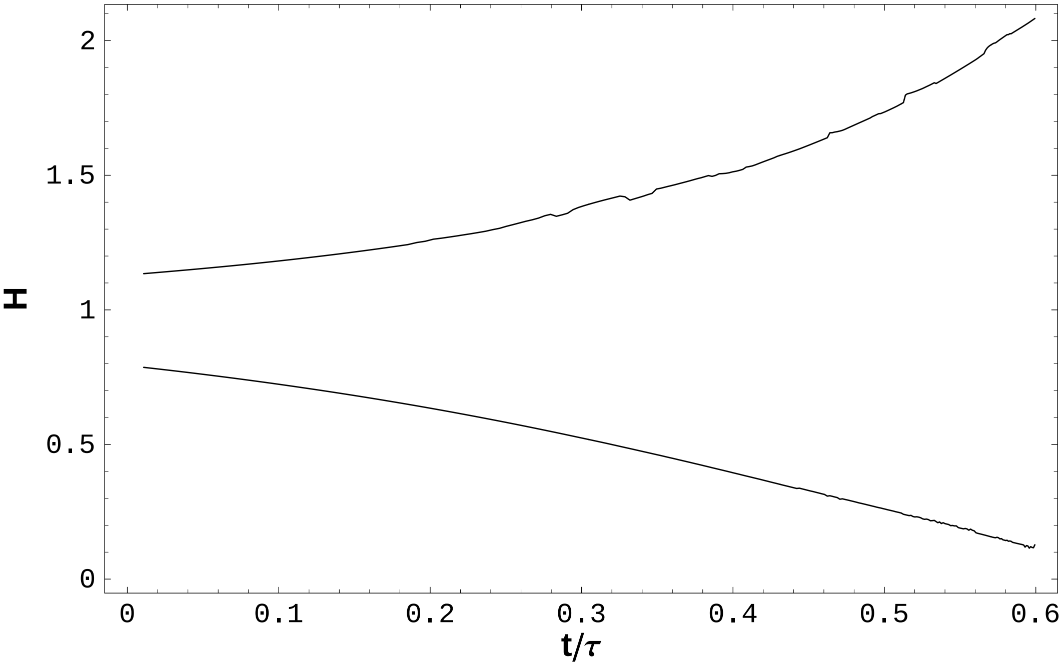

FIGURE 5.27. *Supercritical case* $(Q = 2Q_{cr})$. Plot of the minimum and maximum mean curvature H of the droplet versus (dimensionless) time .

CHAPTER 6

NUMERICAL RESULTS

Now that we have validated the code, we can study more interesting situations. Below we show results for:

- Neck elongation
- Hole closing in a multiply connected droplet
- Corner formation
- Instability of oblate spheroids

6.1. Neck Thinning

We evolve a sphere perturbed with the $\mathcal{Y}_2^0$ mode for $\epsilon = .4$ and supercritical charge $Q = 2Q_{cr}$. The bulk of the mass of the droplet is separated into two parts moving in opposite directions, connected by a thinning neck.

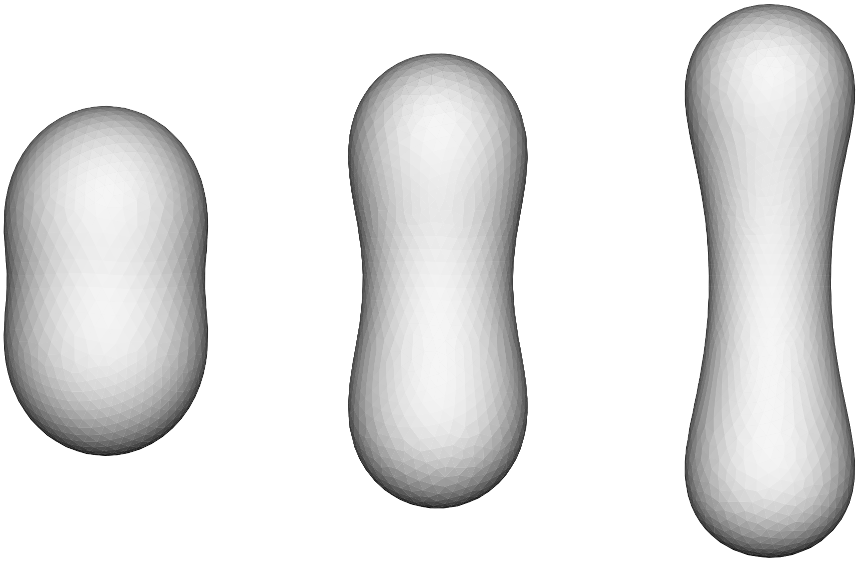

FIGURE 6.1. Evolution of a droplet forming a neck. The frames are for $t = 0., 1.1\tau, 2.07\tau$.

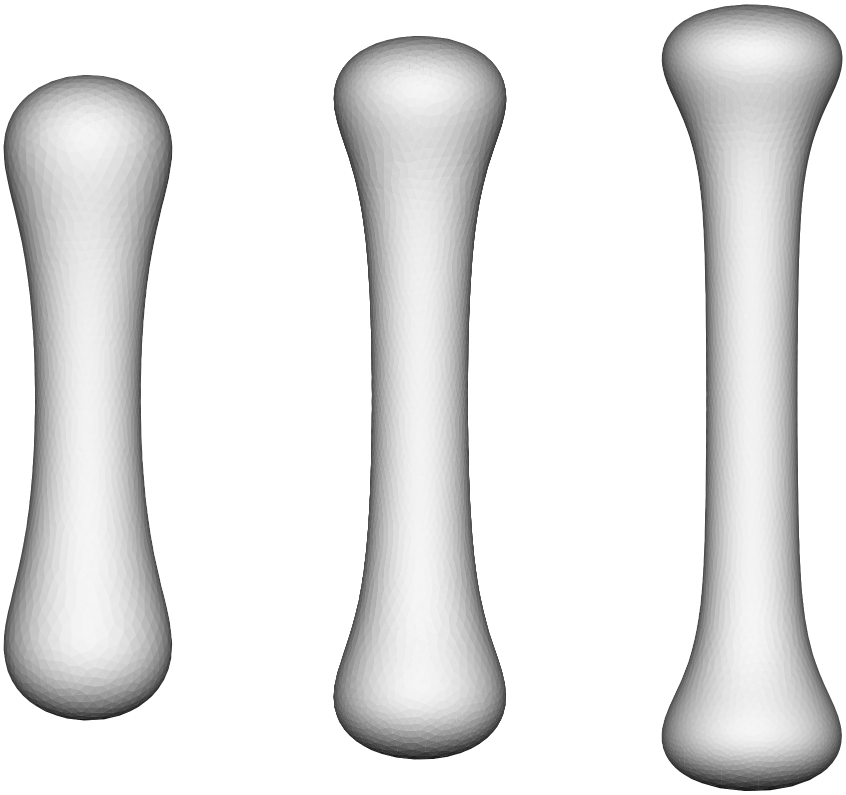

FIGURE 6.2. (contd.) Evolution of a droplet forming a neck. The frames are for $t = 3.14\tau, 4.25\tau, 5.3\tau$.

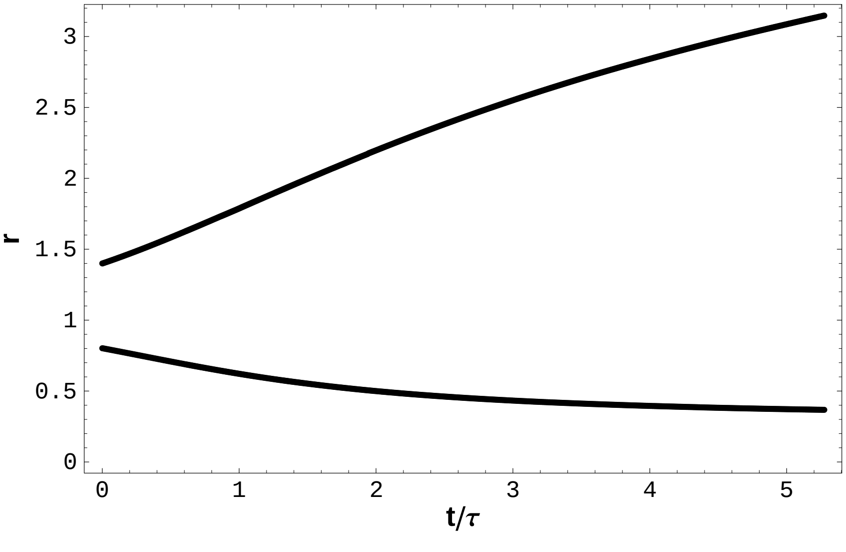

FIGURE 6.3. The radius of the neck and the length of the semi-major axis of the droplet as a function of time (divided by τ).

6.2. Evolution of a multiply connected droplet.

We evolve a multiply connected droplet with two holes running through it, one parallel to the x axis and the other parallel to the y axis. The charge is subcritical ($Q = .9Q_{cr}$). The holes shrink, tending to separate the "chamber" inside the droplet from the exterior surface.

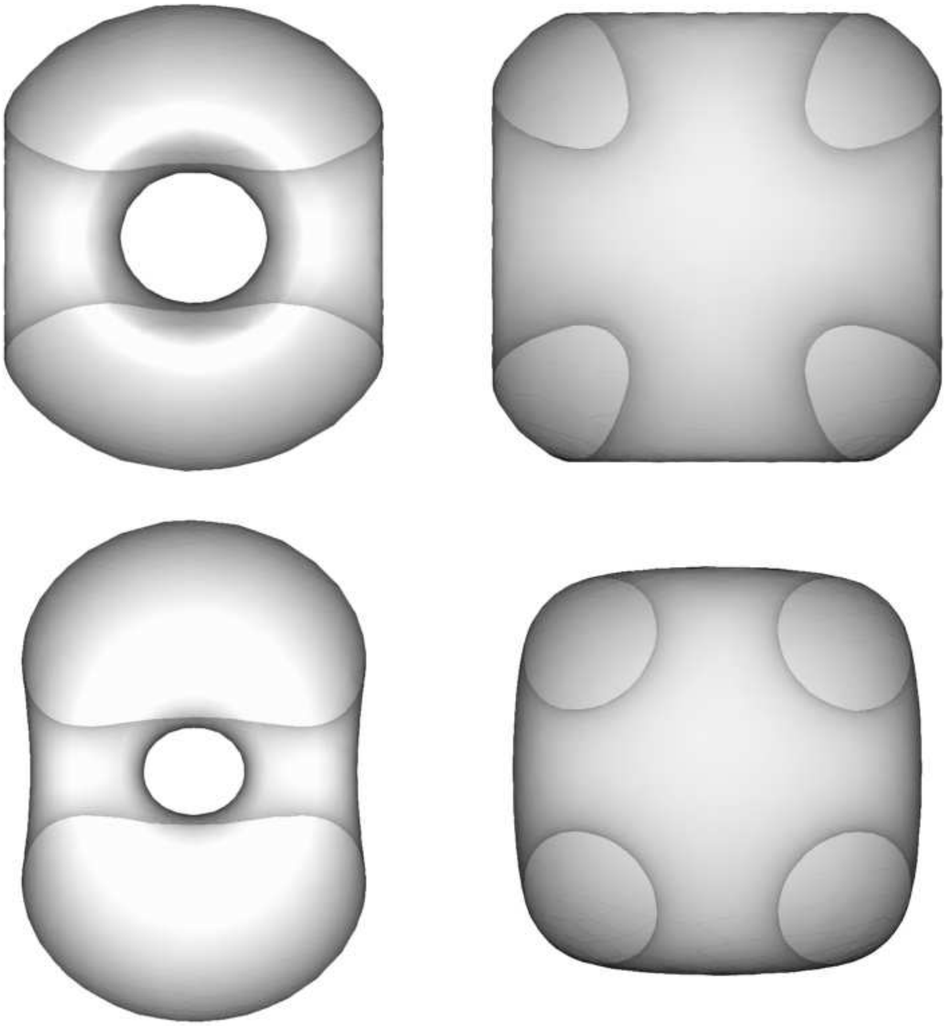

FIGURE 6.4. A multiply connected droplet ($t = 0, 26.4\tau$). Views from the z and y directions. The surface is semitransparent to allow an unobstructed view of the interior.

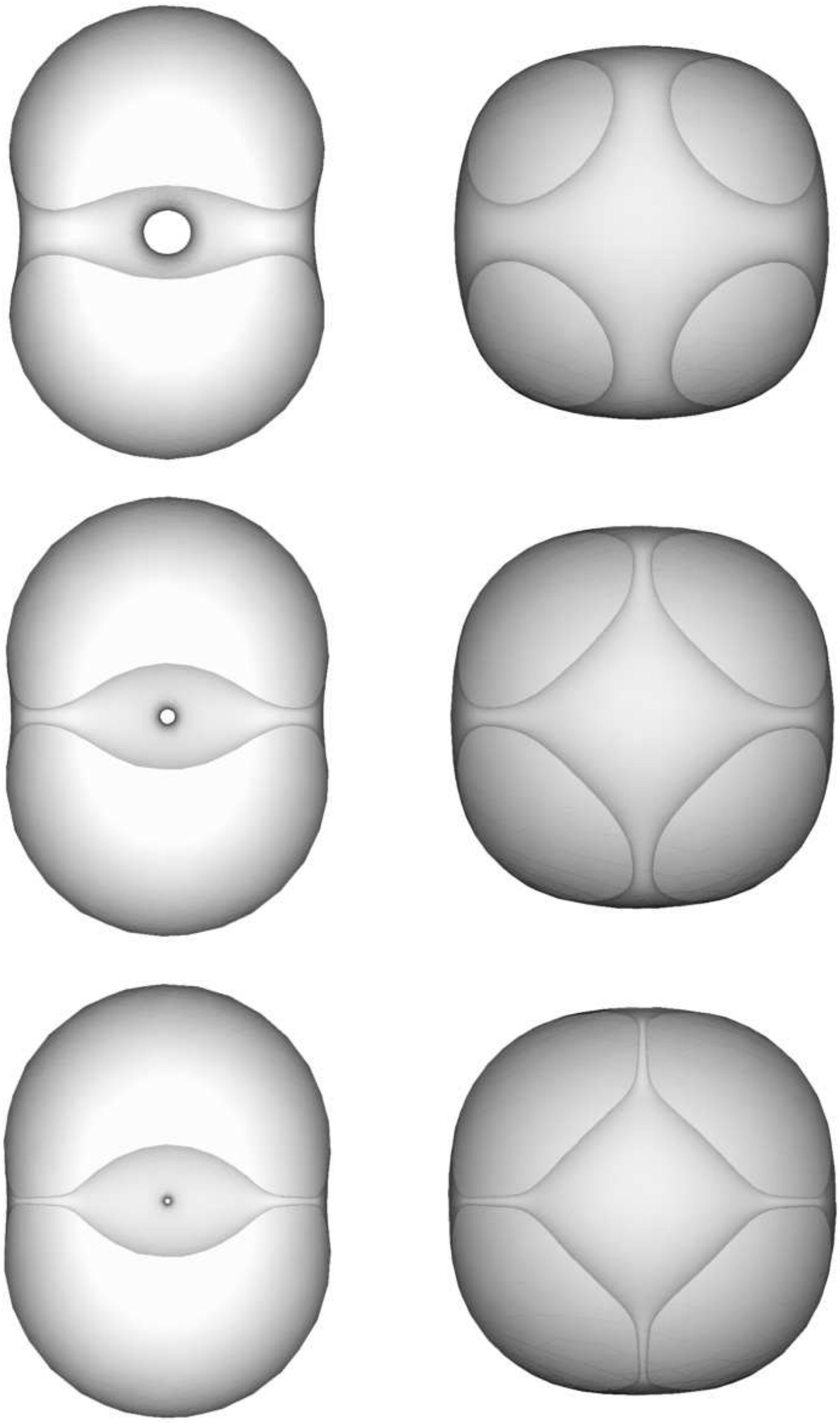

FIGURE 6.5. (contd.) A multiply connected droplet ($t = 56.4\tau, 75.5\tau, 81.5\tau$). Views from the z and y directions. The surface is semitransparent to allow an unobstructed view of the interior.

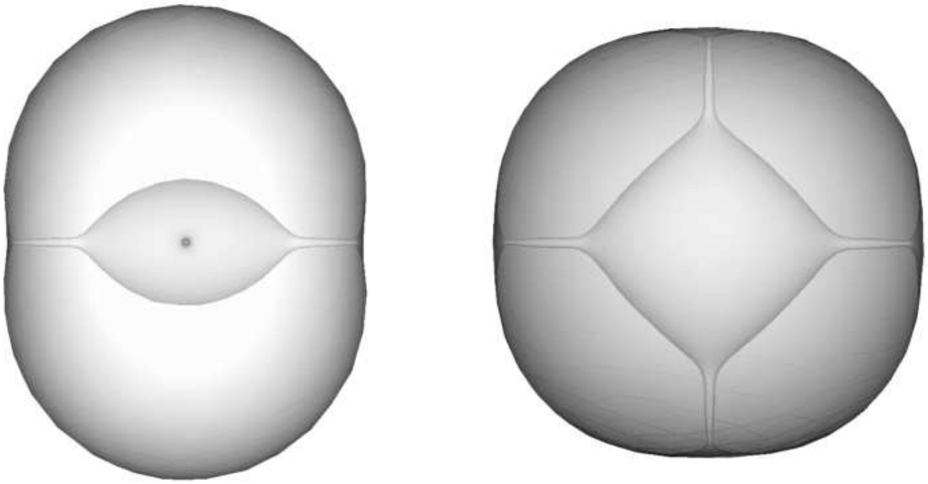

FIGURE 6.6. (contd.) A multiply connected droplet ($t = 83.8\tau$). Views from the z and y directions. The surface is semitransparent to allow an unobstructed view of the interior.

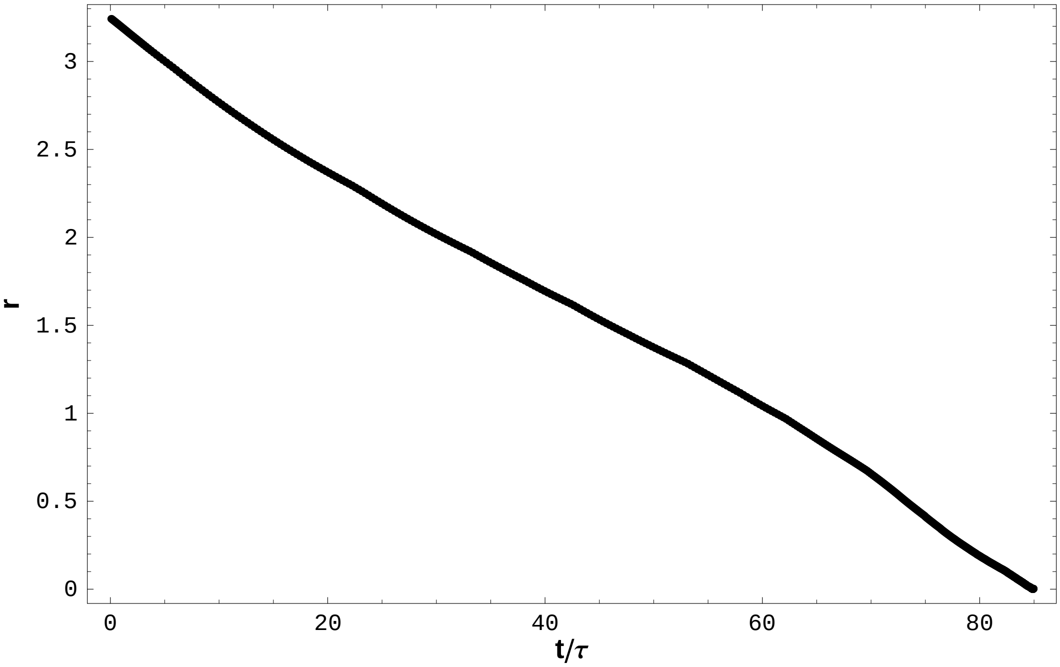

FIGURE 6.7. Plot of the minimum radius r of the holes as a function of time t (divided by τ).

6.3. Singularity Formation

Axisymmetric Droplet

We evolve a sphere perturbed with the $\mathcal{Y}_2^0$ mode for $\epsilon = 0.2$ and slightly supercritical charge $Q = 1.1Q_{cr}$. The droplet elongates and forms two conical tips. The curvature becomes very large.

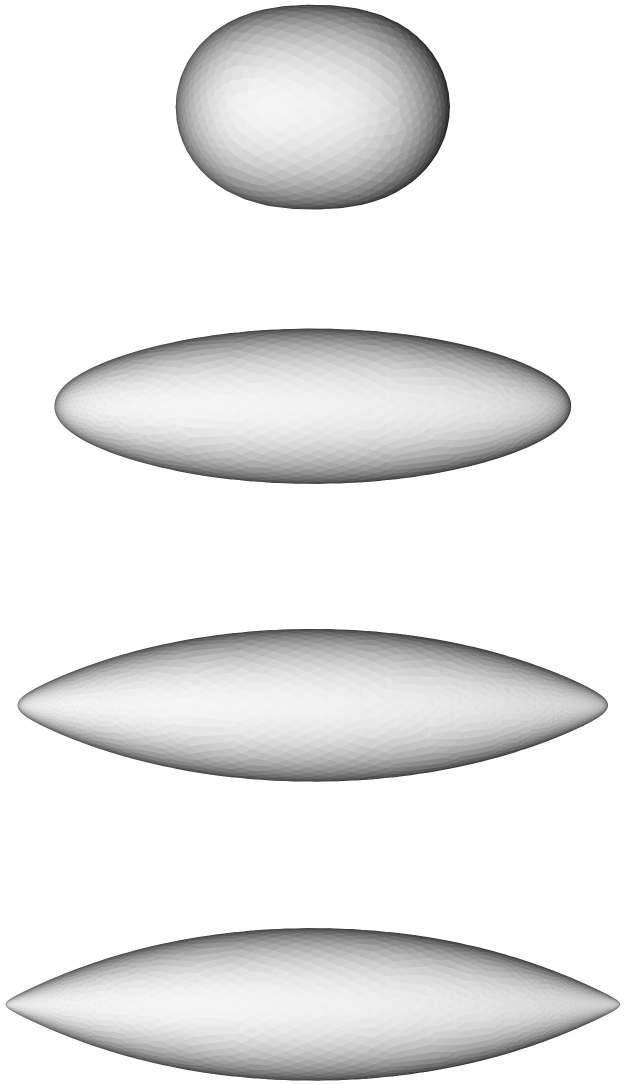

FIGURE 6.8. Axisymmetric droplet with slightly supercritical charge forming conical tips.

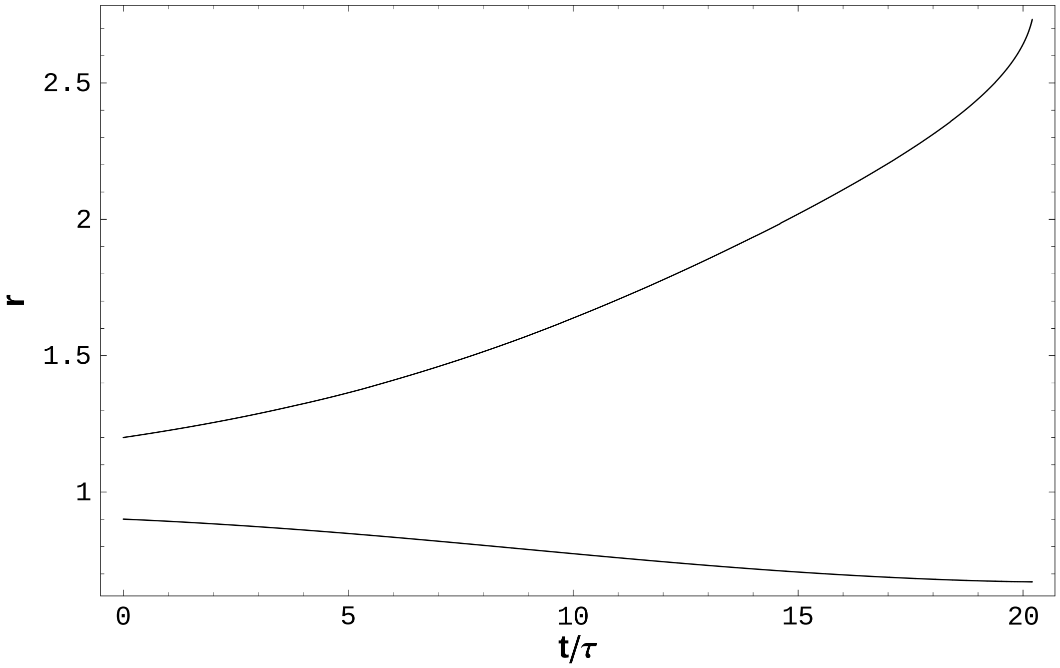

FIGURE 6.9. Plot of the minimum and maximum radius r of the droplet as a function of time t (divided by τ).

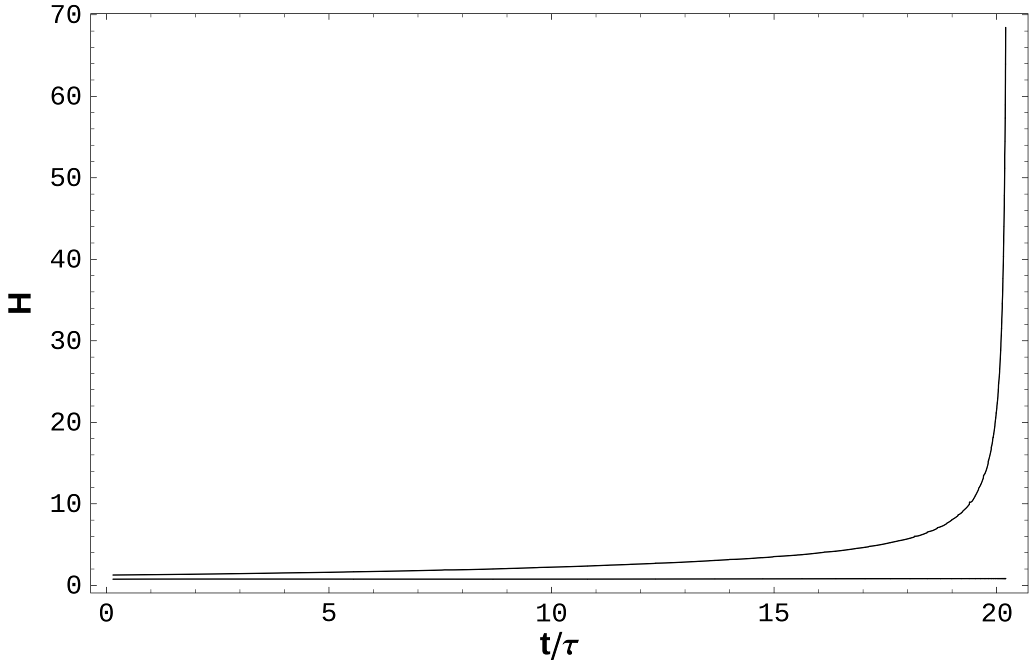

FIGURE 6.10. Plot of the minimum and maximum mean curvature H on the surface of the droplet as a function of time t (divided by τ).

Droplet with Tetrahedral Symmetry

We evolve a sphere perturbed with the $\mathcal{Y}_3^2$ mode for $\epsilon = 0.029$ and slightly supercritical charge $Q = 1.1Q_{cr}$. The droplet forms conical tips at the vertices of a tetrahedron. The curvature becomes very large.

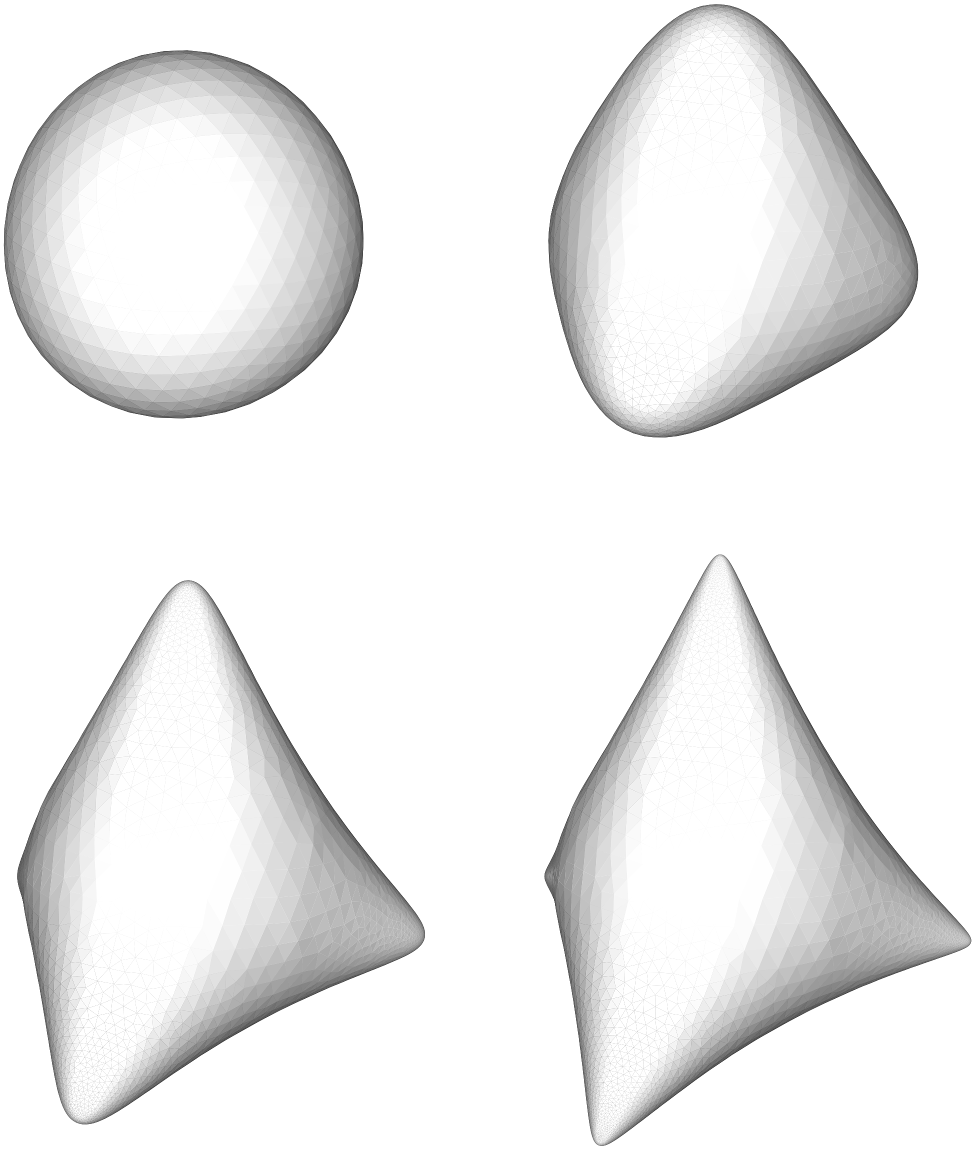

FIGURE 6.11. Droplet with tetrahedral symmetry and slightly supercritical charge forming conical tips.

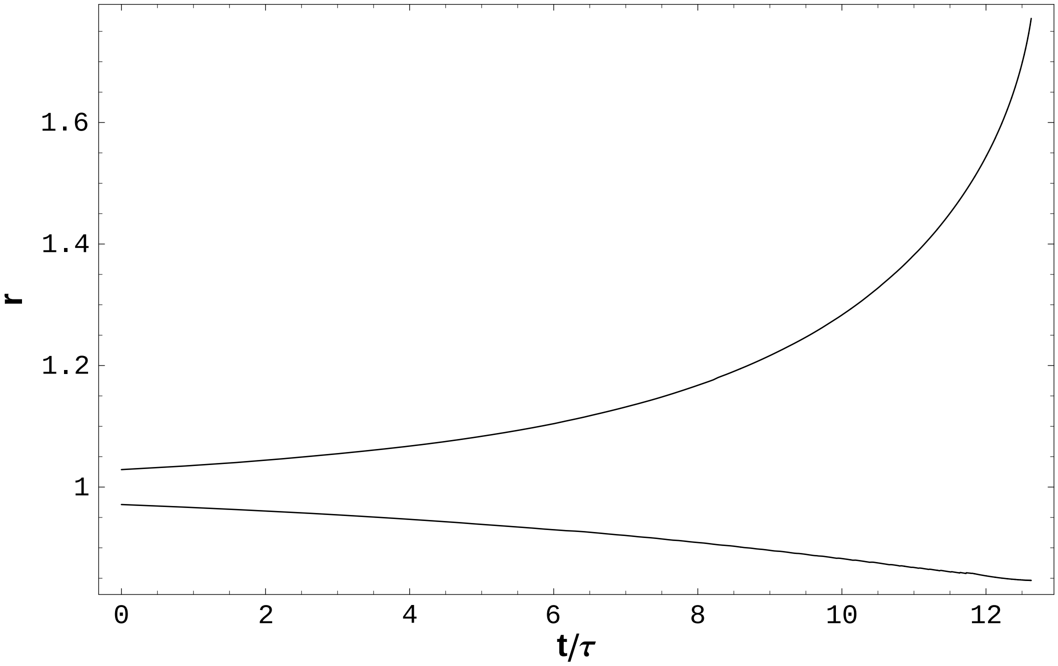

FIGURE 6.12. Plot of the minimum and maximum radius r of the droplet as a function of time t (divided by τ).

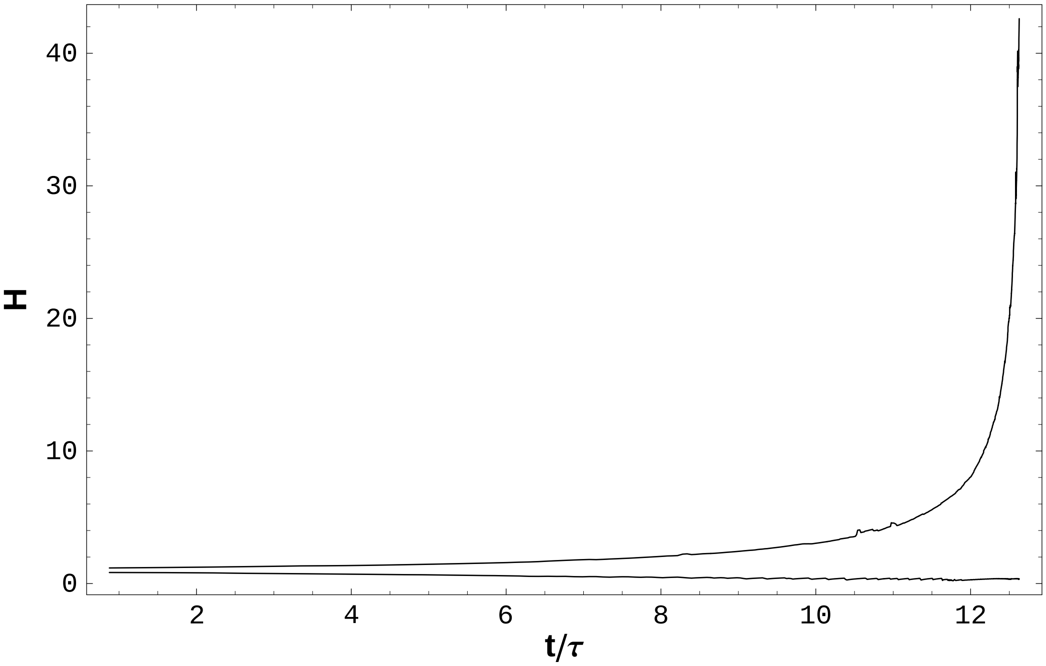

FIGURE 6.13. Plot of the minimum and maximum mean curvature H on the surface of the droplet as a function of time t (divided by τ).

Droplet with Cubical Symmetry

We evolve a sphere perturbed with the $\lambda \mathcal{Y}_4^0 + \mathcal{Y}_4^3$, $\lambda = \sqrt{\frac{7}{40}}$, mode for $\epsilon = 0.014$ and slightly supercritical charge $Q = 1.1Q_{cr}$. The droplet forms conical tips at the vertices of a cube. The curvature becomes very large.

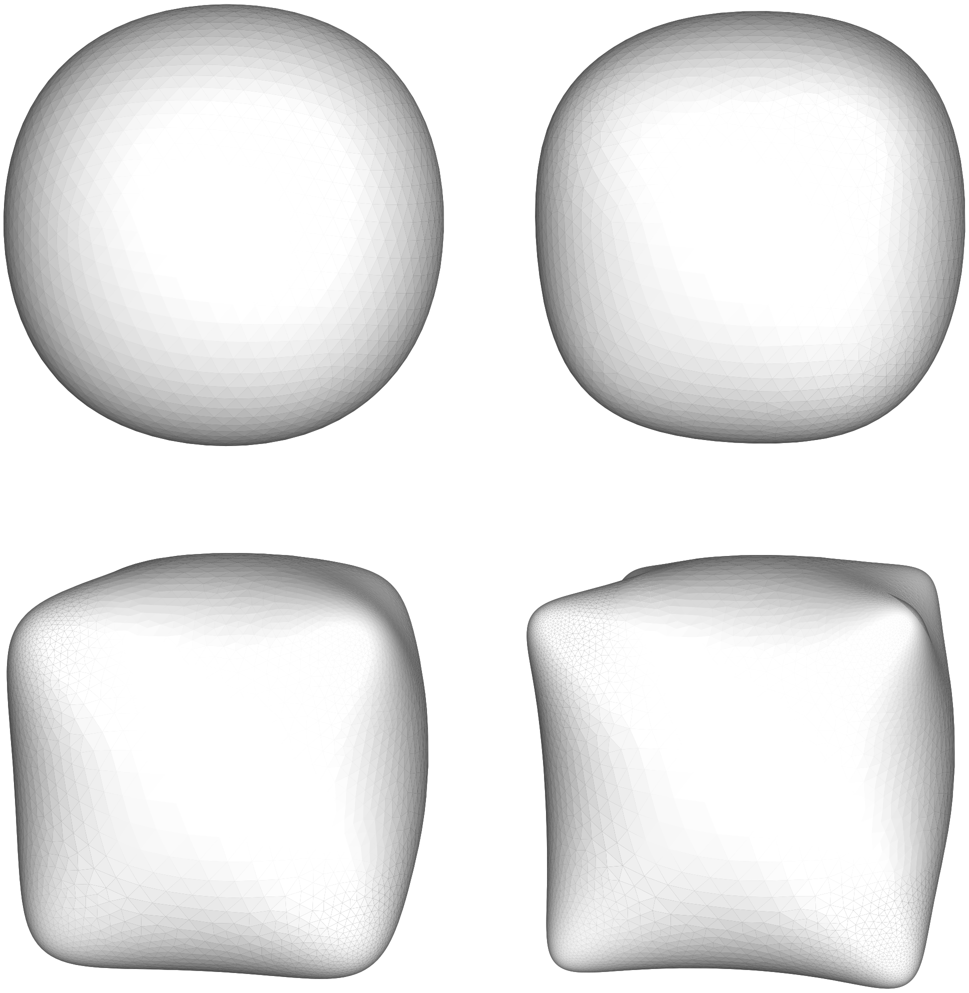

FIGURE 6.14. Droplet with tetrahedral symmetry and slightly supercritical charge forming conical tips.

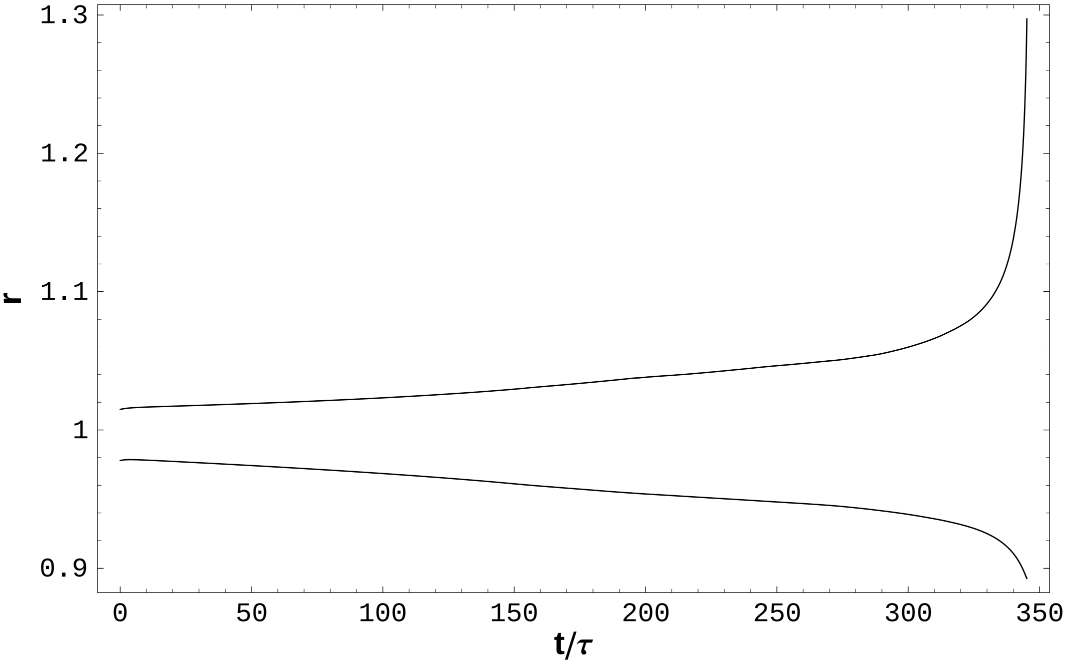

FIGURE 6.15. Plot of the minimum and maximum radius r of the droplet as a function of time t (divided by τ).

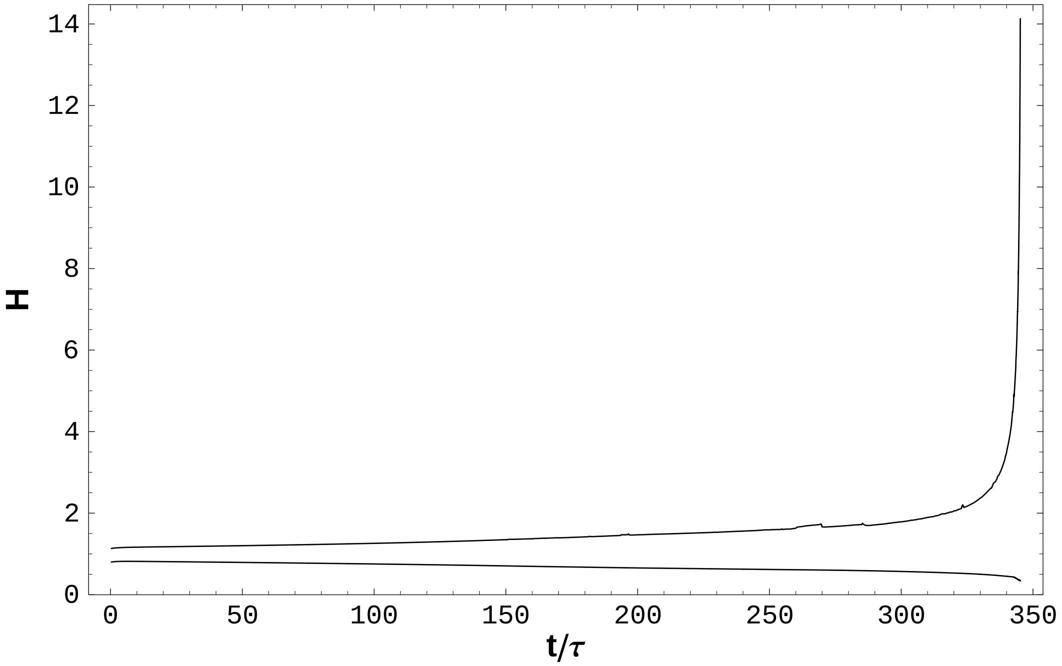

FIGURE 6.16. Plot of the minimum and maximum mean curvature H on the surface of the droplet as a function of time t (divided by τ).

6.4. Instability of Oblate Spheroids

We evolve an oblate spheroid, which is a sphere perturbed by the $\mathcal{Y}_2^0$ mode with *negative* $\epsilon = -0.2$ and very slightly supercritical charge $(Q = 1.01Q_{cr})$. According to [Fon], the oblate spheroid is a stationary solution of the problem. We observe that the oblate spheroid initially appears to be evolving toward a sphere, but soon it becomes apparent that it tends to become *prolate* instead. We conclude that the oblate spheroid is unstable.

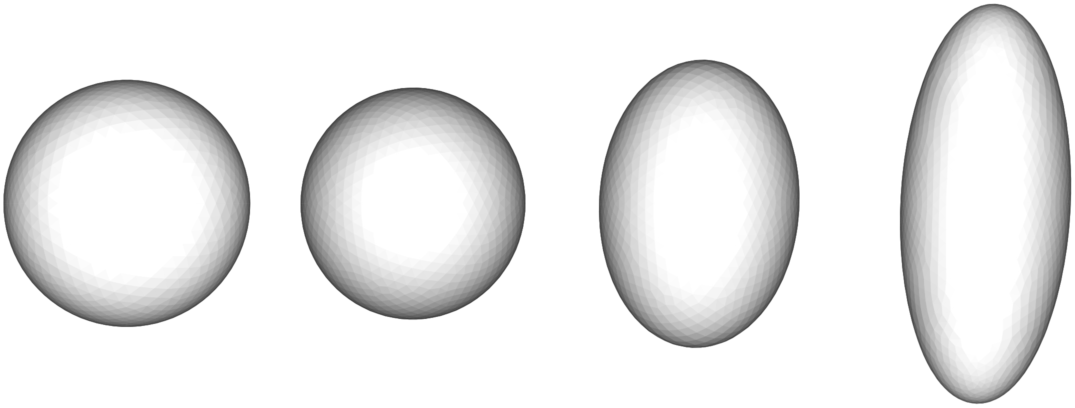

FIGURE 6.17. Evolution of an oblate spheroid into a prolate spheroid. View from the z direction.

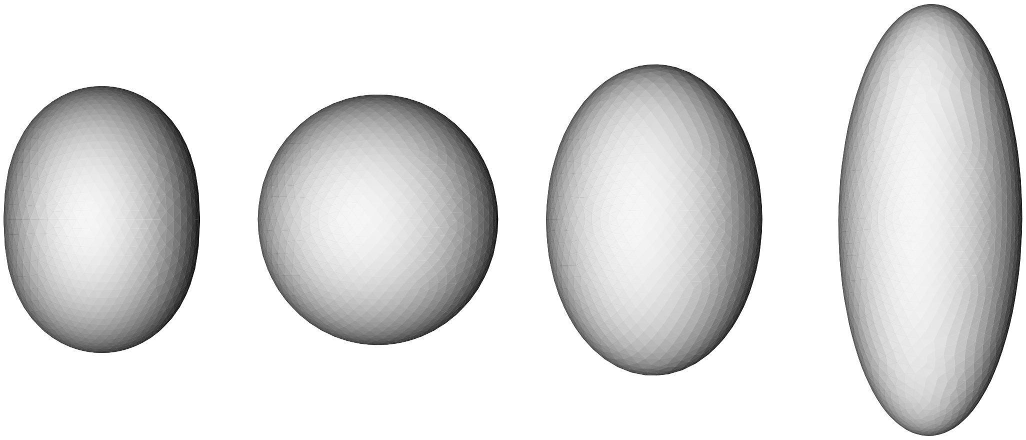

FIGURE 6.18. Evolution of an oblate spheroid into a prolate spheroid. View from the x direction.

BIBLIOGRAPHY

[Abr] M. Abramowitz, I. A. Stegun, *Handbook of Mathematical Functions with Formulas, Graphs, and Mathematical Tables*, John Wiley & Sons, 1972

[Bar] I. G. Loscertales, A. Barrero, I. Guerrero, R. Cortijo, M. Marquez, A. M. Gañan-Calvo, *Micro/Nano Encapsutation Via Electrified Coaxial Liquid Jets*, Science, Vol. 295, 5560 (2002), 1695-1698.

[Bat] D. M. Bates, D. G. Watts, *Nonlinear Regression and Its Applications*, Wiley, 1988.

[Baz] I. B. Bazhlekov, F. N. van de Vosse, H. E. H. Meijer, *3D Numerical Simulation of Drop Coalescence*, Advances in Computation: Theory and Practice, Vol. 7, Kananskis, 2001

[Bea] J. Beauchamp, *Exploding Nanodroplets: Applications to Frontier Studies in Mass Spectrometry, Ion Solvation, and the Chemistry of Molecular Clusters.*, Presentation

[Ber] M. de Berg, M. van Kreveld, M. Overmars, O. Schwarzkopf, *Computational Geometry: algorithms and applications*, Springer, 1997

[Bet] S. I. Betelu, M. A. Fontelos, U. Kindelán, *The shape of charged drops: Symmetry-breaking bifurcations and numerical results*, Progress in Nonlinear Differential Equations and their Applications 63 (2005), 51-58

[Bet2] S. I. Betelu, M. A. Fontelos, *Spreading of a charged microdroplet*, Physica D, 209 (2005) 1-4, 28-35

[Bet3] S. I. Betelu, M. A. Fontelos, U. Kindelán, O. Vantzos, *Singularities on charged viscous droplets*, Arxiv Mathematical Physics e-prints, arXiv.org:math-ph/0512063, Dec 2005

[Bue] J. Buehrle, S. Herminghaus, F. Mugele, *Interface Profiles near Three-Phase Contact Lines in Electric Fields*, Phys. Rev. Lett. 91, 086101 (2003)

[DoC] M. P. do Carmo, *Differential Geometry of Curves and Surfaces*, Prentice-Hall, 1976

[Cha] G. Chartrand, *Introductory Graph Theory*, Dover, 1985

[Cho] S. K. Cho, H. Moon, C.-J. Kim, *Creating, Transporting, Cutting, and Merging Liquid Droplets by Electrowetting-Based Actuation for Digital Microfluidic Circuits*, Journal of Microelectromechanical Systems, Vol. 12, No. 1, Feb 2003

[Chu] T. J. Chung, *Computational Fluid Dynamics*, Cambridge University Press, 2002

[Cox1] H. S. M. Coxeter, *Introduction to Geometry, 2nd ed.*, Wiley, 1969

[Cox2] H. S. M. Coxeter, S. L. Greitzer, *Geometry Revisited*, Math. Assoc. Amer., 1967.

[Cri] V. Cristini, J. Blawzdziewicz, M. Loewenberg, *An Adaptive Mesh Algorithm for Evolving Surfaces: Simulations of Drop Breakup and Coalescence*, Journal of Computational Physics, Vol. 168, pp. 445-463, 2001

[Cun] F. R. Cunha, A. J. De Sousa, M. Lowenberg, *A mathematical formulation of the boundary integral equations for a compressible stokes flow*, Computational and Applied Mathematics, Vol. 22, N. 1, pp. 5373, 2003

[Dvo] P. Dvorak, *Labs-On-A Chip Spur Multiphysics Simulations*, Medical Design, Oct 2005

[Duft] D. Duft, T. Achtzehn, R. Müller, B. A. Huber and T. Leisner, *Rayleigh jets from levitated microdroplets*, Nature, Vol. 421, 2003, pg. 128.

[Eng] G. Engeln-Mülges, F. Uhlig, *Numerical Algorithms with C*, Springer, 1996

[Feng] Z. C. Feng, L. G. Leal, *Numerical Simulation of the Dynamics of an Electrostatically Levitated Drop*, Int. J. Multiphase Flow, Vol. 22, No. 1, pp. 93-120, 1996

[Fon] M. A. Fontelos, A. Friedman, *Symmetry breaking bifurcations of charged drops*, Arch.Ration.Mech.Anal. 172,2 (2004), 267-294

[For] N. Fortner, B. Shapiro, *Equilibrium and Dynamic Behavior of Micro Flows under Electrically Induced Surface Tension Actuation Forces*, Proceedings of the International Conference on MEMS, NANO and Smart Systems (ICMENS'03)

[Fri] A. Friedman, F. Reitich, *Quasi-static motion of a capillary drop, II: the three-dimensional case*, J. Differential Equations 186 (2002) 509-557

[Hay] R. A. Hayes and B. J. Feenstra, *Video speed electronic paper based on electrowetting*, Nature, 425, pp. 383-385 (2003)

[Kat] J. T. Katsikadelis, *Boundary Elements: Theory and Applications*, Elsevier Science, 2002

[Lamb] Sir H. Lamb, *Hydrodynamics, 6th ed.*, Cambridge University Press, 1932

[Lis] R. Lischner, *C++ in a Nutshell*, O'Reilly & Associates, 2003

[Pel] N. A. Pelekasis, J. A. Tsamopoulos, G. D. Manolis, *Equilibrium shapes and staiblity of charged and conducting drops*, Phys. Fluids A 2 (8), Aug 1990

[Poz] C. Pozrikidis, *Introduction to Theoretical and Computational Fluid Dynamics*, Oxford University Press, 1997.

[Poz2] C. Pozrikidis, *Boundary integral methods for linearized viscous flow*, Cambridge University Press, 1992.

[Pur] E. M. Purcell, *Life at Low Reynolds Number*, American Journal of Physics, vol. 45, pp. 3-11, 1977.

[Ray] Lord Rayleigh, *On the Equilibrium of Liquid Conducting Masses Charged with Electricity*, Proc.Roy.Soc. 184-186, 1882

[Rez] S. N. Reznik, A. L. Yarin, A. Theron, E. Zussman, *Transient and steady shapes of droplets attached to a surface in a strong electric field*, J. Fluid Mech. (2004), vol. 516, pp. 349-377

[Rou] J. Roumeliotis, G. R. Fulford, *Droplet Interactions in Creeping Flow*, Computers and Fluids, 29 (2000), pp. 435–450

[Sav] D. A. Saville, *ELECTROHYDRODYNAMICS: The Taylor-Melcher Leaky Dielectric Model*, Annu. Rev. Fluid Mech., 1997, 29:27-64

[Sto] H. A. Stone, A. D. Stroock, A. Ajdari, *ENGINEERING FLOWS IN SMALL DEVICES: Microfluidics Toward a Lab-on-a-Chip*, Annu. Rev. Fluid Mech. 2004, 36:381-411

[Sur] T. Surazhsky, E. Magid, O. Soldea, G. Elber, E. Rivlin, *A comparison of Gaussian and mean curvatures estimation methods on triangular meshes*, ICRA 2003: 1021-1026

[Suv] V. G. Suvorov, E. A. Litvinov, *Dynamic Taylor cone formation on liquid metal surface: numerical modelling*, J. Phys. D: Appl. Phys. 33 (2000) 1245-1251

[Tay] G. I. Taylor, *Disintegration of water drops in an electric field*, Proc. Roy. Soc. London A 280 (1964), 383-397.

[Tho] J. F. Thompson, B. K. Soni, N. P. Weatherill, *Handbook of Grid Generation*, CRC Press, 1999

[Van] A. VanderWyst, A. Christlieb, M. Sussman, I. D. Boyd, *Level Set Simulations of Charged Droplets Using a Boundary Element Method*, IEPC-2005-019 Presented at the 29th International Electric Propulsion Conference, November 2005, Princeton University

[Wei1] E. W. Weisstein, *"Rotation Formula", From MathWorld - A Wolfram Web Resource*, http://mathworld.wolfram.com/RotationFormula.html

[Wol] S. Wolfram, *The Mathematica Book, 5th Ed.*, Wolfram Media, 2003

[Yang] C. Yang, *Dynamic Point-Formation in Dielectric Fluids*, ArXiv Physics e-prints, arXiv.org:physics/0303122, Mar 2003

[Yar] A. L. Yarin, S. Koombhongse, D. H. Reneker, *Taylor cone and jetting from liquid droplets in electrospinning of nanofibers*, J. Appl. Phys. 90, 4836 (2001)

[Zna1] V. Znamenskiy, I. Marginean, A. Vertes, *Solvated Ion Evaporation from Charged Water Nanodroplets*, J Phys. Chem. A 2003, 107, 7406-7412

[Zna2] V. S. Znamenskiy, A. Vertes, *Molecular Dynamics of Ion Formation from Charged Nanodroplets in Electrospray Ionization*, 50th ASMS Conference, Jun 2002

[Zin] A. Z. Zinchenko, M. A. Rother, R. H. Davis, *A novel boundary-integral algorithm for viscous interaction of deformable drops*, Phys. Fluids, Vol. 9. No. 6, June 1997